DOPAS
(Contract Number: FP7 - 323273)

Deliverable n°3.32

Final report on the sealing behaviour of fractured claystone and seal materials (THM-Ton)

Author(s)   *Chun-Liang Zhang*

Date of issue of this report: **29.02.2016**

Start date of project: 01/09/2012   Duration: 48 Months

Scope	Deliverable n°3.32 (WP3 + WP5)	Version:	1.0
Type/No.		Total pages	2+148
		Appendixes	
Title	Final report on the sealing behaviour of fractured claystone and seal materials – THM-Ton	Articles	6

ABSTRACT:

This report presents the work performed by GRS as part of the European project DOPAS (Full scale Demonstration of Plugs and Seals) under WP 3 task 2 and WP 5 task 1 on "Design and technical construction feasibility of the plugs and seals" and "Performance assessment of plugs and seals systems". This subproject performed more comprehensive experiments on the claystone-bentonite mixture in comparison with pure bentonite and bentonite-sand mixture. The seal materials were characterized in terms of key geotechnical properties. The sealing behaviour of the excavation damaged claystone (EDZ) that will play an important role in the long-term seal performance of the plug/seal systems was also studied.

RESPONSIBLE:

GRS, Oliver Czaikowski

APPROVED FOR SUBMISSION:

DOPAS Coordinator Johanna Hansen 31.5.2016

DOPAS

Deliverable n° 3.32 Version n°1.0
Dissemination level: PU
Date of issue of this report: **29.02.2016**

2/2

GRS

Gesellschaft für Anlagen-
und Reaktorsicherheit
(GRS) gGmbH

**Full Scale Demonstration of
Plugs and Seals (DOPAS)**

Deliverable D3.32

**Sealing behaviour of
fractured claystone and
seal materials**

Final Report

Chun-Liang Zhang

February 2016

GRS - A - 3852

Table of contents

4

1 Introduction

Many countries have chosen argillaceous clay formations for deep geological disposal of radioactive waste, such as the Callovo-Oxfordian formation in France /AND 05/ and the Opalinus Clay formation in Switzerland /NAG 02/. In Germany, two clay formations, the Unterkreide Clay in the north and the Opalinus Clay in the south of Germany, are proposed as potential host rock for the disposal of high level radioactive waste (HLW) /BGR 07/ and /JOB 15a,b/ and /LOM 15/.

Depending on the individual geological environments and safety requirements on the potential repositories, these countries have developed reference disposal concepts /NAG 02/, /AND 05/, /JOB 15a/b/ and /LOM 15/. Various feasible techniques for the disposal operations have been developed and demonstrated by large and full-scale experiments in the Underground Research Laboratories (URLs), for instance, at the Mont-Terri-URL in Switzerland, the MHM-URL in France, and the other URLs in different host rocks.

The European Full-Scale Demonstration of Plugs and Seals project (DOPAS) conducted during the time period of 09.2012 – 08.2016 is a technology development project to improve the adequacy, consistency and industrial feasibility of the plugs and seals designed for safe sealing repositories in different geological formations (clay, salt, crystalline/granite) /HAN 13/14/. According to the geological conditions, different types of plugs and seals have been designed and demonstrated in the DOPAS project by five full-scale experiments:

1. Full-Scale Seal (FSS) in France;
2. Experimental Pressure and Sealing Plug (EPSP) in Czech Republic;
3. Dome Plug (DOMPLU) in Sweden;
4. Posiva's Deposition Tunnel Plug (POPLU) in Finland; and
5. In situ Demonstration Test for Shaft Sealing Components (ELSA) in Germany.

The materials used for the construction of the plugs and seals are characterized in laboratory experiments to provide a robust database for analysing the long-term sealing performance of the plug/seal systems.

In most of the plug/seal concepts, compacted bentonite-based materials are chosen to ensure certain swelling pressures to compress the surrounding damaged rock and to achieve low hydraulic conductivity of the whole plug/seal system. As an alternative to the bentonite-based materials, crushed claystone produced by excavation of repository openings is also considered as backfill/seal material, because of its many advantages such as chemical-mineralogical compatibility with the host rock, availability in sufficient amounts, low costs of material preparation and transport, and no or less occupancy of the ground surface for the excavated claystone. The crushed raw material shall be used for backfilling repository openings and, mixed with bentonite, for sealing boreholes, drifts, and shafts. In the frame of the previous German national projects /ZHA 10a/13a/, an investigation programme was performed with the crushed claystone excavated from the MHM-URL. The experiments showed favourable properties of the crushed claystone as backfill material and the compacted claystone-bentonite mixture as seal material with respect to their barrier functions.

In task 3.2 of the DOPAS project, GRS performed more comprehensive experiments on the claystone-bentonite mixture in comparison with pure bentonite and bentonite-sand mixture. The seal materials were characterized in terms of key geotechnical properties such as compacted density, water uptake and retention capacity, swelling pressure and expansion, water permeability and gas migration.

Additionally, GRS also investigated the sealing behaviour of the excavation damaged claystone (EDZ) that will play an important role in the long-term seal performance of the plug/seal systems. This important issue was studied with artificially-cracks claystones under relevant in situ conditions, including determination of the long-term deformation, damage und induced permeability, moisture effects on deformation and strength, fracture closure and permeability reduction, gas migration in damaged and resealed states.

The experimental results on the seal materials and the claystones were evaluated concerning the model prediction of the sealing performance of the plug/seal systems in clay formations. The modelling work was performed in task 5.1 by verification and improvement of the constitutive models for the hydro-mechanical behaviour of the seal materials and the claystones, which are available in the THM computing code CODE-BRIGHT developed by the Technical University of Catalonia (UPC) /UPC 15/. The validation of the models was carried out by numerical simulations of various kinds of la-

boratory experiments performed on the seal materials and claystone using CODE-BRIGHT.

This report presents the final work and results achieved by GRS as part of the DOPAS project under task 3.2 "characterization of seal materials applied in plug/seal systems" and task 5.1 "performance assessment of the plug/seal systems and identification of the relevant tools for predicting the behaviour of a complete plug/seal system". Chapter 2 gives a short overview of the backfilling/sealing concepts for repositories in clay formations. Chapter 3 highlights the self-sealing behaviour of fractured claystones. The geotechnical properties of the investigated seal materials (claystone-bentonite mixture, bentonite, and bentonite-sand mixture) are illustrated in chapter 4. The modelling work is reported in chapter 5. Finally, main conclusions drawn from the investigations are summarized in chapter 6.

Remarks:
The report at hand is the final technical report issued after 42 months of the DOPAS project. This report supersedes the interim version (D5.5) /ZHA 14a/ issued after 24 months of the DOPAS project.

2 Backfilling and sealing concepts

The fundamental basis of the geological disposal concepts for radioactive waste is generally a multi-barrier system, which comprises the natural geological formations and engineered barriers (EBS). The EBS represents engineered materials placed within a repository, including the waste form, waste canisters, buffer, backfill, plugs and seals. After emplacement of radioactive waste, the disposal boreholes/drifts, access drifts and shafts must be backfilled and sealed with suitable materials to prevent release of radionuclides into the biosphere. The engineered barriers are designed to assure the stability of the repository and of the thermo-hydro-mechanical-chemical (THMC) conditions, and to provide low permeabilities and diffusivities, chemical buffering, and long-term retardation of radionuclides.

In deep clay host formations, which are practically impermeable and have sufficiently large dimensions, the engineered barriers will play a central role in the disposal system ensuring the long-term containment and retardation of radioactive waste. According to the characteristics of the clay host rocks at selected potential repository sites, the disposal concepts and the functional requirements on each component of the EBS, reference backfilling and sealing concepts have been developed in several countries including France, Switzerland, Belgium, Germany, and others. Clay-based backfill and seal materials and emplacement techniques have been investigated and demonstrated in full-scale experiments under realistic repository conditions. Some reference backfilling/sealing concepts for the potential repositories in argillaceous formations are briefly represented in the following.

2.1 Swiss concept

Fig. 2.1 shows an overview on the Swiss reference backfilling/sealing concept for spent fuel / high level radioactive waste (SF/HLW) in the Opalinus Clay at a depth of about 650 m below the surface /NAG 02/, /OEC 04/, /KOH 15/. The argillaceous formation at the potential repository site has a thickness of about 100 m. In order to maximise the length of the radionuclide transport to adjacent formations both above and below the repository, the horizontal disposal in drifts was selected. The waste emplacement drifts and the operation drifts will be excavated in the centre of the formation. SF/HLW will be emplaced in horizontal drifts of 2.8 m inner diameter and 800 m length. The disposal

drifts are separated by pillars of 40 m width and oriented in the direction of the maxi-mum principle stress so as to favour the stability. Each canister will be embedded in a suitable buffer material that is made of compacted bentonite blocks and of granulated bentonite mixture.
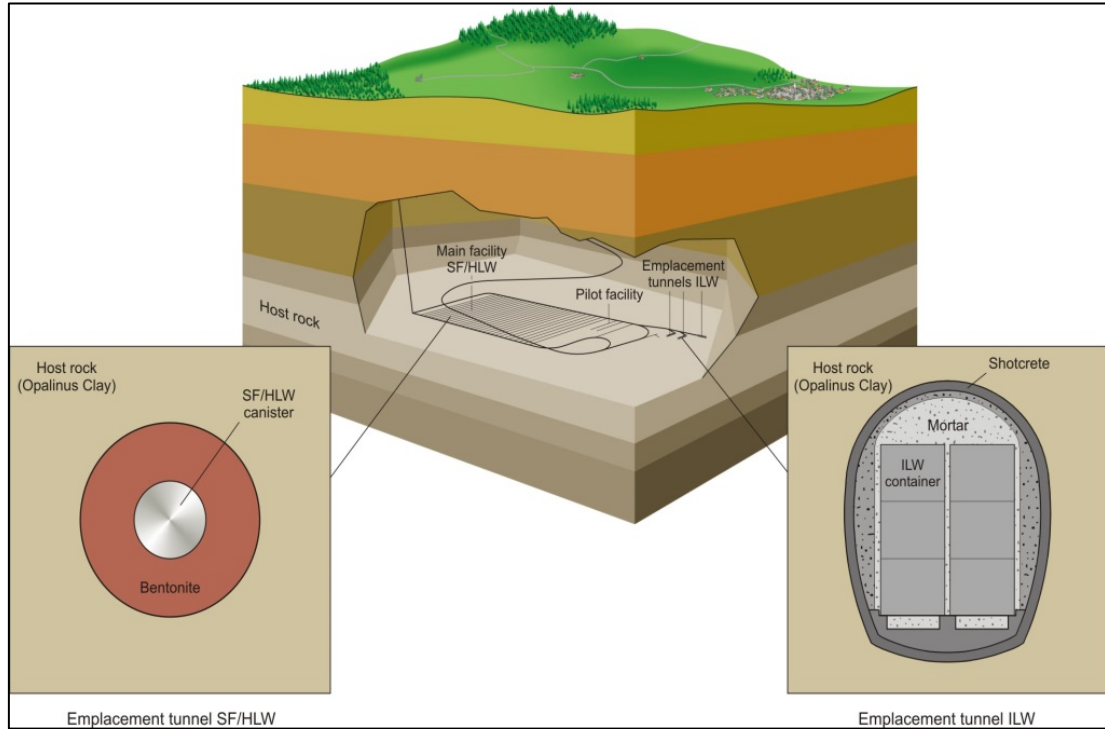
Possible layout of a deep repository
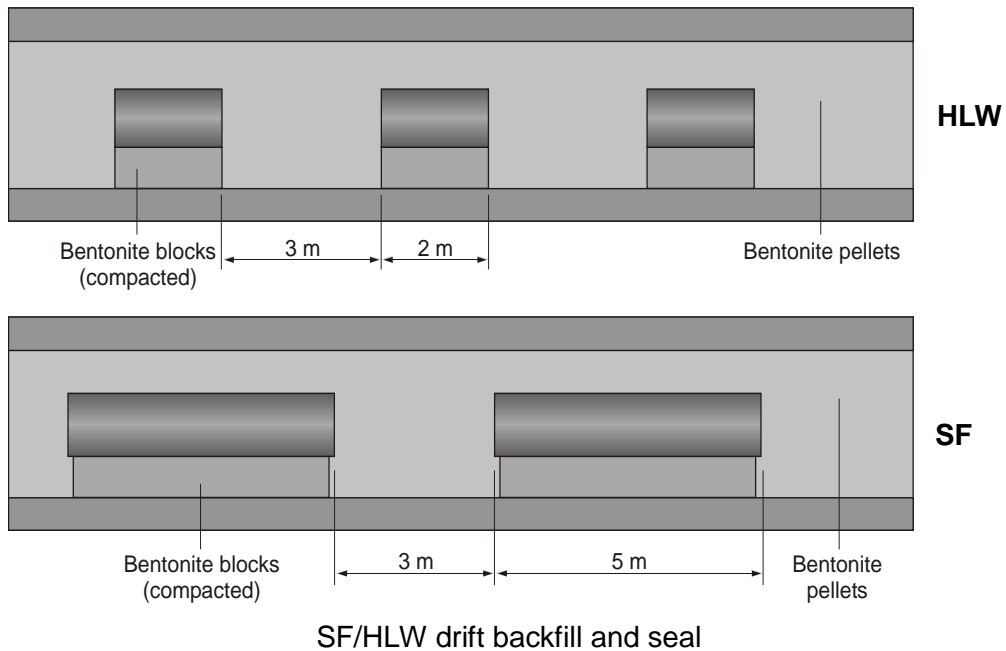
SF/HLW drift backfill and seal

Fig. 2.1   Swiss repository concept for SF and HLW disposal in horizontal drifts in the Opalinus clay formation /NAG 02/

Sufficiently high density is required for the buffer to ensure adequate long-term sealing performance of the bentonite-based material since it directly influence the other safety relevant attributes such as mechanical stability, swelling pressure, hydraulic conductivity to water and gas, porosity and suppression of microbial activity. A saturated density of 1.90 g/cm^3 (corresponding to a dry density of 1.45 g/cm^3) for the bentonite buffer is a desirable target and can be achieved by constructing bentonite blocks of a dry density of 1.80 g/cm^3 on the drift floor and by backfilling bentonite pellets into the remaining space using a prototype backfilling machine with five auger conveyers, as demonstrated in the Full-Scale Emplacement (FE) Experiment at the Mont-Terri URL /MUL 15/.

Final closure of the repository would involve installation of ~ 40 m long seals of highly compacted bentonite in the access drifts and backfilling the ramp with a mixture of bentonite and sand.

2.2 French concept

In the French disposal concept, HLW and ILW will be disposed in the Callovo-Oxfordian argillaceous formation at a depth of about 500 m below the surface /AND 05/15/. The repository is located on a single level in the middle of the formation with a thickness of about 130 m and divided into HLW and ILW disposal areas. Fig. 2.2 shows the concept for the French Deep Geological Repository (Cigéo) /AND 15/.
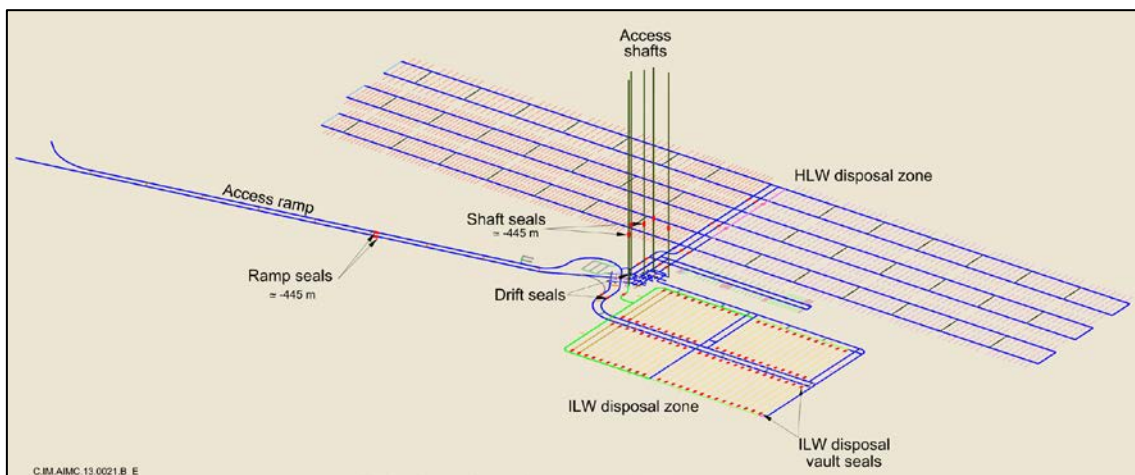

Fig. 2.2   French repository concept for HLW and ILW disposal in horizontal boreholes and drifts in the Callovo-Oxfordian clay formation /AND 15/

The HLW disposal area includes several hundred disposal boreholes of 70 cm diameter and tens of meters in length. The boreholes are steel-lined to support the surrounding rock and to ensure emplacement and potential retrieval of waste packages. No buffer material is placed in the disposal cells, but grout is injected in the annular gap between the rock wall and the steel liner. The boreholes are sealed with a swelling clay core and with two low-pH concrete containment plugs, one at each end.

The ILW disposal area includes several tens of large-diameter disposal vaults, each about 400-500-m long. Waste containers are emplaced in a concrete disposal container. Vault concrete lining and disposal containers provide a cementitious environment for the waste. The gaps between waste packages and vault lining could be left empty or backfilled with cementitious material or neutral filler.

The remaining openings are backfilled and sealed. The excavated host rock is used to backfill the drifts, shafts and ramps with the concrete lining maintained. In key positions, the shafts, ramps, drifts, and disposal vaults will be sealed. Fig. 2.2 shows the seal locations. The conceptual designs for the seals are quite similar. Fig. 2.3 illustrates an example for a drift seal /FOI 15/. Each seal consists of a swelling clay core and two low-pH concrete containment walls. The swelling core provides the required long-term sealing performance, whereas the containment walls are to confine the core mechanically. Before installation of the swelling core, the concrete linings in the selected positions are fully or partly removed, depending on the mechanical strength of the host rock there. Shaft and ramp seals will be located in the upper part of the COX formation with sufficiently high strength, so that the lining can be fully removed there. For the drift and vault seals in the middle part of the formation with less strength, the lining is allowed to be partly removed. The removal of the lining ensures a good contact and seal between the clay core and the host rock.

Based on the safety functions, requirements on the seals are specified. For instance, a low hydraulic conductivity of 10^{-11} m/s is currently set for the swelling cores in the drift seals, even though the performance assessment modelling has suggested a higher value of 10^{-9} m/s for the seals /WHI 14/. The swelling pressure shall be close to but not exceed the effective mechanical stress of 7 MPa and a length of two drift diameters (or 20 m) at least. Bentonite-based materials such as bentonite pellets and bentonite-sand mixture will be used for the swelling cores. The swelling cores have to be constructed to be homogeneous and have a good contact with the surrounding rock.
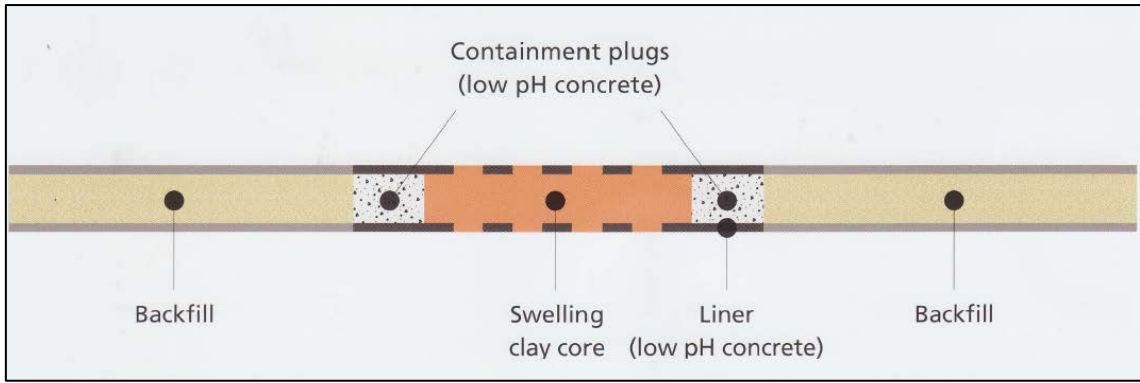
Fig. 2.3   French reference drift sealing and backfilling concept /FOI 15/

In order to develop confidence in and to demonstrate the feasibility of constructing the full-scale seals, large and full-scale experiments have being undertaken in the MHM-URL and in surface facilities, for instance, FSS /FOI 15/ and NSC /DEL 15/ experiments.

The FSS Experiment is a demonstrator experiment for the drift seal and carried out within the DOPAS project /FOI 15/. The swelling clay core was comprised of bentonite pellets and powder in a ratio of 70 % to 30 %. The material was backfilled in a concrete-made drift model of 7.6 m diameter and 36 m length. The feasibility of filling the drift with recesses in the host rock was demonstrated. After emplacement an average dry density of 1.49 g/cm^3 was achieved. Fig. 2.4 shows the concept of the FSS seal as constructed.
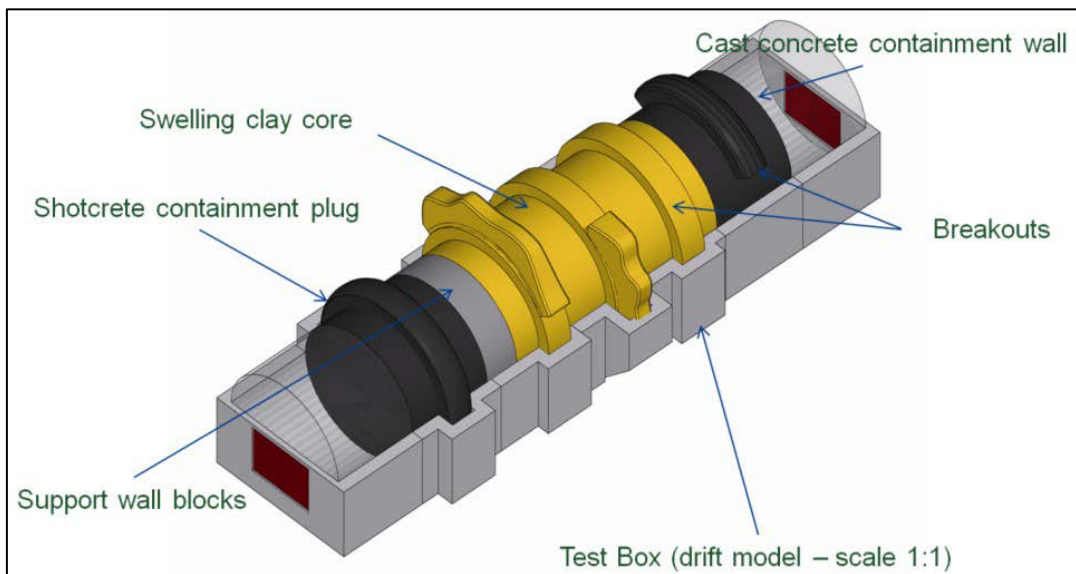
Fig. 2.4   longitudinal view of the FSS experiment made by ANDRA /FOI 15/

The NSC Experiment is a large-scale experiment to evaluate the sealing performance of a drift seal itself and the interface between the seal and the surrounding EDZ /DEL 13/15/. A drift of 5 m long and 4.6 m in diameter was sealed using the compacted bentonite-sand blocks (300 x 200 x 100 mm). The remaining space between the drift wall and the seal was filled with bentonite pellets. Fig. 2.5 shows the test layout and a picture of the seal construction. An average dry density of 1.45 g/cm^3 was estimated for the constructed seal.
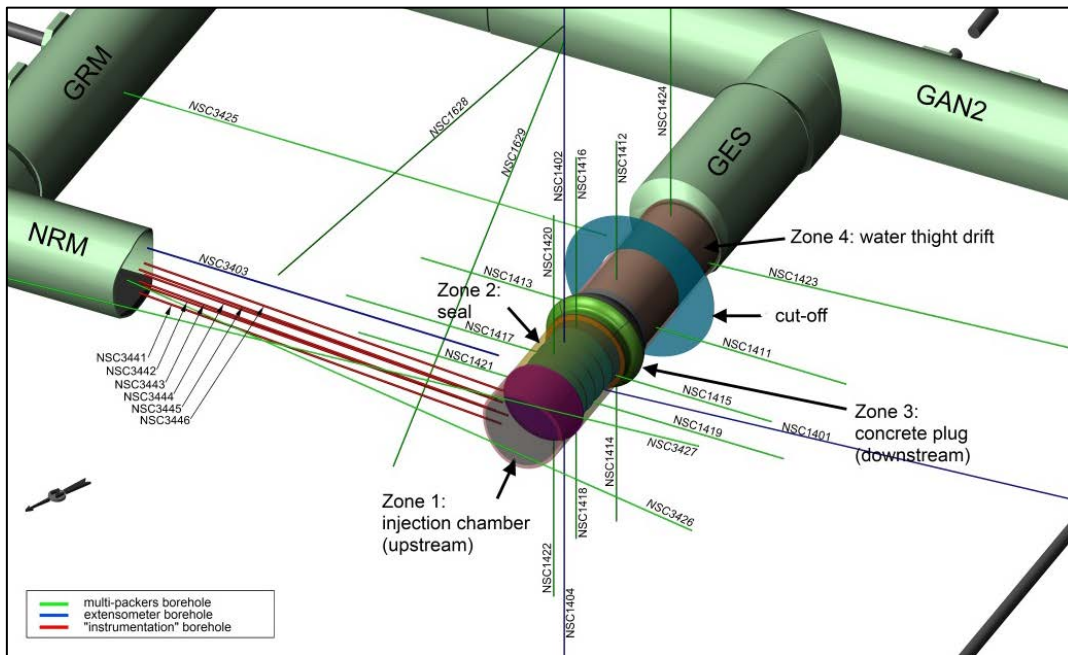
Fig. 2.5   General layout of the NSC experiment in the MHM-URL and seal construction in the drift using bentonite-sand blocks and bentonite pellets /DEL 15/

2.3   German concept

Within the framework of the German R&D project "ANSICHT" /JOB 15a/ for develop-
ment of an integrated methodology to demonstrate the safety of a HLW repository in
clay formations in Germany, two disposal concepts as well as the associated backfilling
and sealing concepts have been proposed for two clay host formations respectively:
the SOUTH concept for the Opalinus Clay in the southern Germany /JOB 15b/ and the
NORTH concept for lower-cretaceous Clays (Barremium and Hauterivium) in the
northern part of Germany /LOM 15/. One key point is to demonstrate the integrity of the
geological and engineered barriers for isolating the waste in the host rock called "con-
tainment rock zone" (CRZ) for a period of 1 million years.

The Opalinus Clay host rock at the repository model site in the south of Germany is in
a thickness of 100 to 130 m. The potential repository will be at a depth of about 670 m
below the ground surface. Due to the limited thickness of the Opalinus clay the horizon-
tal drift disposal, like in the Swiss concept (Fig. 2.1), is the only suitable option since a
vertical borehole disposal would lead to a very small CRZ only. Fig. 2.6 shows the
schematic of the disposal drift with concrete liner, backfill and POLLUX casks. The
drifts have an excavated cross section of about 22-24 m^2 and a length of 400 m. With
regard to temperature limitations in buffer and host rock /JOB 15a/, the distance be-
tween neighbouring casks will be of 23 m and the distance between the drifts of 20 m.
In the preliminary concept, the casks will be laid down on highly compacted blocks
consisting of prepared excavated rock material (Opalinus clay). If necessary, expansive
clay minerals will be added to ensure a sufficient swelling pressure development. The
remaining spaces in the emplacement drifts will be backfilled using a prepared granu-
late of the same material. The use of the excavated claystone or claystone-bentonite
mixture as buffer material is desired because of its chemical-mineralogical compatibility
with the host rock and other advantages.

The large thickness of about 540 m of the Lower-cretaceous Clay host rock in the
northern of Germany allows HLW disposal in vertical boreholes with sufficient large dis-
tances to the above and below adjacent formations leading to a much smaller footprint
of the repository. The main level of the potential repository will be at a depth of ca. 770
m below the ground surface. Fig. 2.7 illustrates the principle of the vertical borehole
disposal concept. Vertical boreholes will be drilled to a depth of 27 m. Considering pos-
sibly high rock stresses, the boreholes are lined with steel tubes to prevent breakout of

the borehole walls. Three waste canisters are emplaced in an inner steel tube and separated with dry sand. This inner casing allows the retrieval of the canisters easily, when it is required within 500 years after the disposal. The casing is emplaced on the compacted clay-based buffer at the bottom. The remaining annular space between the inner and out liners is backfilled with the compacted clay-based ring blocks. The boreholes are sealed with plugs at the tops. The utilisation of the excavated claystone is desired for the buffers.
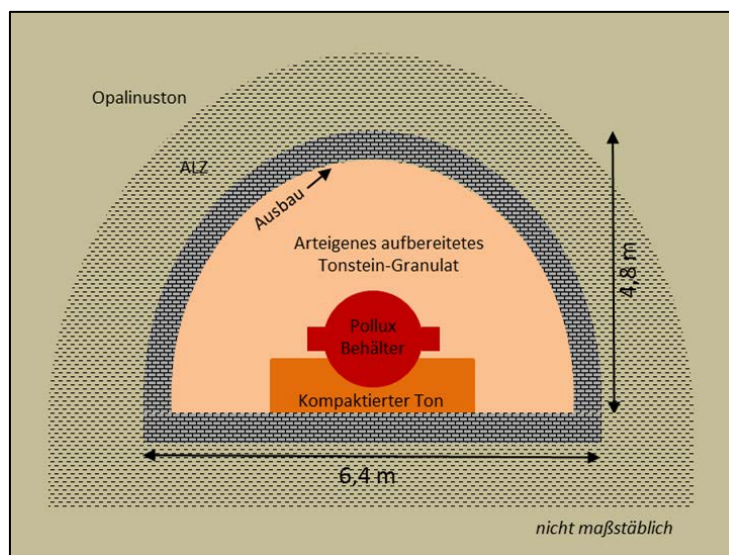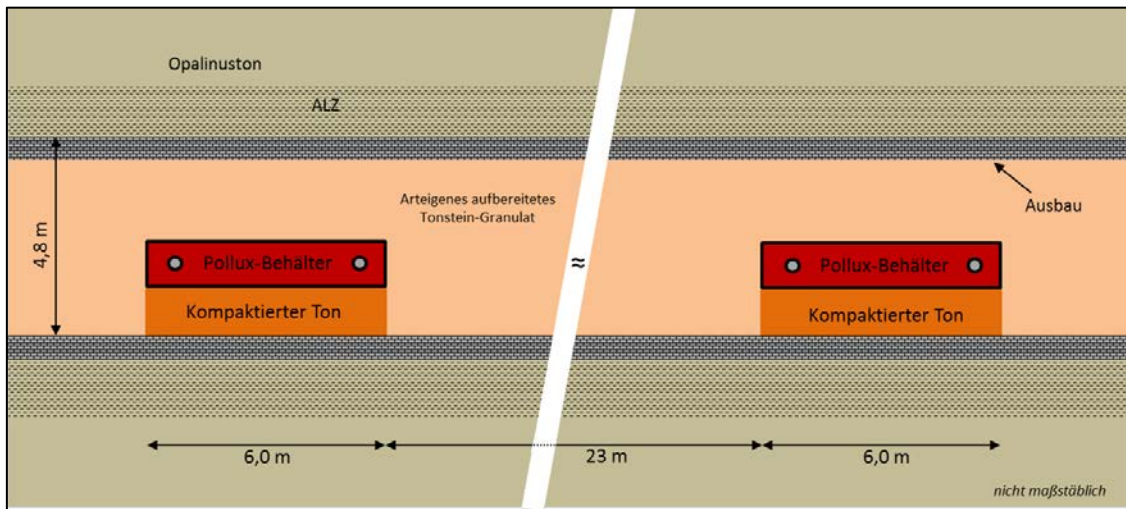
Fig. 2.6   German concept for HLW disposal in horizontal drifts in Opalinus Clay /JOB 15b/
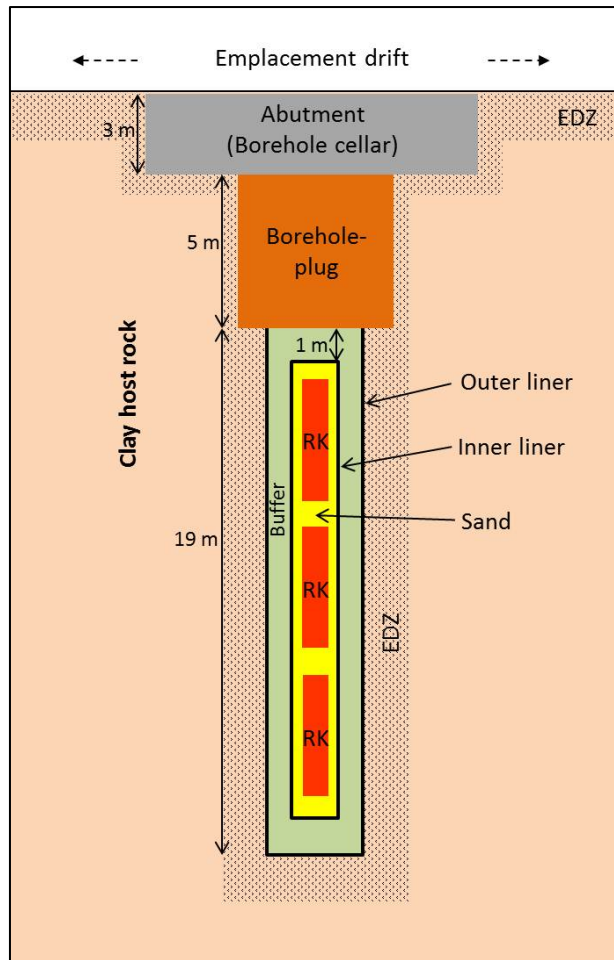
Fig. 2.7   German concept for HLW disposal in vertical boreholes in Lower-cretaceous Clay /LOB 15/

A similar principle to ANDRA's drift backfill/seal concept (Fig. 2.2) is taken into account in the German concepts for backfilling and sealing drifts. Fig. 2.8 shows an example of the drift plug/seal system proposed for the potential repository in the Lower-cretaceous Clay. Subject to mechanical stability demonstration the liner at the sealing element location will be removed and several slots will be excavated into the rock. Two seal cores will be constructed with compacted clay-based blocks and bentonite pellets filling the remaining space between the drift walls and blocks (cf. Fig. 2.5). The seal cores must have certain swelling capacity to compress and cut off the EDZ. The seal cores are confined by three concrete plugs at each end and in the middle to ensure the mechanical stability. It is also considered to add asphalt/bitumen elements between the seal cores and plugs as immediate active seal elements. The remaining space in the drifts will be backfilled with the excavated claystone, which is expected to take the long-term barrier function.
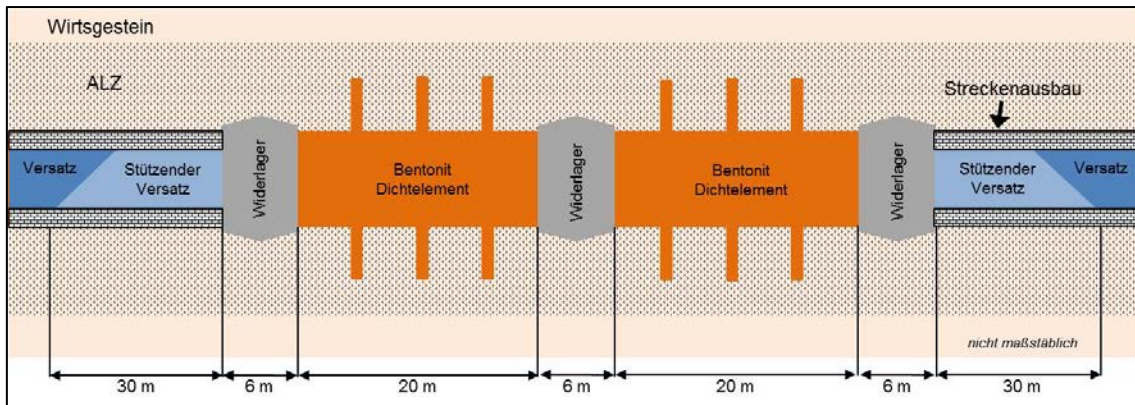
Fig. 2.8   German drift backfilling/sealing concept for the potential repository in Unterkreide Clay /LOB 15/

It is to be pointed out that the EDZ as a crucial component belongs to any plug/seal systems because its hydro-mechanical behaviour determines the sealing performance of the whole systems.

Shaft sealing systems, currently under development in the German ELSA project /HER 15/, will complement the overall sealing system yielding a multi-barrier system considering redundancy and diversity in sealing elements and sealing material.

3   Sealing behaviour of fractured claystone

Excavation of a repository leads to a concentration of the deviatoric stress in the surrounding rock and results in micro- and macrocracks in the near-field, which may act as potential pathways for fluid flow and radionuclide migration into the biosphere. As observed in the URLs at Mont-Terri /BOS 04/ and at Bure /ARM 14/, the damaged zone is developed near drift walls and the permeability increases over several orders of magnitude.

However, reconsolidation and sealing of the fractures in the EDZ can be expected due to the convergent compression of the surrounding clay rock, the increasing resistance of the backfill/seal materials, and the swelling of clay minerals into fracture interstices. The closure of the fractures will decrease the hydraulic conductivity, depending on the mineralogical components of the clay rock and the hydro-mechanical conditions. As the EDZ becomes water-saturated, gas migration through the EDZ may need a sufficiently high pressure to overcome the capillary resistance in it.

For assessment of the sealing performance of the plug/seal systems and hence the long-term safety of a repository, the development of the EDZ surrounding the plugs and seals has to be precisely characterized, deeply understood, and reliably predicted. This important issue has been extensively investigated at the GRS laboratory in the frame of the R&D projects EC-NFPRO /ZHA 08a/, EC-TIMODAZ /ZHA 10a/, THM-TON /ZHA 13a/ and EC-DOPAS project /ZHA 14c/d/. Various laboratory experiments were carried out on core samples from the Callovo-Oxfordian (COX) and the Opalinus (OPA) clay rocks in order to investigate the long-term deformation, damage and failure strength, damage-induced permeability, swelling capacity, self-sealing of fractures, water and gas flow in damaged and resealed claystone. The results are presented in the GRS reports and publications /ZHA 08/a/b/, /ZHA 09/, /ZHA 10a/b/, /ZHA 11/, /ZHA 13a/b/, /ZHA 14a/b/, /ZHA 15a/b/. A number of scientific papers dealing with the key topics were published during the time period of the DOPAS project:

A. Sealing of fractures in claystone, *Journal of Rock Mechanics and Geotechnical Engineering* (2013) /ZHA 13b/;

B. Gas migration in damaged and resealed claystone, *Geological Society Special Publication 415* (2014) /ZHA 14b/;

C. Deformation of clay rock under THM conditions, *Journal of Geomechanics and Tunnelling* (2015) /ZHA 15a/;

D. Stress-strain-permeability behaviour of clay rock during damage and recompaction, *Journal of Rock Mechanics and Geotechnical Engineering* (2015) /ZHA 15b/.

This report focuses on the most important issues of damage-induced permeability and self-sealing of fractures in claystones, whereas the other topics mentioned above can be found in the given documentations.

3.1 Characteristics of investigated claystones

The Callovo-Oxfordian claystone (COX) at the -490m level of the MHM-URL and the Opalinus claystone (OPA) from the shaly facies at the Mont-Terri-URL have been experimentally investigated at the GRS laboratory. Both COX and OPA argillaceous formations are results of a specific geological history that lasted hundreds of millions of years, beginning with deposition and aggregation of fine-grained particles in sea water, followed by sedimentation and consolidation with a concurrent expelling of porewater, development of diagenetic bonds between mineral particles, and other processes /AND 05/, /NAG 02/, BOC 10/. They have been highly consolidated to porosities of 14-18 %. The pore sizes mainly range from nanometer scale in between the parallel platelets of the clay particles to micro- and mesometer scale between solid particles. The fraction of pores smaller than 20 nm amounts to about 60-80% for the clay rocks. On average, the COX claystone contains 25-55% clay minerals, 20-38% carbonates and 20-30% quartz, while the OPA clay-schist has higher clay contents (58-76%), less carbonates (6-24%) and quartz (5-28%). Because of the relatively high clay components, both the investigated claystones can be referred as clay rich. The claystone matrix contains accessory minerals but mainly clay, which consists of particles with strongly adsorbed interlayer water and adsorbed water at the external surfaces. In large pores is bulk water mobile.

3.2 Fracturing-induced permeability

Mechanical damage and induced permeability changes were determined on COX claystone samples under triaxial compression stresses, whereby deformation of the samples, gas permeability and wave velocity through them were recorded. Details of the tests and results are given in /ZHA 15b/.

Fig. 3.1 shows a typical example of the stress-strain-permeability response of the clay-stone and a conceptual mode of crack evolution during triaxial loading. The establishment of this mode takes into account the micro tomography of localized damage and deformation made on the same claystone during triaxial loading /VIG 11/, and also the typical fracture pattern observed on the samples after testing. The stress-strain-permeability behaviour may be characterized in four sequential stages.

I	II	III	IV
closure of existing microcracks	initiation/growth of microcracks	crack connection percolation threshold	macrofracturing permeability increase
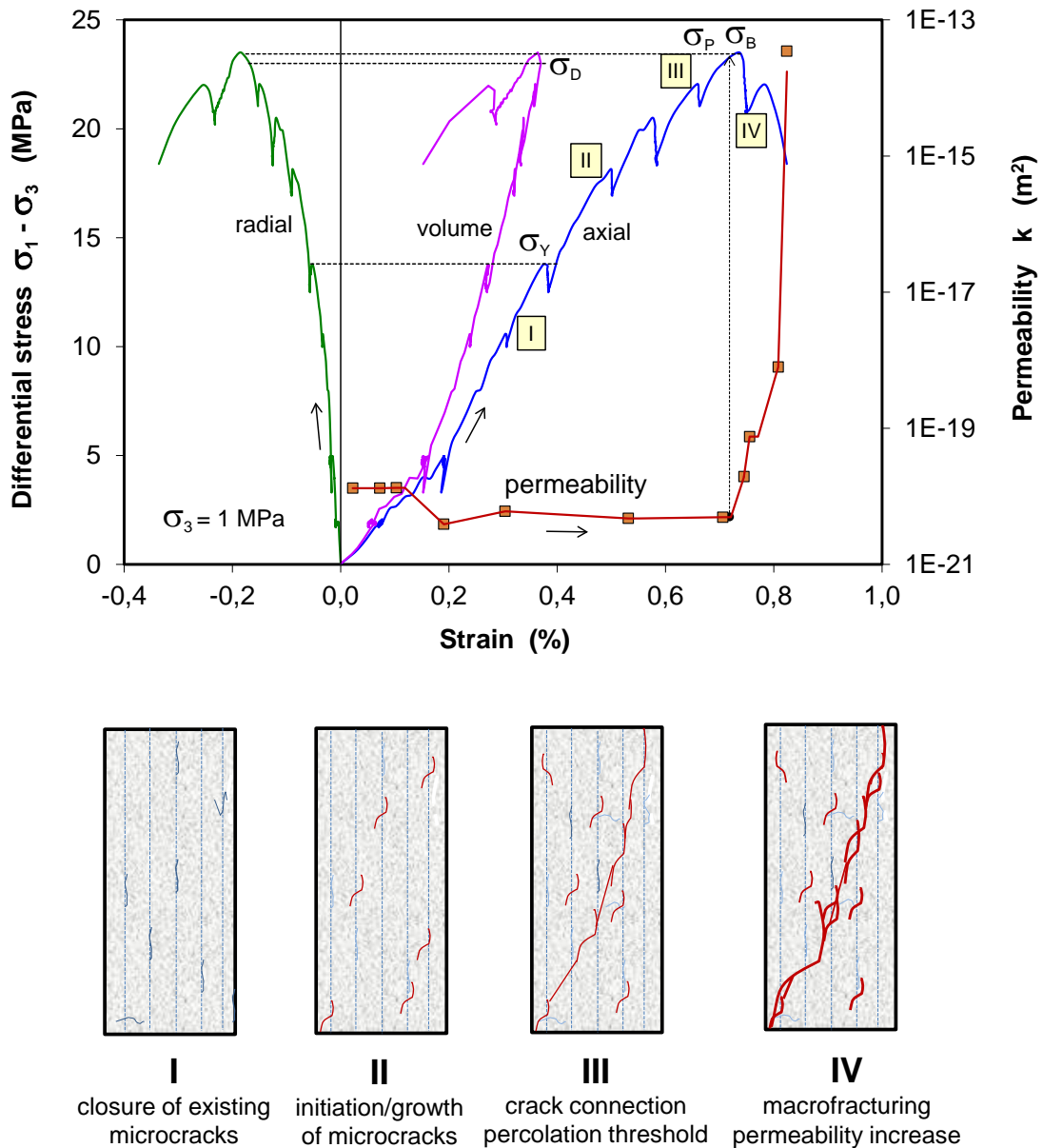
Fig. 3.1   Stress-strain-permeability behavior of COX claystone including thresholds of yield σ_Y, dilatancy σ_D, percolation σ_P, and peak failure σ_B

I.   The claystone deforms relatively largely in the very beginning of the load due to the closure of the remaining microcracks, and then it follows a linear axial compression ε_1, radial extension ε_3 and volumetric compaction ε_v until a deviation appears at a differential stress σ_Y. The yield point indicates onset of microcracking, as detected by shear wave velocity on the Opalinus claystone /POP 07/. The yield stress recorded is about 60 % of the peak failure strength σ_B.

II.   Further increasing the stress results in a non-linear plastic hardening process with an overall volume compaction. This implies that the pre-existing and newly-created microcracks mostly keep closed during shearing /VIG 11/. As a result, the initially very low permeability does not change much.

III.   When the deviatoric stress reaches a high value σ_D close to the peak σ_B, the volume compaction changes over to dilatation due to crack opening. Exceeding the dilatancy threshold, the microcracks grow and propagate much faster with further loading. Just as some of the neighbouring microcracks coalesce to a continuous network through the sample, the permeability begins to rise. The corresponding differential stress σ_P is usually called percolation threshold. It occurs shortly before the peak failure at low lateral stresses $\sigma_3 \leq 1$ MPa but shortly after the peak at high lateral stresses. So it is reasonable to assume $\sigma_P \approx \sigma_B$.

IV.   Beyond the fracture percolation during the post-failure phase at the residual stress, the connection of the cracks results in a spontaneous increase of the permeability, accompanied with very small dilatancy. After the crack connectivity is sufficiently developed, further deformation is mainly dominated by fracture slipping, so that the increase of the fracturing-induced permeability is limited.

The damage and the resulting permeability change are dependent on the lateral confining stress. As the confining stress is increased, the inner structure of the claystone becomes more compacted and fracturing is inhibited. The deformation becomes progressively from brittle to ductile, as shown in Fig. 3.2. Because high confining stresses suppress the initiation, growth and propagation of cracks, the compaction phase before the onset of dilatancy lasts longer and the fracture percolation occurs later on at high lateral stresses. The increased permeability is also relatively low at high confining stresses. Generally, the critical stresses and strains at yield, dilatancy, percolation, and peak failure increase with increasing the lateral confining stress.
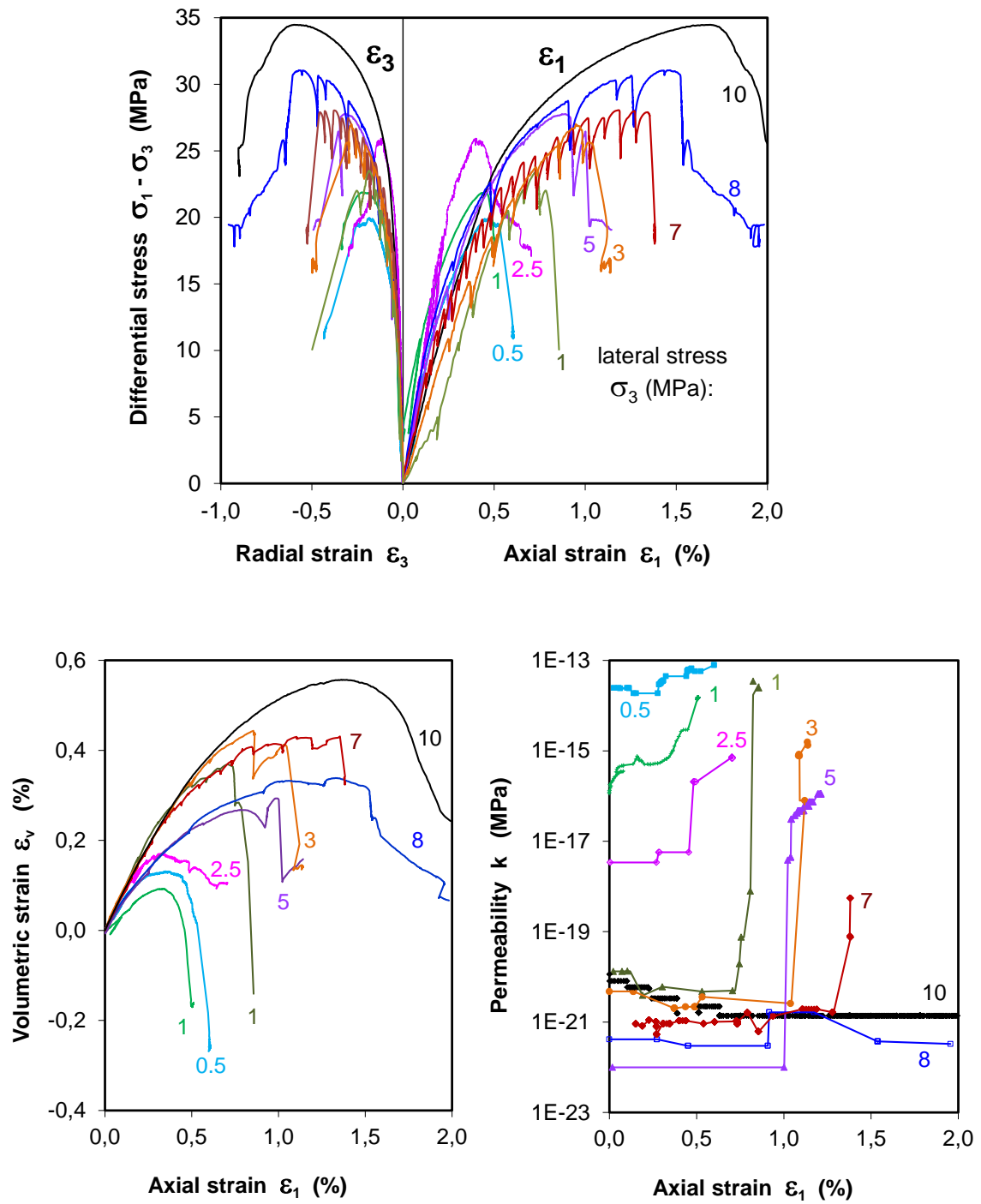
Fig. 3.2   Dependency of the deformation and permeability of COX claystone on lateral confining stress

The critical stresses at yield, dilatancy, percolation, and peak failure increase with increasing confining stress, as shown in Fig. 3.3. The peak failure strength can be described by the Hoek-Brown (HB) and Mohr-Coulomb (MC) criteria

HB: $\quad\sigma_B = (m \cdot \sigma_c \cdot \sigma_3 + s\sigma_c^2)^{1/2}$ (3.1)

where the uniaxial compression strength σ_c = 19 MPa, the parameter m = 4, and s = 1 are estimated for the claystone; and

MC: $\quad\sigma_B = 2 \cdot c \cdot tan\left(45° + \frac{\varphi}{2}\right) - \sigma_3 \cdot \left[1 - tan^2\left(45° + \frac{\varphi}{2}\right)\right]$ (3.2)

where the cohesion c = 6 MPa and the internal friction angle φ = 26° are determined.
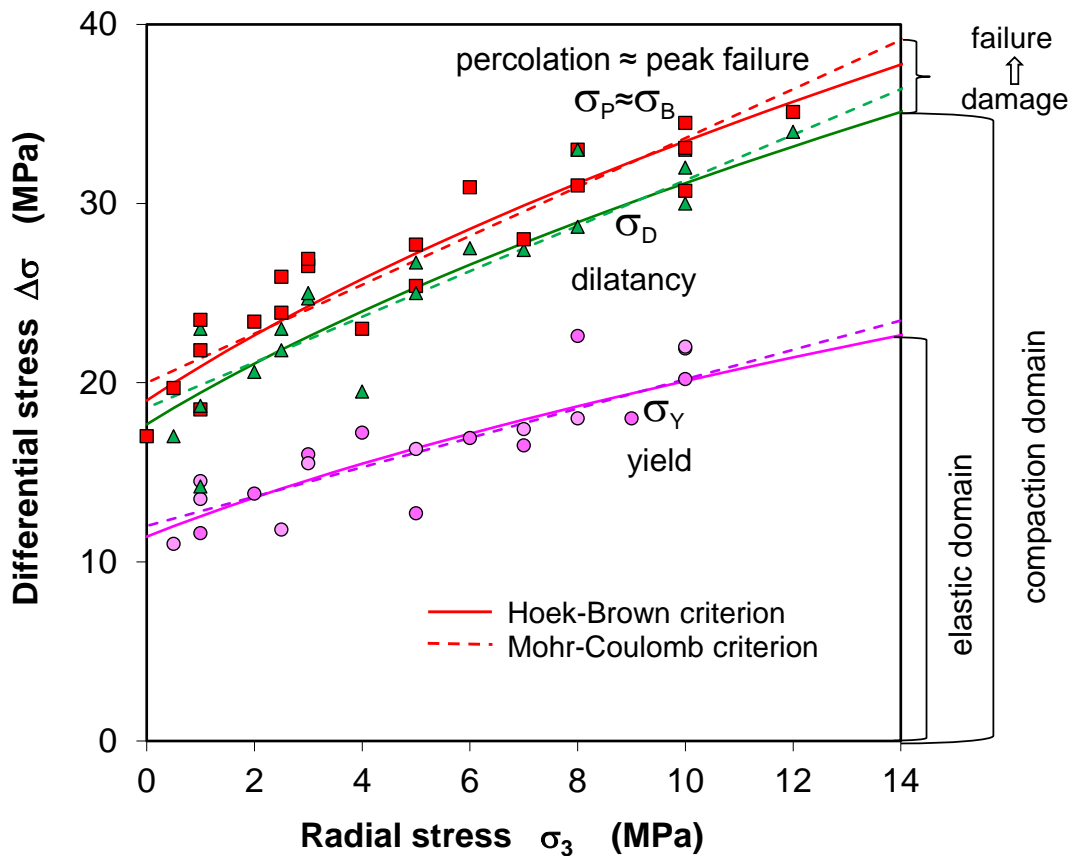
Fig. 3.3   Stress boundaries of yield, dilatancy, percolation and peak failure of the claystone

It appears that the ratios of the yield and dilatant stresses to the peak strength are more or less constant, being independent of the confining stress. The average values are obtained as σ_Y/σ_B = 0.60, σ_D/σ_B = 0.93, and $\sigma_P \approx \sigma_B$.

These stress boundary conditions are helpful for characterising the state of the rock subjected to any given stress state. For stresses below the yield boundary σ_Y, the rock

behaves elastically. Above the yield boundary but below the dilatancy boundary, $\sigma_Y <$ $(\sigma_1-\sigma_3) < \sigma_D$, the overall volume is under compression without damage even though some microcracks are created. If the dilatancy boundary is violated, $(\sigma_1-\sigma_3) \geq \sigma_D$, the microcracks grow and coalesce with increasing deviatoric stresses. When the stress reaches the percolation and failure boundary, $(\sigma_1-\sigma_3) \geq \sigma_P \approx \sigma_B$, a crack network builds up leading to a spontaneous increase of the permeability and to failure.

The fracturing-induced permeability is contributed by the connectivity and the conductivity of cracks and can be expressed in a general form by $K_g = K_f \cdot P$, where K_f is the ultimate permeability of the fractured rock with perfectly interconnected cracks and P is the percolation probability defining the fraction of cracks belonging to the conducting part of a network. The ultimate fracture permeability increases with decreasing the minor principle stress σ_3 by $K_f = K_o \cdot exp(-\gamma\sigma_3)$, where K_o is the permeability at zero minor stress and γ being a parameter characterizing the dilatability of the interconnected cracks. In addition, the percolation probability is assumed to be a function of crack dilatancy: $P = [1-exp(-\Delta\varepsilon_D/\varepsilon_P)]$, where $\Delta\varepsilon_D = |\varepsilon_v - \varepsilon_P|$ is the volumetric dilatancy with reference to the volumetric strain ε_P at the percolation threshold. At $\varepsilon_v = \varepsilon_P$, $P = 0$, the connectivity of the cracks is zero. With increasing dilatancy the cracks tend to a full connection, $P \rightarrow 1$ as $\varepsilon_v \rightarrow \infty$. In fact, a sufficiently high connectivity of the cracks for a high and final permeability can develop at very small dilatancy, for instance, $\Delta\varepsilon_D < 0.1$ % as observed on the claystone in the tests. The final expression shows the relationship of fracturing-induced permeability to the minimum principle stress and dilatancy

$$K_g = K_o exp(-r\sigma_3)\left(1 - \exp\left(-\frac{\Delta\varepsilon_D}{\varepsilon_P}\right)\right) \tag{3.3}$$

The values of the parameters are estimated to be $K_o = 3 \cdot 10^{-13}$ m^2 and $\gamma = 1.9$ MPa^{-1}.

The model predictions for the permeability evolution at exceeding dilatancy are compared in Fig. 3.4 with the data obtained during fracturing at different lateral stresses. It is evident that the fracturing-induced permeability with the spontaneous increase due to the formation of a continuous crack network and the subsequent considerable slow-down of this increase with further development of the network can be reasonably described by the model. However, more experiments are needed to confirm the parameters obtained here.
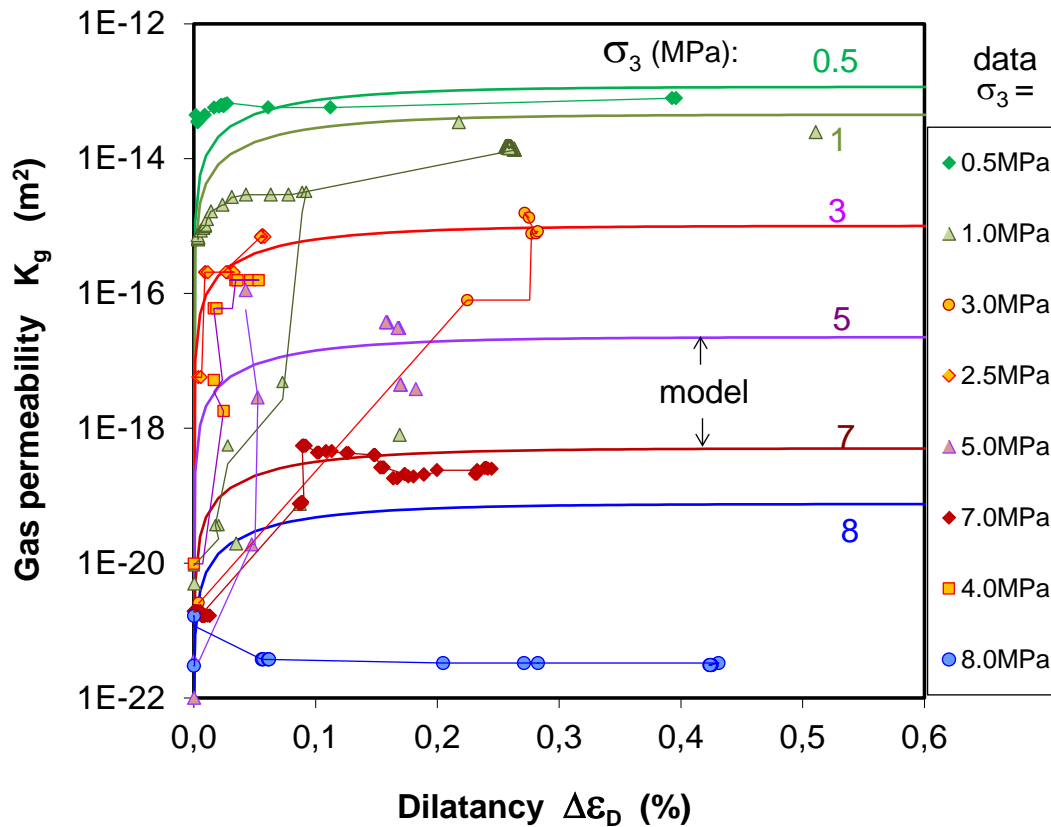
Fig. 3.4   Prediction of the fracturing-induced permeability in the claystone using the percolation model

3.3   Fracture closure and permeability variation

The compaction behaviour of damaged claystone was investigated under hydrostatic and deviatoric load conditions. Fig. 3.5 shows results of the hydrostatic compaction on two fractured COX samples. It can be seen that a) the increase of hydrostatic stress closes up the fractures and hence decreases the fracture permeability; and b) the subsequent unloading leads to some elastic reopening of the fractures without significant reversibility of the permeability. It suggests that parts of the fractures have been permanently closed and disconnected from the pathway. The quantitative differences are caused by different factors such as size, geometry, roughness, and connectivity of the cracks.
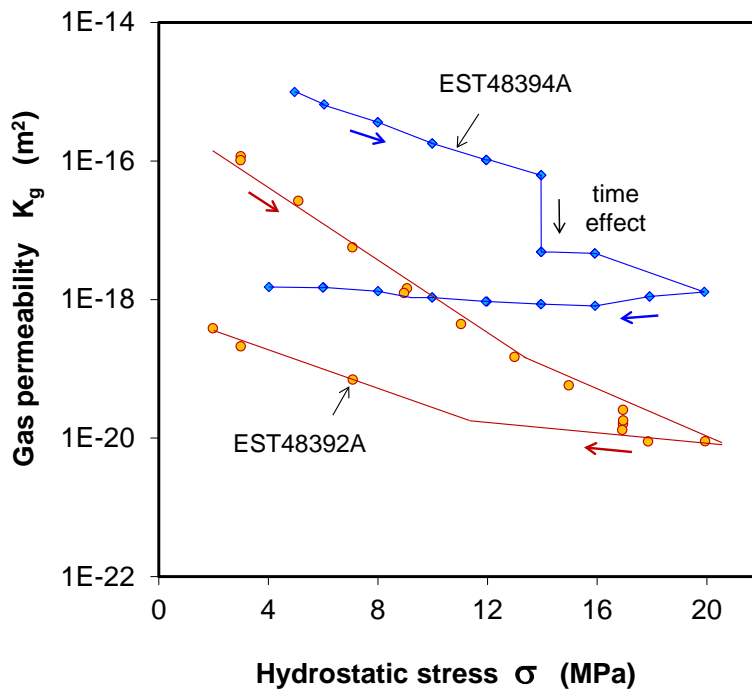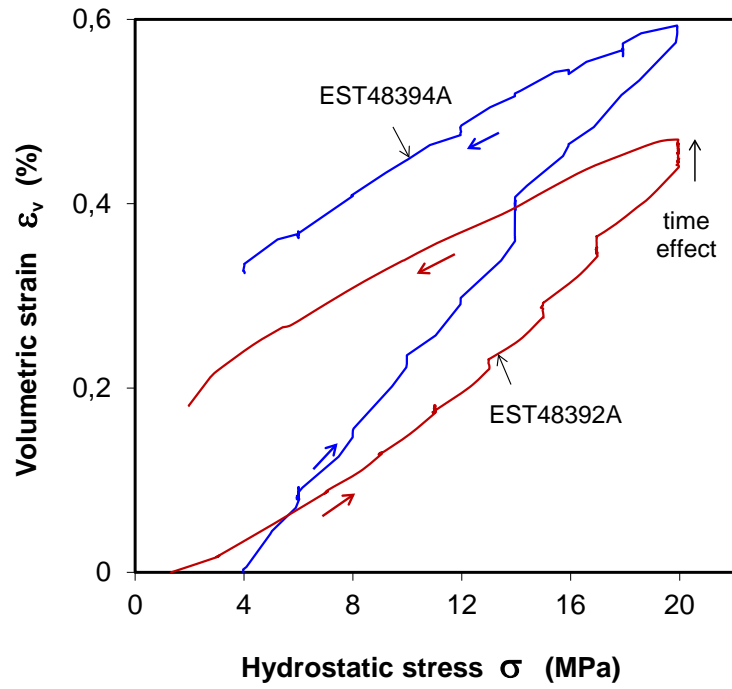
Fig. 3.5   Volume compaction (a) and permeability changes (b) of fractured COX
            claystone during hydrostatic loading and unloading

Fig. 3.6 presents the other test examples in terms of fracture closure vs. normal stress
and the corresponding permeability reduction. The fracture closure evolves faster at
large apertures in the initial loading stage and then closure rate decreases with in-

creasing stiffness at smaller apertures. Corresponding to the fracture closure, the gas permeability decreases significantly by 3 to 5 orders of magnitude, from the initial values of 10^{-13} m^2 down to 10^{-16} m^2 at large initial apertures (1.1–1.7 mm) and from 10^{-15} m^2 down to 10^{-18}–10^{-20} m^2 at small initial apertures (0.3–0.6 mm).

Fig. 3.6   Fracture closure as a function of normal stress (a) and permeability reduction with fracture closure (b)

The fracture closure can be approximated by an exponential equation of effective normal stress:

$$\Delta b = b_o \left(1 - \exp\left(-\alpha \sigma_n^{\beta} \right) \right) \tag{3.4}$$

where Δb is the aperture closure, b_o the initial aperture equivalent to the maximum aperture closure, σ_n the effective normal stress, α and β are constants. If the stress tends to infinity, $\sigma_n \to \infty$, the fractures will be f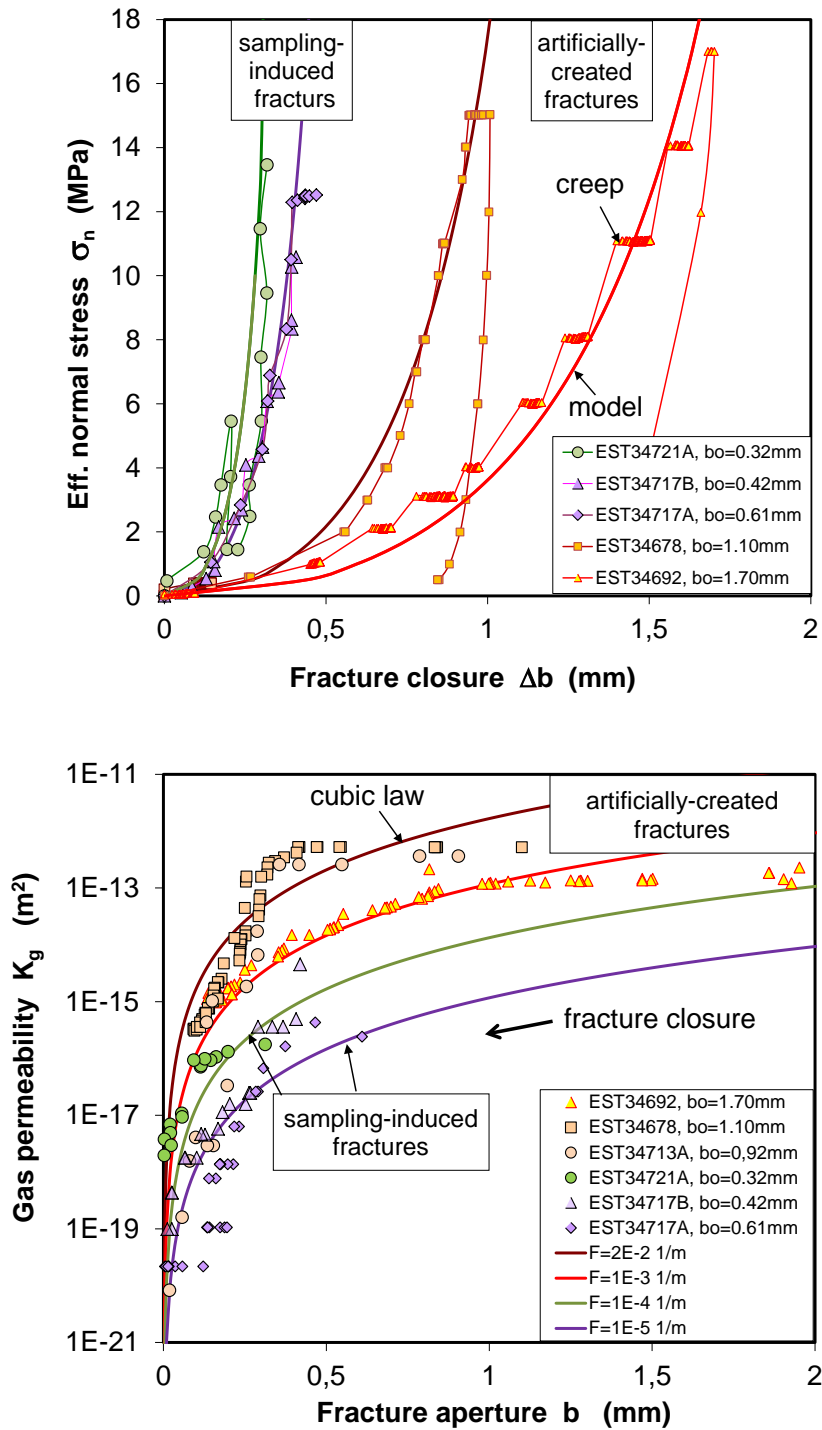ully closed, $\Delta b \to 0$. Fitting the data derives a unique set of the parameters $\alpha = 0.3$ and $\beta = 0.5$ for the fractured samples.

The permeability reduction with fracture closure can be described by the cubic law:

$$K_g = \frac{R}{12s} b^3 = \frac{F}{12} b^3 \tag{3.5}$$

where b is the average fracture aperture ($b = b_o - \Delta b$), s is the mean fracture spacing, R is the roughness factor of the fracture surfaces, and F is the R/s represents an integrated character of the set of fractures. As the fracture aperture b decreases to zero, K_g tends to zero. Fitting the data yields different F-values of 1×10^{-5} up to 2×10^{-2} m^{-1} due to the different characteristics of the fractures in samples.

Supplementary to the hydrostatic recompaction, effects of deviatoric loading were also examined along multistep paths. Fig. 3.7 shows a typical example of the tests in terms of differential stress vs. axial and radial strain ($\Delta\sigma - \varepsilon_1$; $\Delta\sigma - \varepsilon_3$), and volumetric strain and permeability vs. axial strain ($\varepsilon_v - \varepsilon_1$; $k - \varepsilon_1$). The stress-strain curves show that a) the post-failure behaviour at each elevated lateral stress is quite similar to the behaviour under pre-failure conditions, i.e. non-linear axial compression, radial extension and volume compaction until the onset of dilatancy at σ_D; b) then the stress does not increase much because further deformation is dominated by plastic sliding of the fractures; c) the maintaining dilatancy stress σ_D represents the maximum residual stress-bearing capacity σ_R of the fractured claystone; d) the residual strength increases with increasing lateral stress σ_3.
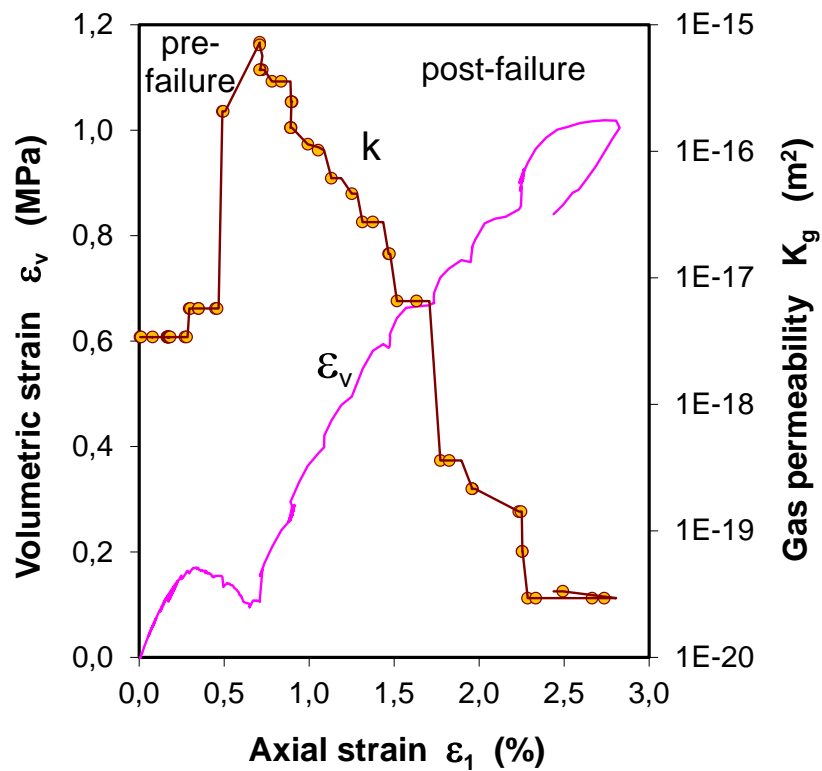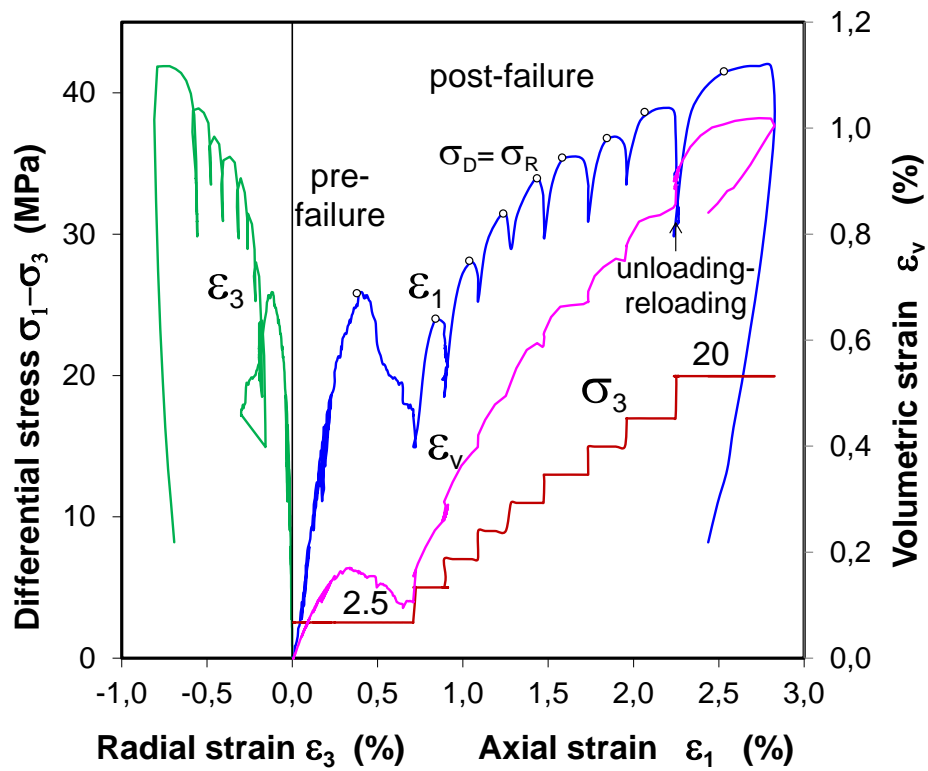
Fig. 3.7   Stress-strain-permeability behaviour of fractured claystone during multistep
deviatoric loading

The residual strength of the damaged claystone is non-linearly related to the minor principle stress (Fig. 3.8). This can reasonably be described by the Hoek-Brown criterion (Eq. 3.1). Because of the different intensities of damage in the samples, the residual strength varies within a relatively large bandwidth. The boundaries of the scattered data can be defined by the respective parameters: σ_c = 7 MPa and m = 5 for the lower boundary; σ_c = 11 MPa and m = 9 for the upper one; σ_c = 9 MPa and m = 7 for the mean curve; and s = 0 for all of them. The lower boundary shall be applied for the residual strength of the heavily damaged clay rock near drift walls, while the upper one for the less damaged rock mass in the far-field.
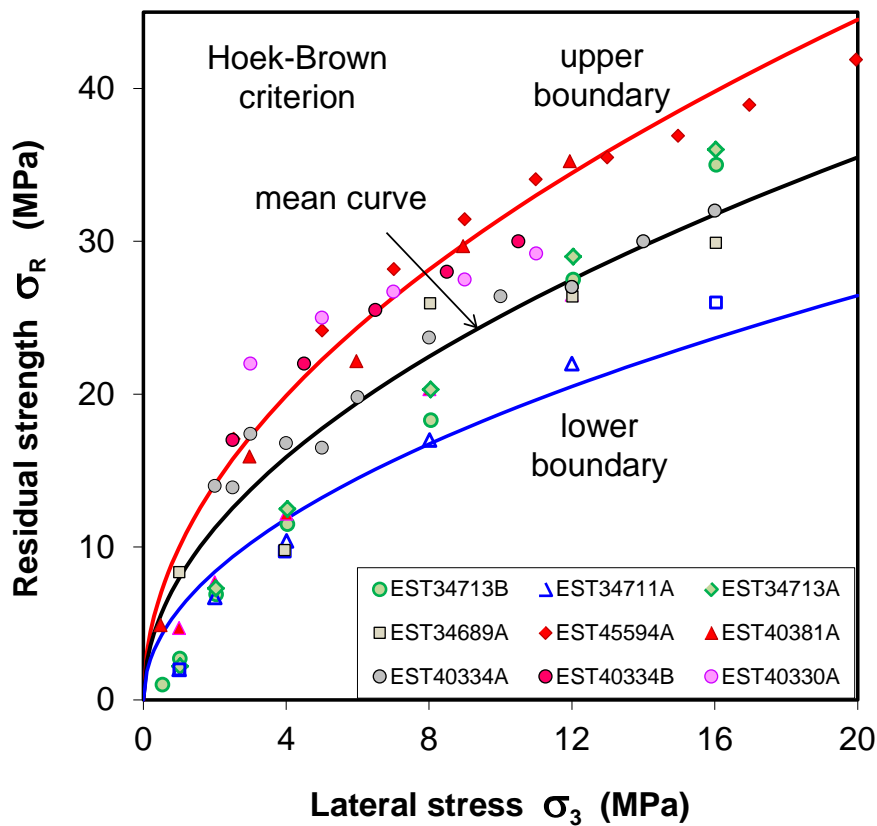
Fig. 3.8   Residual strength of fractured COX claystone as a function of minor confining stress

In correspondence with the closure of fractures or the volume compaction before onset of dilatancy at each lateral stress, the permeability decreases. Dilation with further deviatoric loading does not raise the permeability significantly. This behaviour is different from the spontaneous permeability increase observed in the intact claystone (cf. Fig. 3.1). The permeability in fractured claystone is largely determined by the amplitude and

31

distribution of the apertures and surface roughness of the interconnected fractures along the flow path. It can also be approximated by the cubic law in terms of permeability K_g as a function of volumetric strain ε_v

$$K_g = D(\varepsilon_R)^3 = D|\varepsilon_F - \varepsilon_v|^3 \tag{3.6}$$

where ε_F is the maximum dilatancy reached after sufficient fracturing, $\varepsilon_R = |\varepsilon_F - \varepsilon_v|$ represents the residual voids in the fractures, and D is a parameter characterising the rock state after fracturing, $D = K_f/(\varepsilon_F)^3$. As the residual fracture void tends to zero, $\varepsilon_R \to 0$, the fracture permeability disappears. Fig. 3.9 shows a comparison of the predicted permeability based on the cubic law and the measured permeability as a function of the residual volumetric strain during the hydrostatic compaction and multistep deviatoric compression. The parameter D is derived from the measured ε_F and K_f data to lie in a range of $7 \cdot 10^{-10}$ m^2 to $1 \cdot 10^{-7}$ m^2. A satisfactory agreement between the model and the data can be stated for the compaction phases during the deviatoric loading.

Hydrostatic compaction
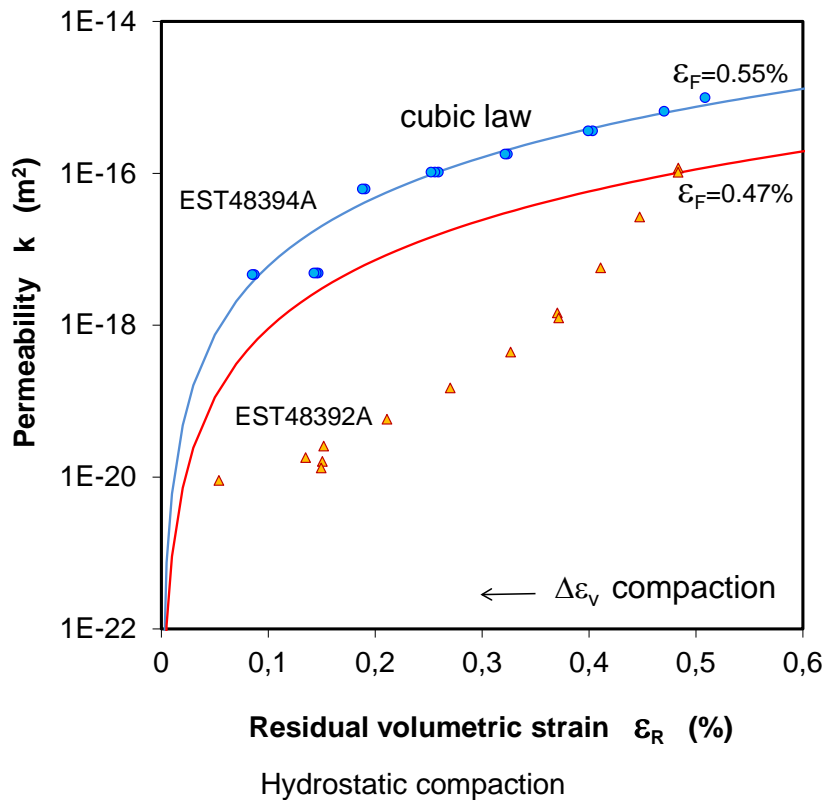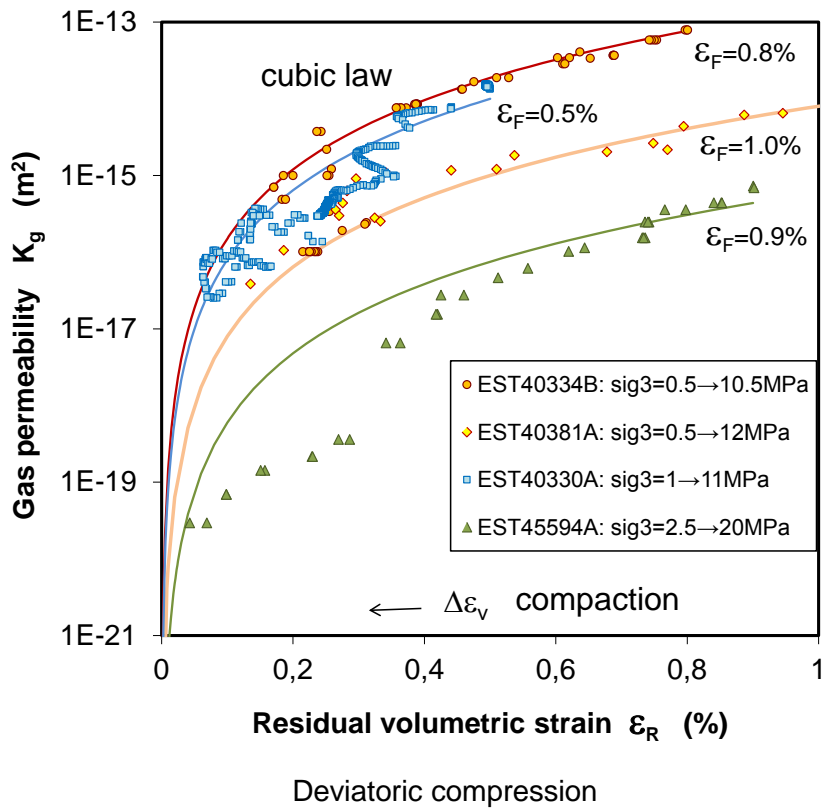
Fig. 3.9   Variation in permeability of fractured claystone with volume compaction during hydrostatic loading (a) and multistep deviatoric loading (b)

3.4   Water conductivity of fractured claystone

As water enters and flows through fractures in claystone, the clay matrix can take up a great amount of the water and expand into the interstices. The water-induced swelling, weakening and slaking of the claystone leads to sealing of the fractures. Consequently, the hydraulic conductivity of the fractured claystone decreases.

Fig. 3.10 illustrates the combined impact of compression and water flow on the sealing of fractures. The recorded radial strain normal to the fracture planes shows that each load increase causes an immediate closure of the fractures. Because of the high swelling capability of the claystone, the fractured claystone expands rather than compacts followed at loads up to 10 MPa. The externally observed expansion indicates high local swelling pressures acting in contacting areas between fracture walls, where the material must expand more into the stress-free fracture voids than elsewhere. Additionally, the clay matrix near the fracture walls contacting with water becomes weakening, slaking and filling the voids. The sealing of the fractures leads to a decrease in permeabil-

ity. After stepwise increasing the load to 13 MPa over seven months, a very low water permeability of $2\cdot10^{-19}$ m^2 was reached, which is close to that of 10^{-20}–10^{-21} m^2 for the undisturbed claystone. The permanent sealing of fractures by swelling and slaking of clay matrix is clearly visible on the pictures. The fractures with sharp wall edges disappeared due to the water-enhanced weakening effects.
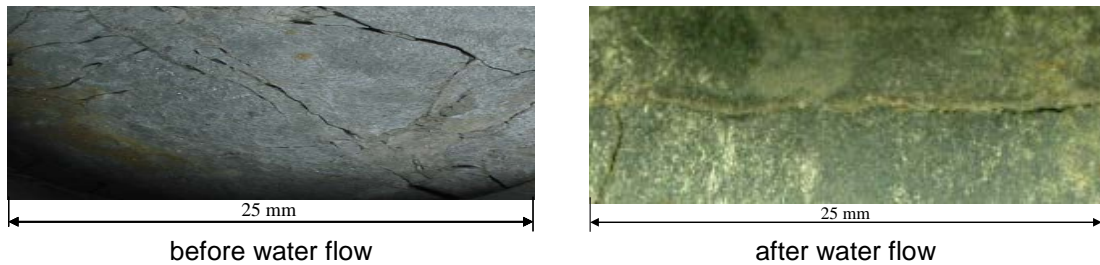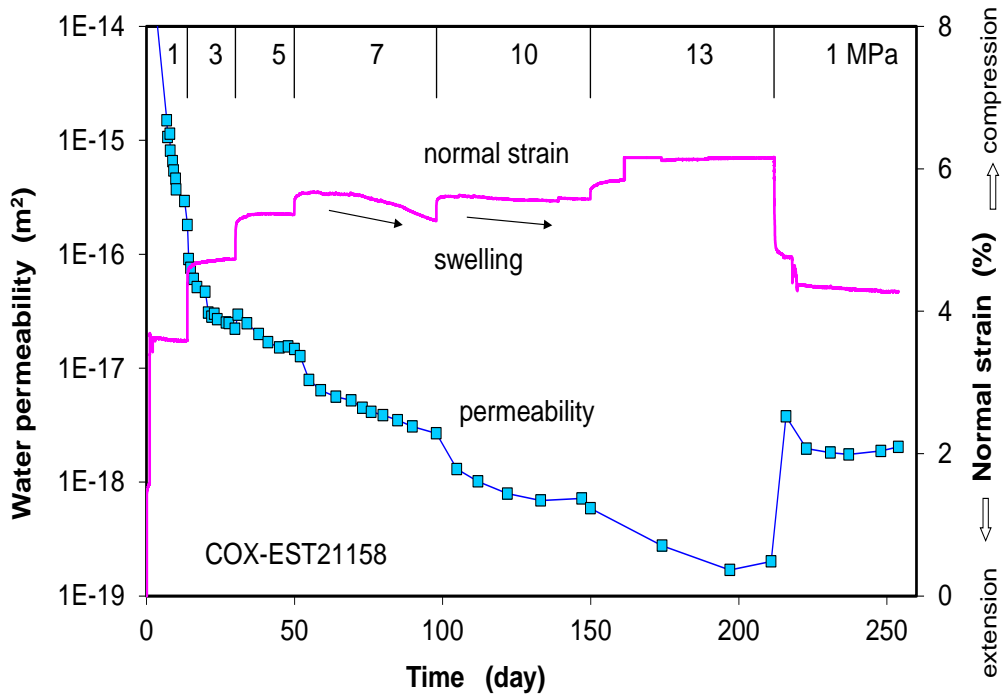
Fig. 3.10   Sealing of fractures in COX claystone under various confining stresses

Fig. 3.11 shows the long-term evolution of water permeability obtained on fractured COX and OPA claystones under low confining stresses of 2–3.5 MPa and temperatures of 20–90 °C. They were flowed with synthetic porewater through over more than 3 years. As soon as the water was supplied, the high initial gas permeability of $3\cdot10^{-12}$ m^2 dropped immediately by five to seven orders of magnitude down to 10^{-17} – 10^{-19} m^2, depending on the fracture intensity of each sample. At each load level, the permeability decreased gradually with time. The influence of the confining stress on the permeability variation was not significant in the testing range. Interesting is that the pre-heating up

to 150 °C did not hinder the sealing process of the fractures in the claystone. During the heating/cooling cycle and water flow, the permeability decreased with time down to a very low level of 10^{-19} m^2. It is evident that the self-sealing of fractures is not affected by the applied thermal load. The final permeability values after 3 years are very low at $3 \cdot 10^{-20} - 7 \cdot 10^{-21}$ m^2, being the same order of magnitude as that of the intact clay rock.
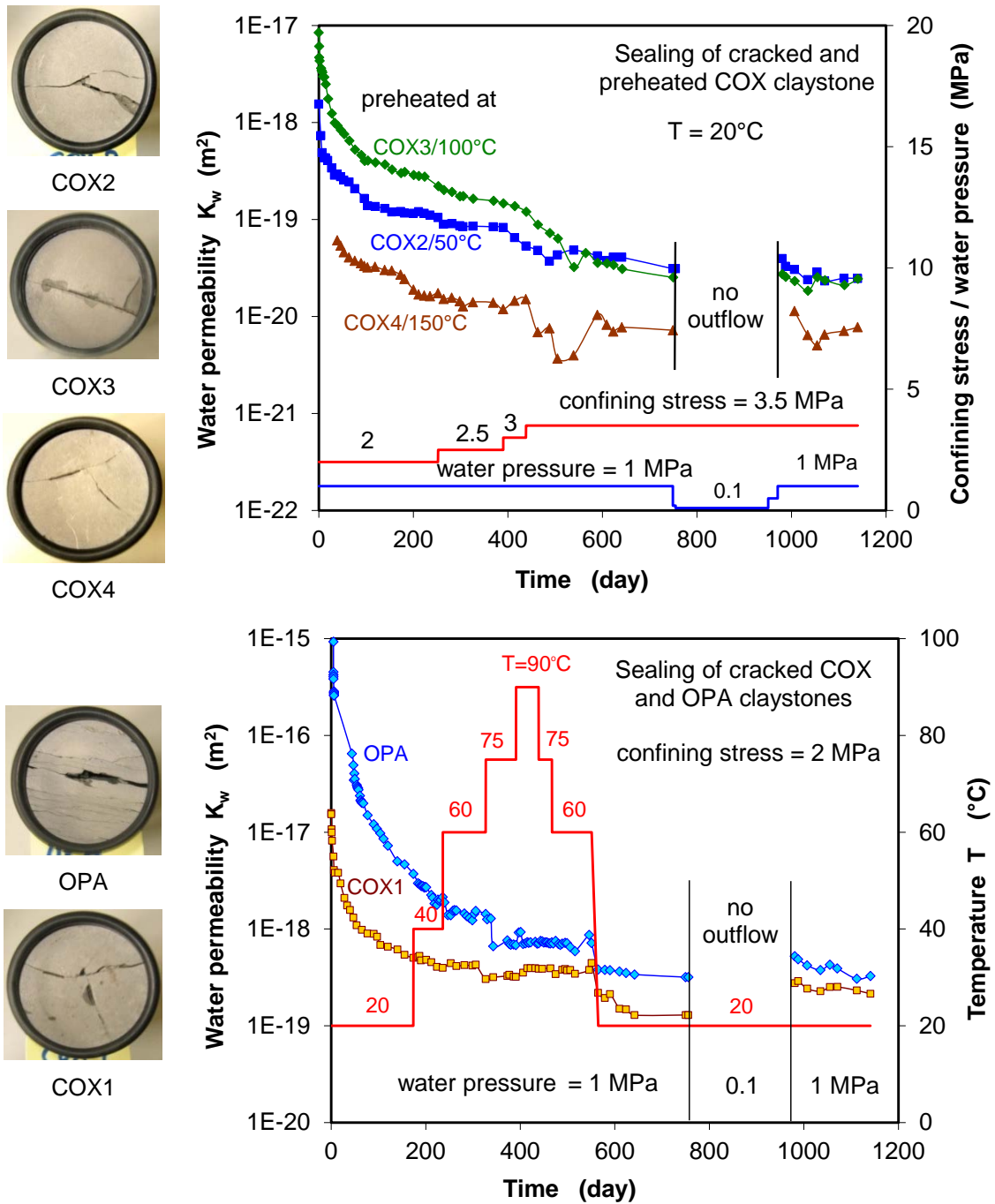
Fig. 3.11 Long-term evolution of water permeability obtained on fractured claystones under confining stresses of 2 to 3.5 MPa and temperatures of 20°C to 90°C

As observed in the tests, the water permeability decreases with the effective confining stress ($\sigma_{eff} = \sigma - p_w$). The permeability values obtained at the end of each stress stage are summarized in Fig. 3.12 as a function of confining stress. The $log(K_w) - \sigma_{eff}$ dataset for each sample can be approximated by an exponential equation

$$K_w = K_{wo}exp(-\beta \cdot \sigma_{eff}) \tag{3.7}$$

where K_{wo} is the initial water permeability at zero confining stress $\sigma_{eff} = 0$ and β is a parameter characterising the compressibility of the water pathways. While K_{wo}-values are estimated in the range of 2×10^{-16} to 4×10^{-20} m^2 depending on the fracture features of each sample, a unique β-value of 0.6 MPa^{-1} is obtained for all tested samples.
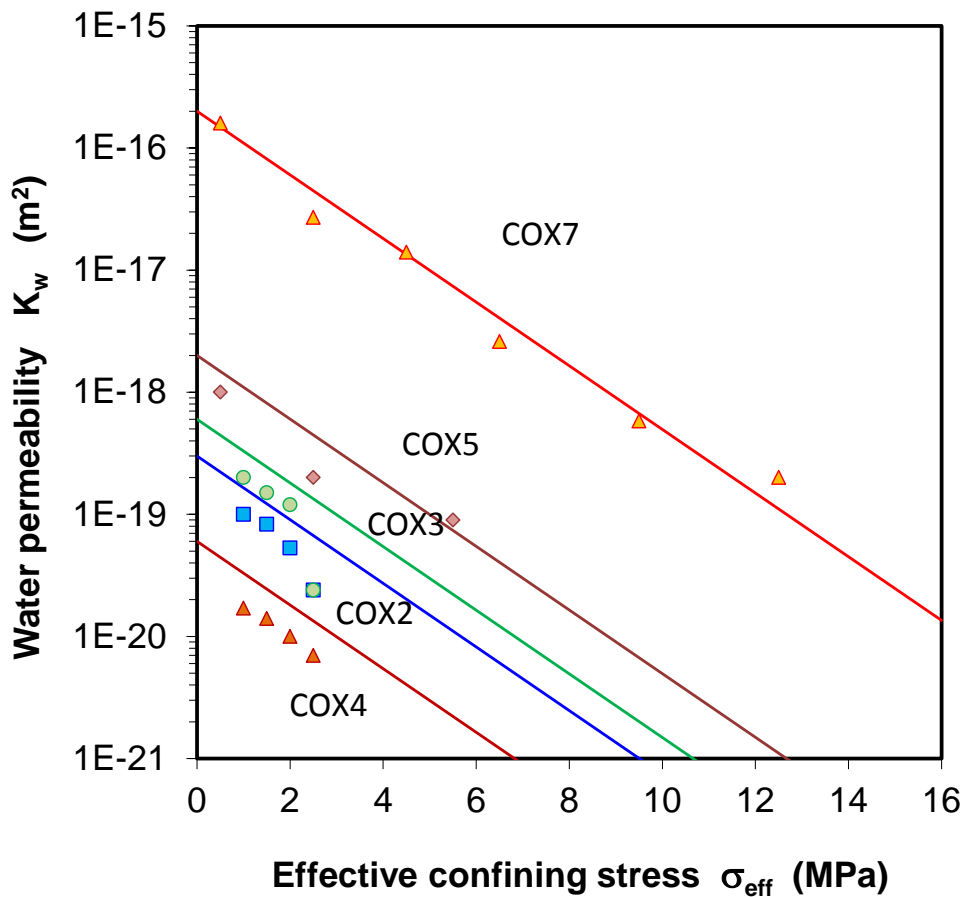
Fig. 3.12   Dependence of water permeability of fractured claystone on effective confining stress

3.5 Gas migration in water-saturated and resealed claystone

The highly-consolidated and water-saturated clay rocks are practically impermeable for advective transport of gas under normally-encountered pressure gradients. However, the EDZ may act as conduits for preferential gas flow, depending on the resealed state. Particularly after water saturation, gas entry into the resealed fractures needs driving forces to overcome the capillary thresholds and to generate migration pathways.

Fig. 3.13 presents the measured gas breakthrough pressures of the highly-resealed COX and OPA samples with very low water permeabilities of 10^{-19}–10^{-21} m^2 (cf. Fig. 3.9). It can be seen that gas entry and penetration into the water-saturated and highly-resealed claystones needs high gas pressures to overcome the capillary thresholds, which are determined by the sealing intensity of the fractures under confining stress.

The advective gas flow through resealed claystone is accompanied by micro-fissuring and dilation of the generated fissures. Fig. 3.14 shows an example of the gas pressure impact. During the first stage with stepwise gas pressure increase from 2 to 4 MPa, compressive strains evolved progressively in all directions and no gas outflow was detectable. The subsequent pressure increase to 4.5 MPa inhibited the continuation of the radial compression. Further pressure increase to 5 – 7 MPa led to a slightly gradual dilatancy in radial direction, indicating a progressive gas penetration into some fissures. As the gas pressure was increased up to 8.3 MPa, a sudden dilatancy in all directions took place and gas outflow could be detected, suggesting the gas breakthrough.

As shown above, the gas breakthrough pressures measured are below the minor confining stress and thus below the fracturing criterion as shown in Fig. 3.15. This important finding implies that the EDZ, even when highly-resealed, will still have the capacity for gas migration with moderate pressures and thus contribute to avoid high pressure building up, so that the host rock is prevented from gas fracturing.
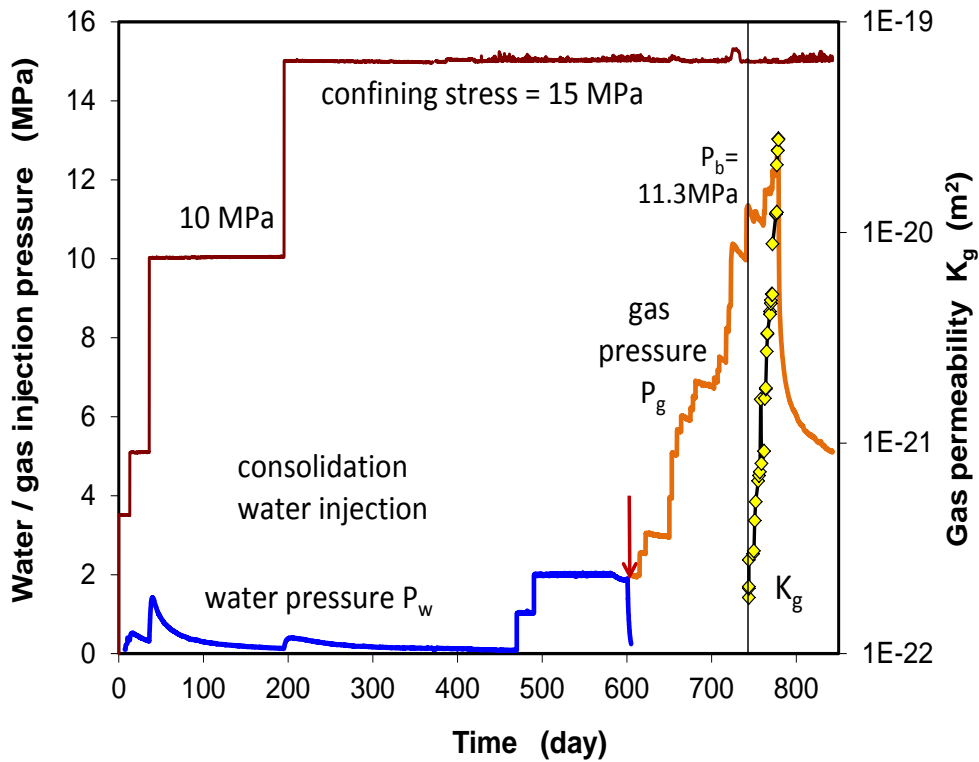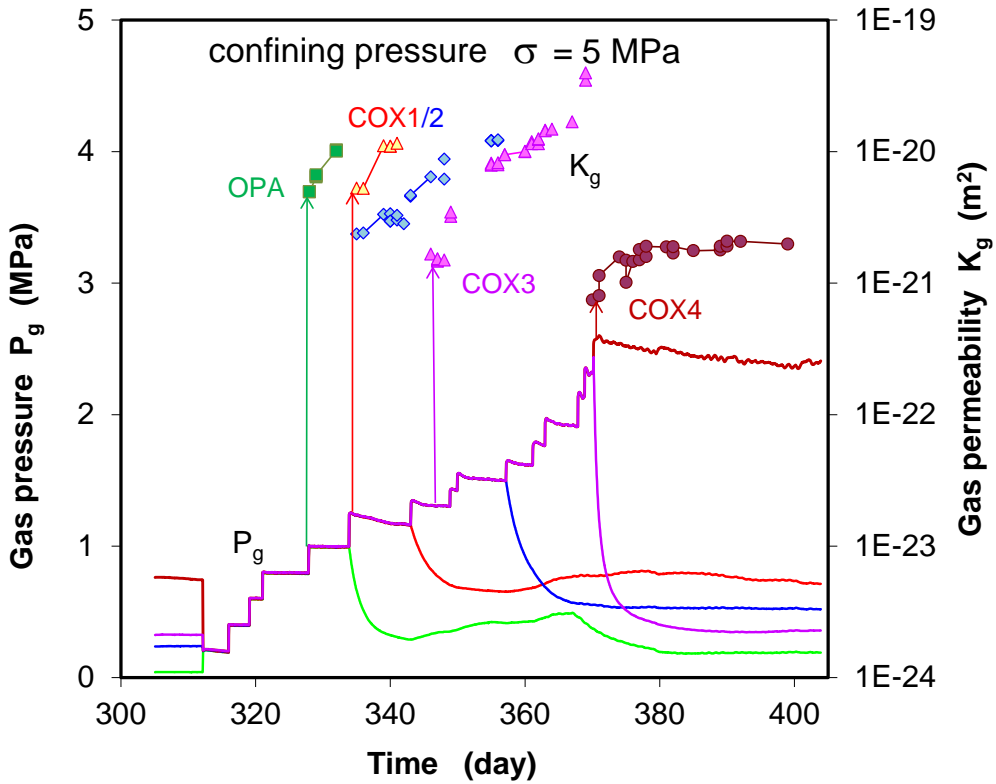
Fig. 3.13   Gas breakthrough pressures measured on highly-resealed claystones un-
der different confining stresses
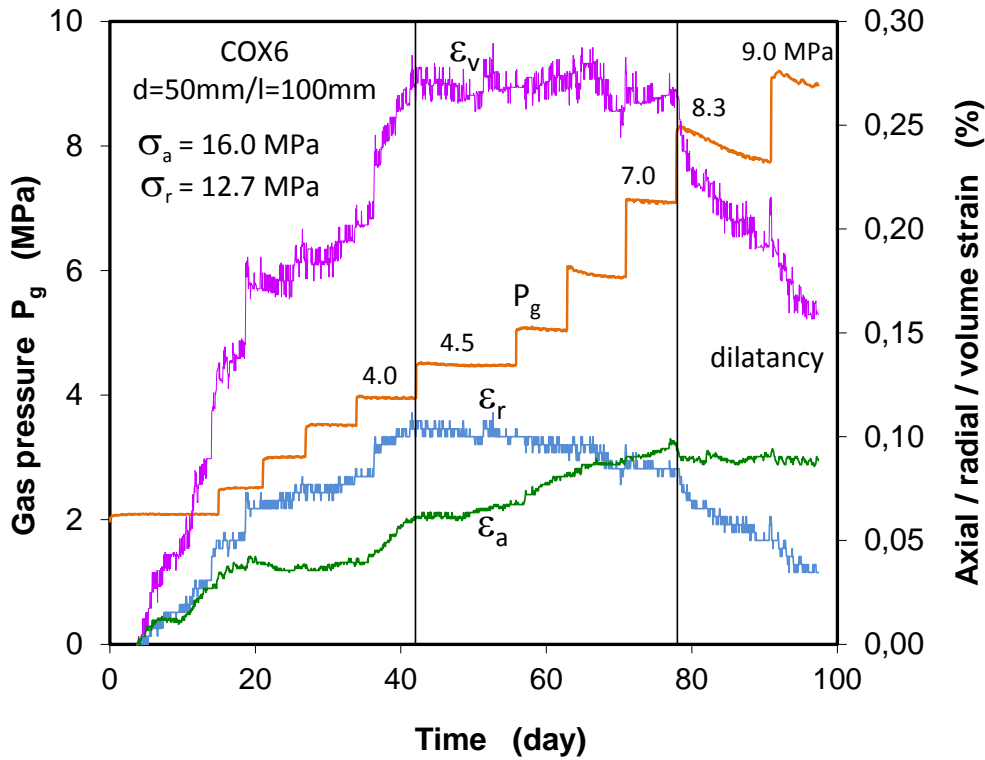
Fig. 3.14   Gas pressure induced dilatancy in a highly-resealed claystone sample un-
der triaxial compression

The gas breakthrough pressure of water-saturated and resealed claystone can be ex-
pressed as function of water permeability and minimum confining stress

$$P_b = B \cdot (K_{wo})^{-1/n} \cdot exp(-\gamma \sigma_{min}) \tag{3.8}$$

where P_b is the gas breakthrough pressure, K_{wo} is the initial water permeability at zero
minor principal stress $\sigma_{min} = 0$, B, n and γ are parameters. For the resealed claystone
with $K_{wo} = 5 \times 10^{-19}$ to 5×10^{-20} m² and for the intact claystone with $K_{wo} = 1 \times 10^{-20}$ m², the
parameters are estimated to be B = 2×10^{-7} MPa·m$^{2/3}$, n = 3 and γ = 0.2 MPa^{-1}. The
model prediction provides a reasonable agreement with the data (Fig. 3.15).

Further gas pressure rising can reopen more weakly resealed micro-fissures as well as
dilate the gas-occupied pathways. The growth of the micro-fissure networks allows gas
to flow easier, so that the effective gas permeability increases as shown in Fig. 3.16.
The drastic increase in gas permeability with increasing pressure represents a typical
percolation process of crack initiation, growth and coalescence.
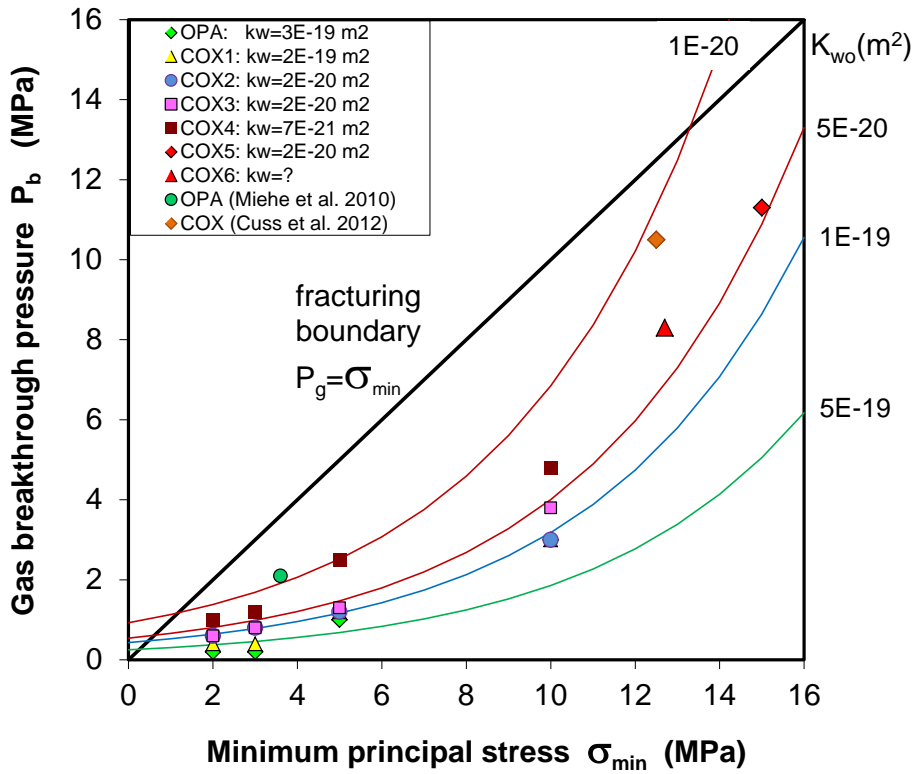
Fig. 3.15   Gas breakthrough pressure of highly-resealed claystones in comparison
with a conservative fracturing criterion without considering tensile strength
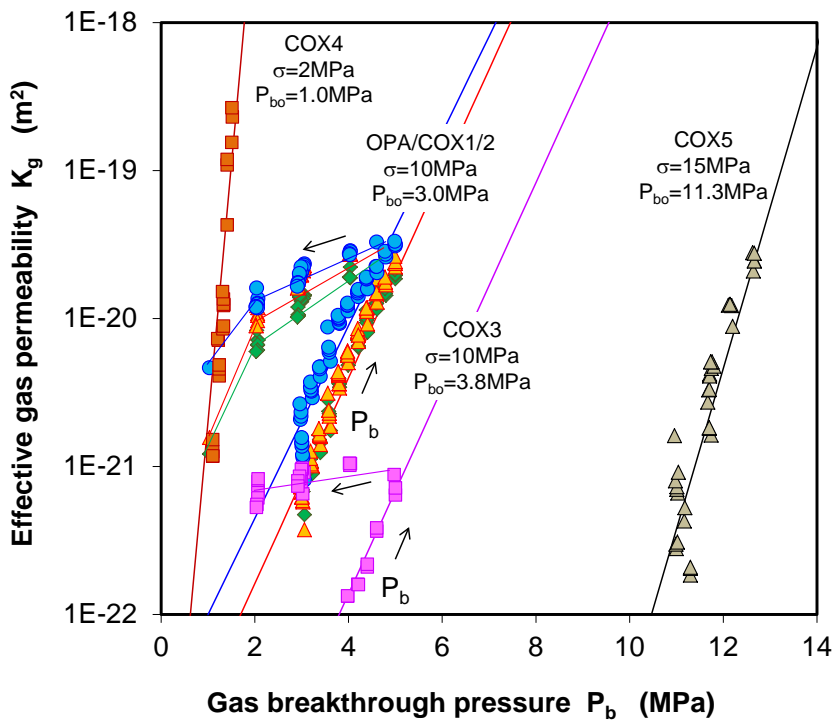
Fig. 3.16   Dependence of gas permeability on gas pressure after breakthrough

4 Geotechnical properties of sealing materials

Bentonite and bentonite-sand mixtures have being widely investigated for sealing of underground repositories in crystalline and clay formations. It is also considerable to utilize excavated claystone as a component of the seal mixture, because of its significant advantages such as chemical-mineralogical compatibility with the host rock, low costs of material preparation and transport, and many others. In order to meet specific requirements for the geotechnical properties of seals to be constructed in boreholes, drifts, ramps and shafts, the crushed claystone shall be mixed with bentonite in adequate fractions. The claystone-bentonite-mixture must be optimized with regard to the required sealing properties:

- sufficiently high density to ensure the safety relevant attributes;
- sufficiently high swelling capacity to seal possible gaps within the seal system and to support and even compress the surrounding EDZ;
- sufficiently low hydraulic conductivity to limit advective water transport and to retard migration of radionuclides;
- sufficiently low gas entry/breakthrough pressure to allow gas flow through without damaging the surrounding host rock and hence to guarantee the integrity of the natural and engineered barrier system;
- chemical-mineralogical compatibility with the host rock to keep the long-term chemical and hydraulic stability of the seal system.

The claystone-bentonite mixture was previously characterized in a certain extent /ZHA 10a/13a/14c/d/. The preliminary results from the compacted mixture show its favourable properties for sealing repositories in clay formations. In order to enhance the confidence in its suitability, the compacted claystone-bentonite mixture was more comprehensively characterized within the DOPAS project. Under identical test conditions, the compacted bentonite-sand mixture that has being investigated by ANDRA for drift sealing in the demonstration experiments PGZ /DEL 13/ and NSC /DEL 15/, was also characterized. So it is possible to compare both the mixtures with reference to the key sealing properties and the requirements on the seal material. The experiments and results obtained on these two mixtures are presented in this chapter.

4.1 Characteristics of investigated sealing materials

Crushed COX claystone produced by the drift excavation in the MHM-URL was used in the experiments. The delivered material was somewhat desaturated during storage to a residual water content of about 4.2 %. Two sets of grain sizes with grin diameters smaller than 10 mm and 5 mm were selected for testing. The aggregates were prepared by sieving the coarse grains through the corresponding sieves.

Expansive Na-bentonite MX80 from Wyoming in the USA was prepared to two sets of grain sizes of d < 0.5 mm and d < 2 mm. The bentonite bentonite contains 75 % montmorillonite, 15 % quartz and 10 % other minerals /KAR 08/. The delivered bentonite is relatively dry with a water content of 9.6 %. The prepared bentonite is mixed with crushed claystone for the claystone-bentonite mixture mainly in two ratios of COX/MX80 = 60/40 and 80/20. The bentonite-sand mixture tested by ANDRA in the borehole sealing experiment PGZ /DEL 13/ has a ratio of MX80/Sand = 70/30. The quartz sand has grains smaller than 2 mm.

Fig. 4.1 shows the grain size distributions of the selected materials as well as the mixtures. A picture of the crushed claystone with grains of d < 10 mm is also shown. The dry grain densities of the materials were measured to be ρ_s = 2.70 g/cm^3 for COX claystone, ρ_s = 2.78 g/cm^3 for MX80 bentonite, and ρ_s = 2.68 g/cm^3 for sand.

Water content:
COX claystone w = 4.2 %
MX80 bentonite w = 13.0 %
60COX+40MX80 w = 7.7 %
70MX80+30Sand w = 9.1 %

Crushed claystone
with grains d < 10 mm
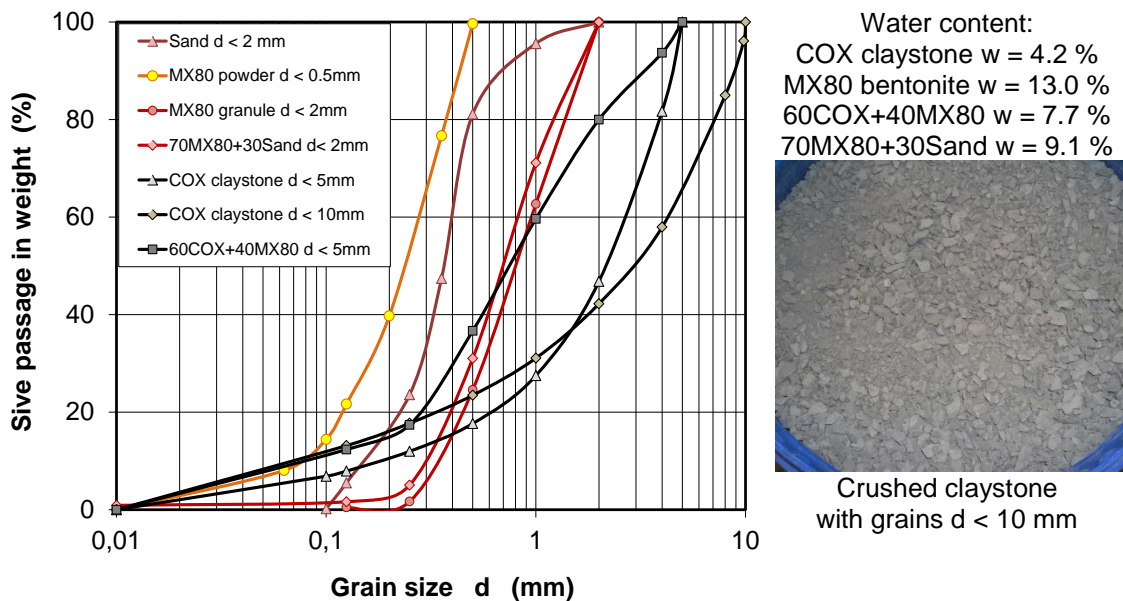
Fig. 4.1   Grain size distributions of crushed claystone, bentonite, sand and mixtures

42

In the previous experiments /ZHA 13a/, the crushed claystone with small grains d < 0.5 mm was also used and mixed with bentonite to different ratios of COX/MX80 = 100/0; 80/20; 60/40; 40/60; 0/100). The major results of the investigations on this fine-grained claystone-bentonite mixture are presented in / ZHA 13a/14c/d/.

4.2   Compacted density

Drift seals are usally designed to consist of compacted blocks of clay-based mixtures and bentonite pellets filling th remaining gaps between the blocks and the drift wall. The blocks must have sufficiently high densities to ensure the requirements on the other sealing properties. The compressibility of the initially loose materials is essential for determination of necessary compression energy to achieve the desired densities.

Three mixtures were selected for testing:

1. Claystone-bentonite mixture in a ratio of COX/MX80 = 80/20 with grain sizes of d < 5 mm for COX and d < 0.5 mm for MX80 and with water content w = 6.0 %;
2. Claystone-bentonite mixture in a ratio of COX/MX80 = 60/40 with grain sizes of d < 5 mm for COX and d < 0.5 mm for MX80 and with water content w = 7.7 %;
3. Bentonite-sand mixture in a ratio of MX80/Sand = 70/30 with grain sizes of d < 0.5 mm for MX80 and d < 2 mm for Sand and with water content w = 9.1 %.

The mixtures were compacted in oedometer cells of 100 mm diameter and 100 mm height up to a miaximum axial load of 30 MPa. Fig. 4.2 shows the compaction curves and pictures of the compacted samples. It was observed that:

a. the initial dry densities of both claystone-bentonite samples before loading are higher than that of the bentonite-sand mixture due to different distributions of the grain sizes;
b. consequently, the final densities of the claystone-bentonite samples at 30 MPa are quite high: dry density ρ_d = 1.90 and 1.88 g/cm^3 for COX/MX80 = 80/20 and 60/40 respectively; and ρ_d = 1.70 g/cm^3 for MX80/Sand = 70/30;
c. the coarse grains of claystone and sand are relatively homogeneously distributed in the compacted blocks.

The dry density of 1.7 g/cm^3 achieved for the bentonite-sand mixture is slightly higher than that of 1.6 g/cm^3 for the same mixture tested in the in situ borehole sealing experiment PGZ /DEL 13/. The dry densities achieved at 30 MPa are defined as reference densities of compacted blocks of the different mixtures.
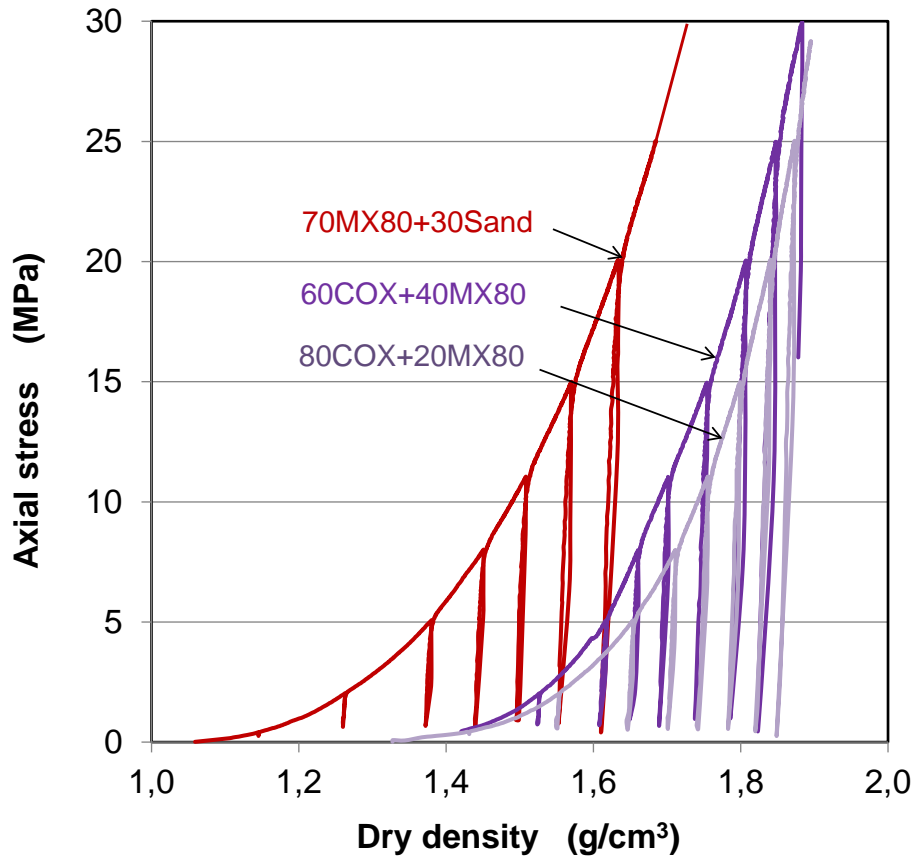
| 80COX+20MX80 | 60COX+40MX80 | 70MX80+30Sand |
| dry density = 1.90 g/cm^3 | dry density = 1.88 g/cm^3 | dry density = 1.70 g/cm^3 |

Fig. 4.2   Compacted dry densities of the claystone-bentonite and bentonite-sand mixtures

4.3   Water retention

An initially unsaturated clay-based material will take up water from humid environment. The amount of water uptake is governed by suction in the material. The relationship between suction and water content or saturation degree is also called water retention curve. The water retention behaviour of the selected mixtures, including pure MX80 bentonite, bentonite-sand mixture, claystone-bentonite mixture and COX claystone, was determined in confined and unconfined conditions under various environmental humidities.

The tests were carried out in three groups consisting of the different samples, as given in Table 4.1. Test group I consisted of the pure MX80 bentonite powder ($d < 0.5$ mm), crushed COX aggregate ($d < 5$ mm), and claystone-bentonite mixture in two ratios: COX/MX80 = 80/20 and 60/40. The materials were compacted in steel cells of 50 mm diameter and 33 mm height up to the maximum load of 30 MPa. Seven samples were prepared for each mixture. Fig. 4.3a shows the photos of the prepared samples.

In test groups II and III, the bentonite-sand (70MX80+30Sand) and claystone-bentonite (60COX+40MX80) mixtures were compacted in steel cells of 50 mm diameter and 20 mm height to the desired densities. The samples were covered with sintered porous discs. The COX claystone cores were prepared to the same size and inserted in the cells. The bentonite powder and the crushed COX claystone were unconfined. Fig. 4.3b shows the photos of the prepared samples in test group III.

All the prepared samples were placed in desiccators at different relative humidity values of $RH = 15$ % to 100 % in group I and $RH = 35$ % to 100 % in groups II and III (Fig. 4.3c). The humidities were adjusted by means of different salt solutions. The temperature was kept at 24 °C. The relative humidity in each desiccator was continuously recorded by transistor psychrometer sensors, while the water content of each sample was measured at time intervals of weeks and months. In group I, the free deformation of the compacted claystone-bentonite mixtures were also recorded.

Table 4.1   Properties of the samples for determination of the water retention curves

Test group I				
Material property	MX80 bentonite	80 COX+ 20 MX80	60 COX+ 40 MX80	Crushed COX claystone
Grain size d_{max} (mm)	0.5	5.0	5.0	5.0
Grain density ρ_s (g/cm^3)	2.78	2.72	2.73	2.70
Dry density ρ_d (g/cm^3)	1.64	1.95	1.88	2.05
Porosity ϕ (%)	41.1	28.2	31.2	24.2
Water content w (%)	9.67	4.50	5.45	3.0

Test group	II		III			
Material property	70MX80+ 30Sand	60COX+ 40MX80	MX80 bentonite	60COX+ 40MX80	COX claystone	Crushed claystone
Grain size d_{max} (mm)	2.0	5.0	2.0	5.0		
Grain density ρ_s (g/cm^3)	2.75	2.73	2.74	2.73	2.70	2.70
Dry density ρ_d (g/cm^3)	1.72	1.81	1.15	1.89	2,28	2.23
Porosity ϕ (%)	37.5	33.5	58.0	30.7	15.5	17.5
Water content w (%)	7.0	5.5	11.0	6.0	5.5	5.5

a.   Samples in test group I

claystone
in cells

compacted
blocks in cells

bentonite
powder

crushed
claystone

b. Samples
in test
group III
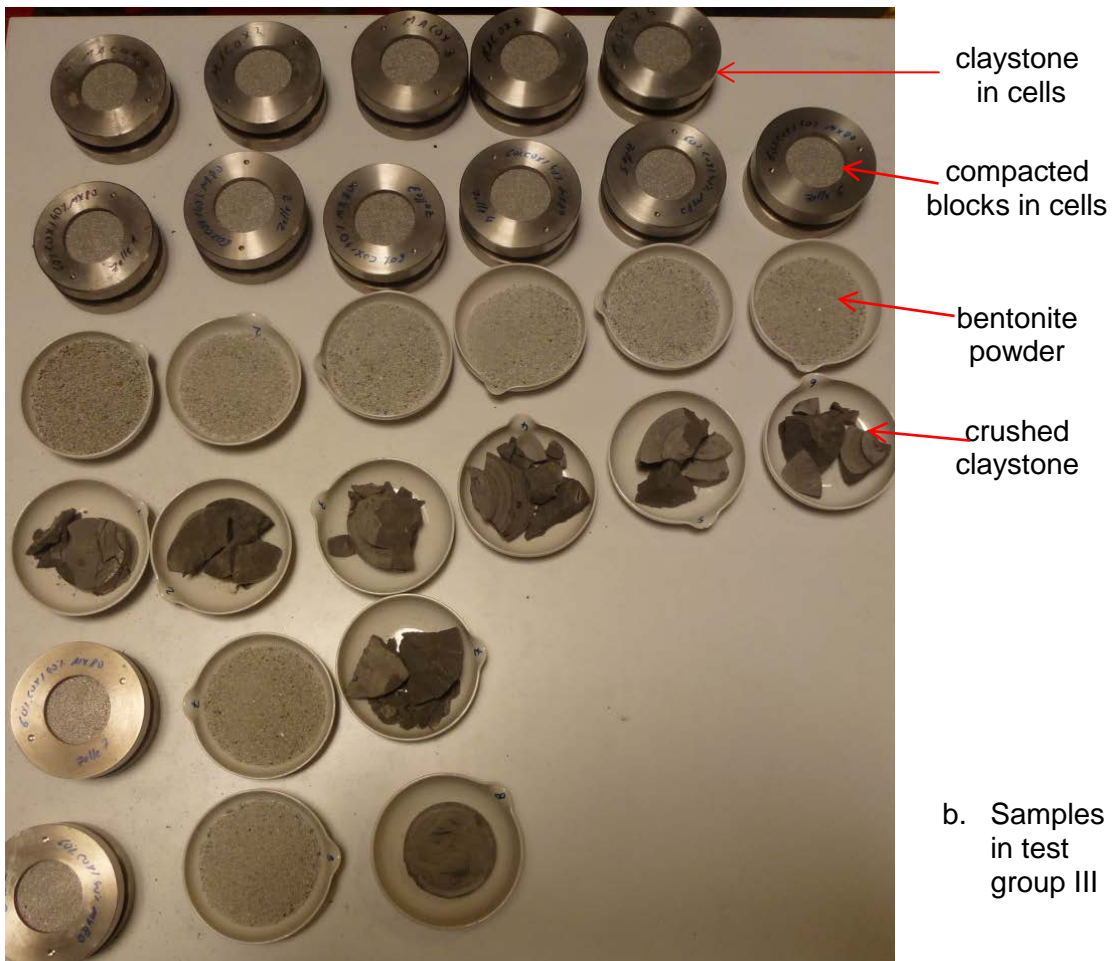
c. Samples in desiccators

Fig. 4.3   Measurement of water retention properties of the seal materials in desiccators at different air humidities

The suction is related to the relative humidity by the psychrometric law /FRE 93/:

$$s = \frac{RT}{v_{wo}\,\omega_v} \ln\left(\frac{p_{va}}{p_{vp}}\right) = -\frac{RT}{v_{wo}\omega_v} \ln(RH) \qquad (4.1)$$

where s = soil suction (kPa), T = absolute temperature (K), R = universal gas constant (8.31432 J/mol K), v_{wo} = specific volume of water or the inverse of density of water ($1/\rho_w$, m³/kg), ρ_w = density of water (998 kg/m³ at 20 °C), ω_v = molecular mass of water vapour (18.016 kg/kmol), p_v = partial pressure of pore-water vapour (kPa), p_{vo} = saturation pressure of water vapour over a flat surface of pure water at the same temperature (kPa), RH = relative humidity ($p_v / p_{vo} \cdot 100\,\%$).

The water contents reached in equilibrium at each humid condition are plotted as a function of suction s in Fig. 4.4 for each material. It can be found out that

- The water content of each material increases gradually with decreasing suction close to zero and then rises rapidly to the maximum w_m at zero suction in vapour: w_m = 45-48 % for the pure bentonite; w_m = 32 % for the 70MX80+30Sand mixture; w_m = 20 % and w_m = 28 % for the 60COX+40MX80 mixture in confined and unconfined conditions respectively; w_m = 19 % for the unconfined 80COX+20MX80 mixture; w_m = 8.8 % for the confined claystone and w_m = 12 % for the unconfined crushed claystone.
- The $w - s$ data obtained on the unconfined pure bentonite with the different initial densities are close to each other (Fig. 4.4a).
- The pure bentonite exhibits the most high water retention capacity. With adding sand and claystone, the amount of water uptake decreases (comparing the pure bentonite in Fig. 4.4a with the bentonite-sand mixture in Fig. 4.4b; and the claystone-bentonite mixture with 40 % and 20 % MX80 component in Fig. 4.4c).
- The water contents measured on the unconfined 60COX+40MX80 mixture (Fig. 4.4c) and the crushed claystone at suctions of higher than 20 MPa are slightly higher than those measured in confined conditions, which might be attributed to different mineral components in the claystone samples.
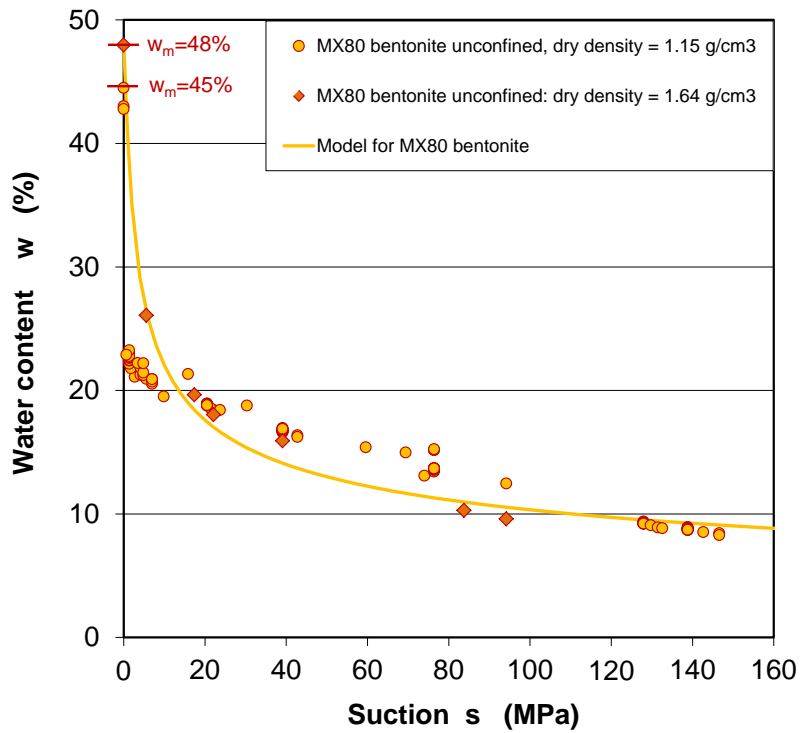
a. Pure bentonite in unconfined condition
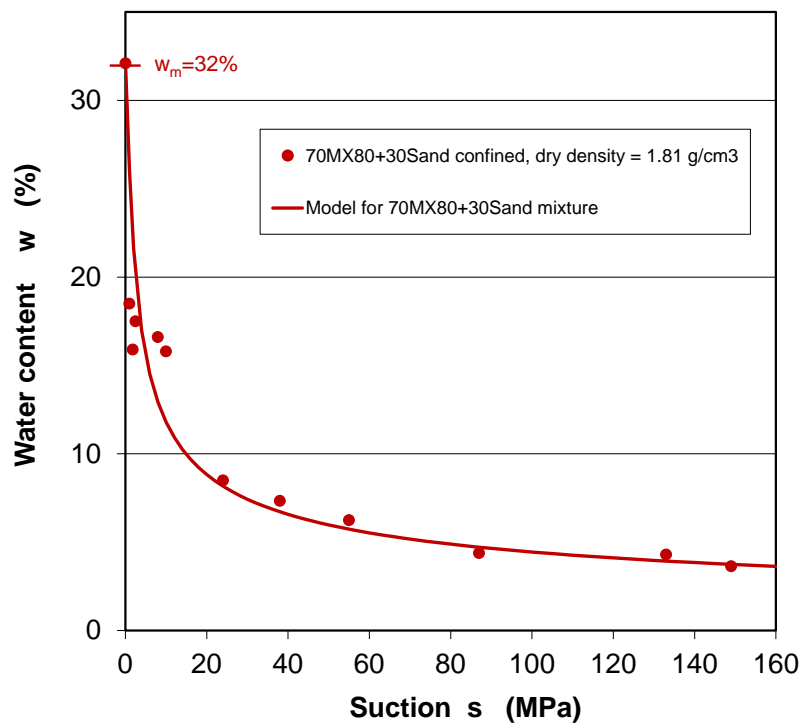
b. Compacted bentonite-sand mixture in confined condition
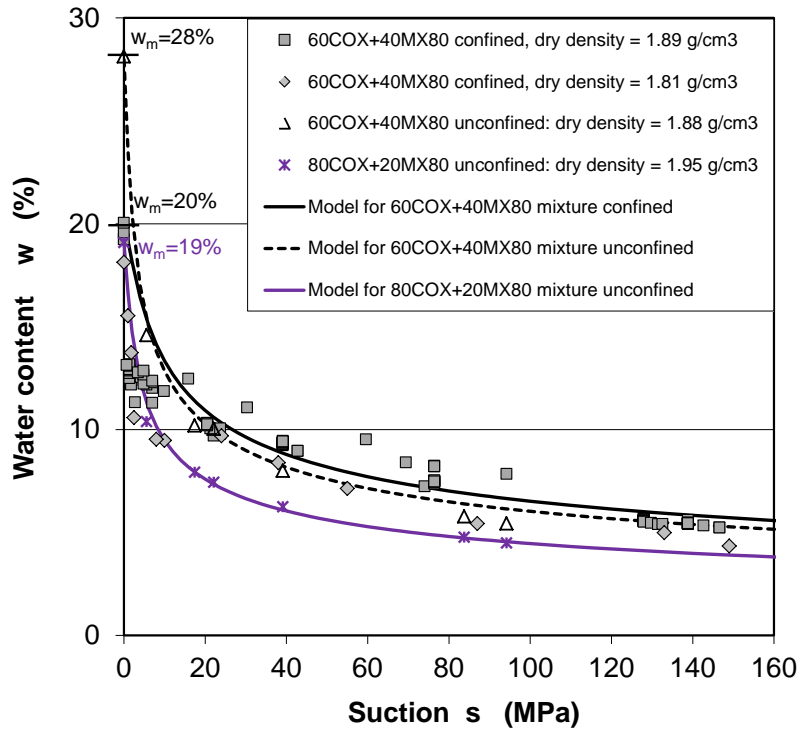
c. Compacted claystone-bentonite mixture in confined and unconfined conditions
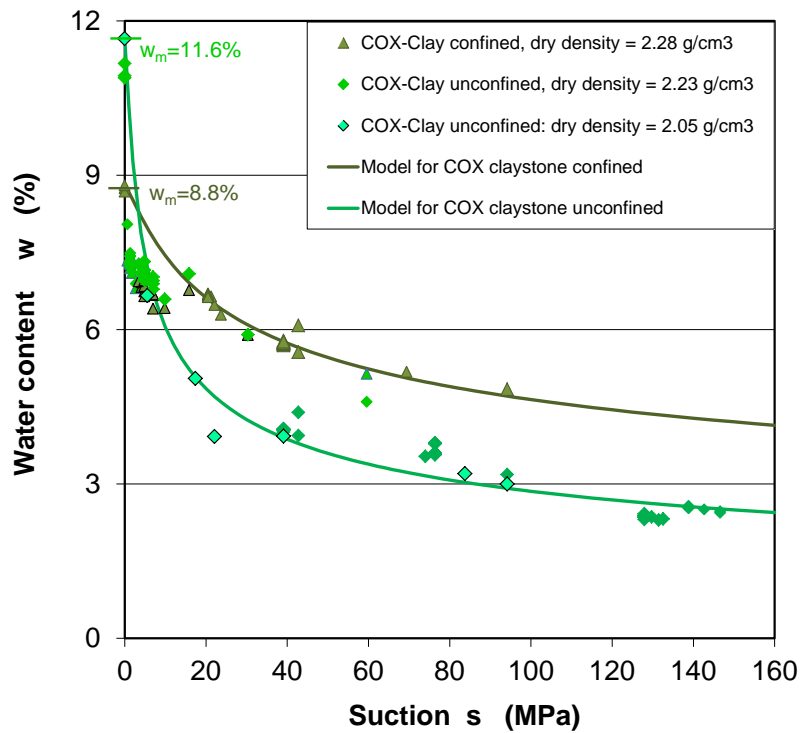
d. Intact claystone in confined and crushed claystone in unconfined conditions

Fig. 4.4   Relationships of water content to suction for the seal materials: bentonite, bentonite-sand mixture, claystone-bentonite mixture, intact and crushed claystone

The relationships between water content and suction are approximated by the van Genuchten model /VAN 80/

$$w = w_m \cdot \left[1 + \left(\frac{s}{P_o} \right)^{\frac{1}{1-\beta}} \right]^{-\beta}$$
(4.2)

where P_o and β are the material parameters. The parameter values are estimated by fitting the $w - s$ data for each material as summarized in Table 4.2. The model is compared in Fig. 4.4a-d with the measured data for each material. A reasonable agreement between the model and data can be identified.

Table 4.2   Parameters of the water retention curves in expression of water content

Parameter	MX80 bentonite unconfined	70MX80+ 30Sand confined	80COX+ 20MX80 unconfined	60COX+ 40MX80 unconfined	60COX+ 40MX80 confined	COX claystone	Crushed claystone
w_m (%)	48.0	32.0	19.0	28.0	20.0	8.8	11.6
P_o (MPa)	1.0	1.0	1.3	1.0	3.5	8.0	1.5
β (-)	0.25	0.3	0.25	0.25	0.25	0.2	0.25

4.4   Water saturation

For evaluation of the hydration or water saturation process in a seal system, water uptake experiments were performed on the selected mixtures: pure bentonite, bentonite-sand mixture, claystone-bentonite mixture, intact claystone and crushed claystone. The materials were compacted to the desired densities in steel cylinders of 50 mm diameter and 100 mm length. Synthetic COX clay water was supplied to an end face of each sample using a burette at atmospheric pressure. The opposite face was connected to the atmosphere via a porous plate. Amounts of water uptake were recorded with time over 10 to 20 months. Fig. 4.5 shows the test layout. After testing, the samples were cut into slices of ~10 mm thickness to determine the distribution of water content and density.

Fig. 4.5   Test layout for water saturation of the seal materials in steel cylinders

The cumulative water uptake recorded is plotted in Fig. 4.6 for (a) pure MX80 bentonite and bentonite-sand mixture in a ratio of MX80/Sand = 70/30, (b) claystone-bentonite mixture in ratios of COX/MX80 = 80/20 and 60/40, (c) intact and crushed COX claystone, and (d) comparison between 70MX80+30Sand and 60COX+40MX80 mixtures, respectively. The main results are:

a. The saturation processes in the compacted pure bentonite and bentonite-sand (70/30) mixture at the similar dry densities round 1.8 g/cm^3 are comparable, the amount of water uptake in the dense bentonite and mixture is limited by the small pore space; the water distributions in the compacted bentonite and bentonite-sand mixture were relatively homogeneous along the sample length (except for the water entry part) but a full saturation was not yet reached for the periods of 10 to 20 months as shown by the post-testing.

b. Similarly, the water uptake of the compacted claystone-bentonite mixture increases with decreasing density; all the compacted claystone-bentonite samples with ratios of 80/20 and 60/40 were fully saturated after testing over about 10 months.

c. The water uptake of the intact claystone is much slower than that of the compacted backfill due to the limitation of the pore space; while the intact claystone was less saturated because of the much higher density, the compacted backfill was fully saturated over 7 months.

d. The saturation process of the compacted claystone-bentonite (60/40) mixture is faster than that of the compacted bentonite-sand (70/30) mixture, even though the density of the first mixture is higher than that of the last one.
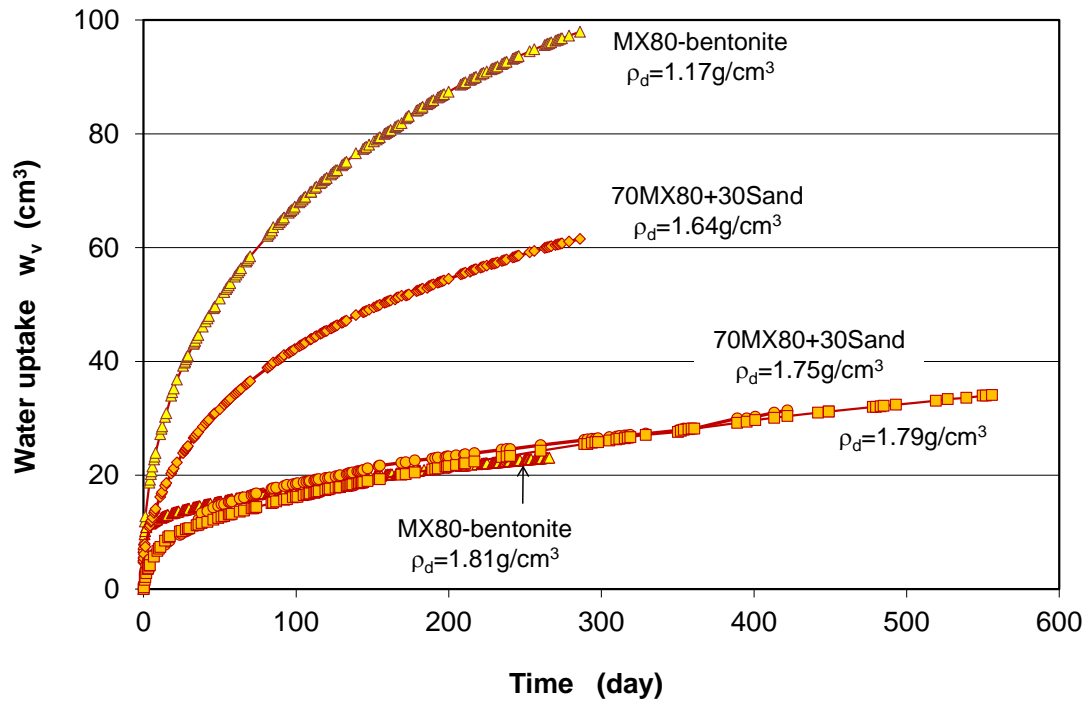
a. Compacted bentonite and bentonite-sand mixture
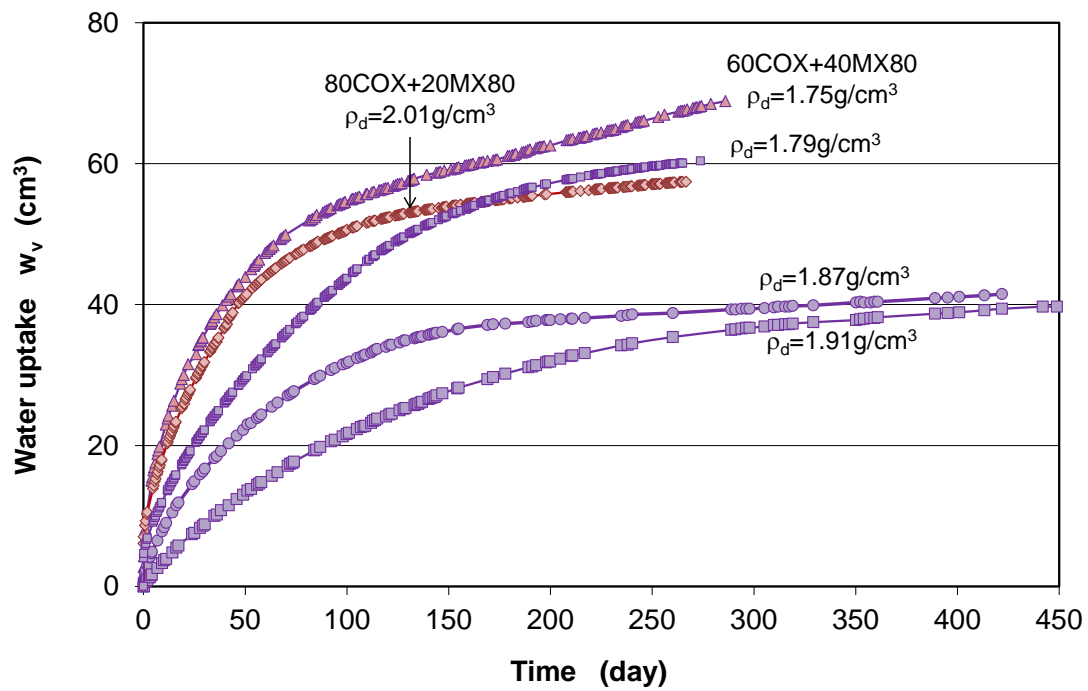
b. Compacted claystone- bentonite mixture
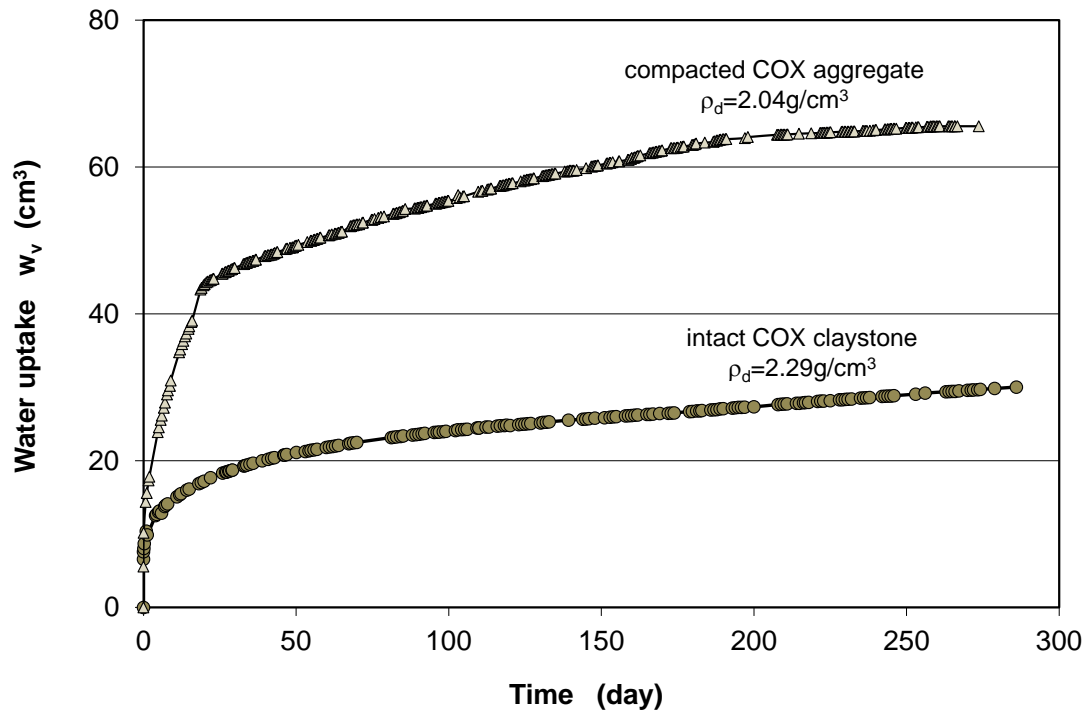
c. Intact and crushed claystone
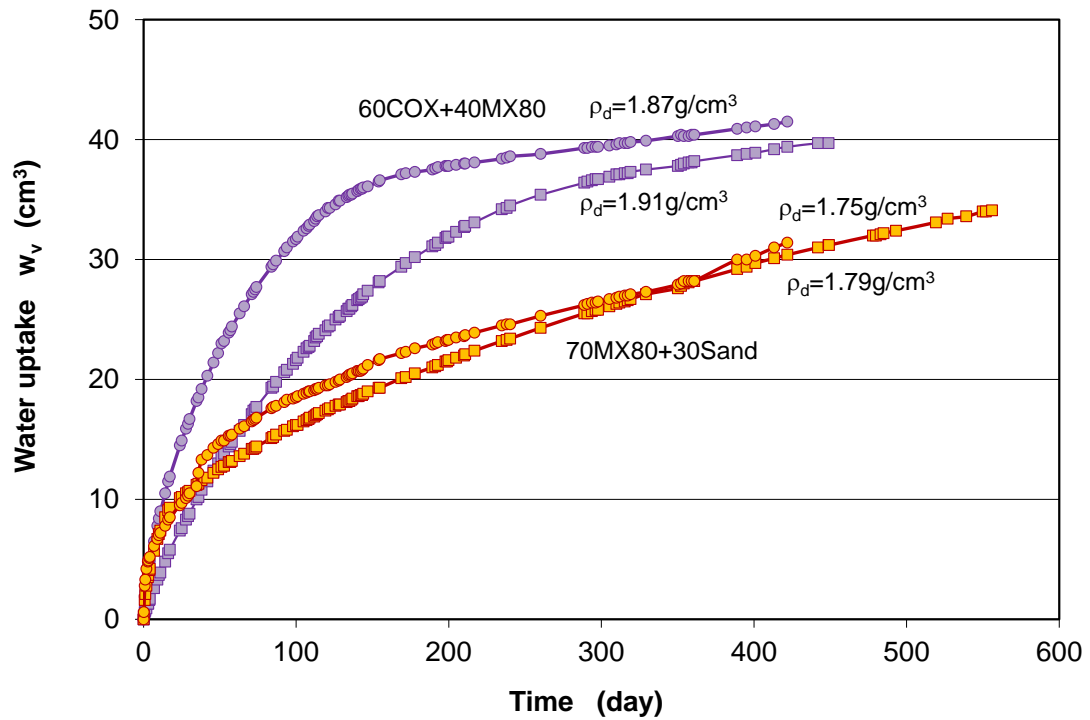
d. Comparison between claystone-bentonite and bentonite-sand mixtures

Fig. 4.6   Evolution of cumulative water uptake of compacted seal materials in contact with synthetic clay water at atmospheric pressure

Due to the high initial suction in the relatively dry state, each sample takes up water rapidly in the beginning and then the saturation process becomes slower. The retardation of water migration is primarily caused by the adsorption of water molecules on clay particles. As a consequence, the suction gradient in the clay-based materials decreases on the one hand; and on the another hand, the adsorbed water films and also the resulting swelling of the clay minerals reduce the accessible pore space for further water migration.

4.5   Swelling capacity

The swelling capacities of the compacted claystone-bentonite and bentonite-sand mixtures were determined by measurements of swelling deformation and pressure under various conditions.

4.5.1   Free swelling

First, the swelling capacities of the selected materials were examined by measurement of swelling deformation of the unconfined samples during the water retention tests (group I) mentioned previously in section 4.3. Four the claystone-bentonite mixture samples with ratios of COX/MX80 = 100/0, 80/20, 60/40 and 0/100 were compacted to different dry densities of 2.05, 1.88, 1.95 and 1.64 g/cm^3, respectively. The main characteristics of the samples (group I) are given in Table 4.1 and Fig. 4.3.

The unconfined samples were placed in desiccators at different relative humidity values of $RH = 15\%$ to 100%, corresponding to suctions between 260 and 0.0 MPa. The water content and the deformation of each sample were measured at different time intervals over more than 6 months until equilibrium. Fig. 4.7 illustrates the measured water contents and the volumetric strains of the compacted mixtures at the different suctions. The water content of each sample increases with decreasing suction or increasing humidity. The moisture uptake at a given suction is proportional to the bentonite content of the mixture. In the wet environment close and equal to zero suction ($RH = 96\text{-}100$ %), all the mixtures can take up large amounts of water up to 12% for the claystone and 48% for the bentonite. The increase in water content is accompanied by volume expansion. At the high humidities of 96-100%, the compacted claystone can expand by a volume increase of 12%, while the other mixtures expand even more up to 20-40%

due to more bentonite content. The volume expansion is almost linearly related with the increased water content, as shown in Fig. 4.8.
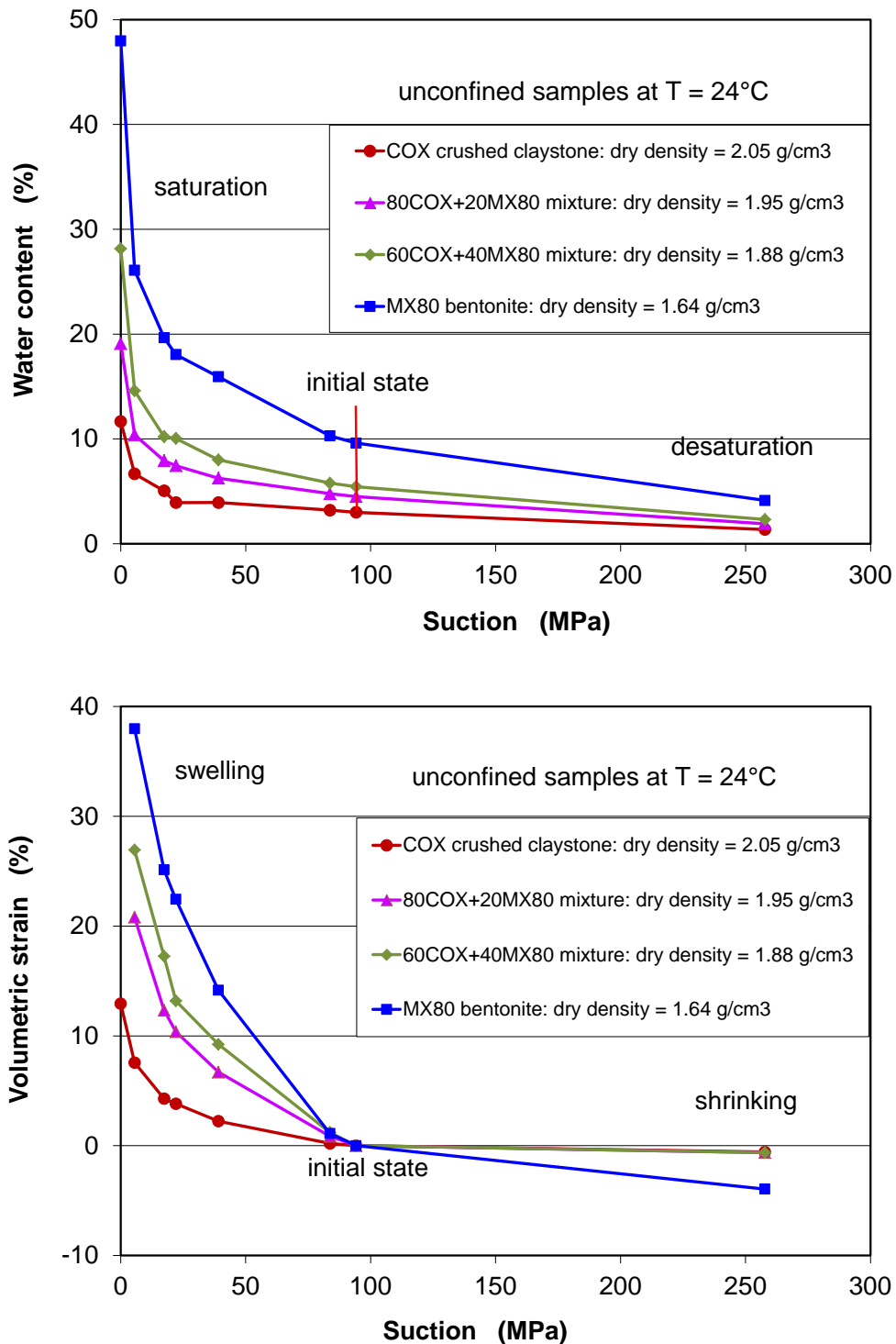
Fig. 4.7   Water uptake (a) and free swelling (b) measured on the compacted clay-stone-bentonite mixtures at different suctions
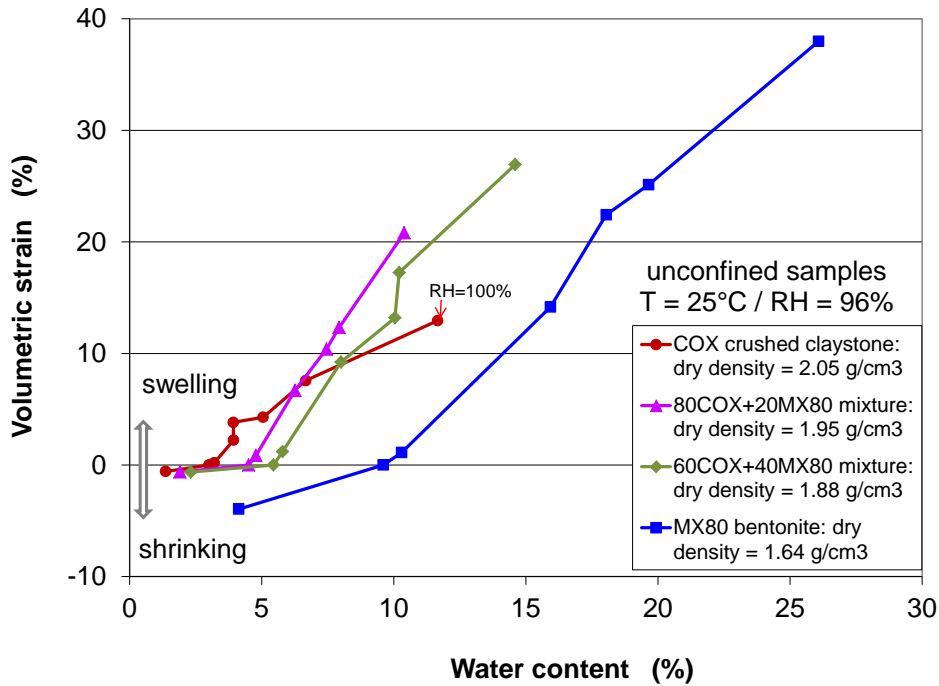
Fig. 4.8   Free swelling of the compacted seal materials with increasing water content

4.5.2   Swelling under load

The compacted seal materials are also able to swell under certain loads. Fig. 4.9 demonstrates the swelling strains of the claystone-bentonite mixture (60COX+40MX80, ρ_d = 1.85 g/cm^3) and bentonite-sand mixture (70MX80+30Sand, ρ_d = 1.75 g/cm^3) in oedometer cells under axial load of 1 MPa during wetting with synthetic COX clay water. The initially fast water uptake leads to a rapid expansion of each mixture in the beginning, and then both the water uptake and the resulting swelling become slow and tend to a final stable state after three months. The maximum swelling strains reached are quite high to 9.5 % at 60COX+40MX80 and 8.5 % at 70MX80+30Sand respectively. As the load is removed, the samples expanded furthermore up to higher levels of 23 % at 60COX+40MX80 and 17 % at 70MX80+30Sand respectively. This maximum volume expansion of the compacted claystone-bentonite mixture after unloading is comparable to the free swelling recorded during wetting with vapour (cf. Fig. 4.8). Additionally, the relatively high swelling stain of the claystone-bentonite mixture compared with the bentonite-sand one might be attributed to its higher compacted density.
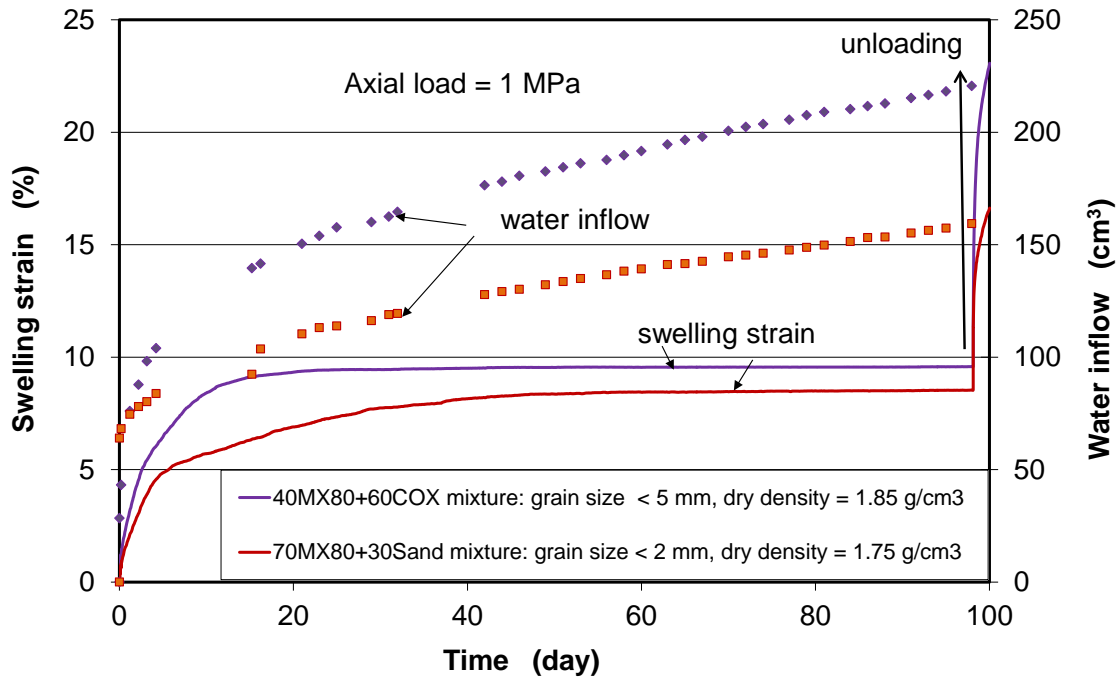
Fig. 4.9   Swelling strains of the compacted claystone-bentonite and bentonite-sand
mixtures under load of 1 MPa during saturation with synthetic clay water

Another swelling test was performed on a compacted 60COX+40MX80 sample (D/L = 50mm/100mm) with a dry density of ρ_d = 1.92 g/cm^3. It was confined in a triaxial cell under hydrostatic stress of 2 MPa. Fig. 4.10 illustrates the test principle and a photo of the sample. It can be seen that the fine-grained bentonite (d < 2 mm) was homoge-nously distributed in the coarse-grained claystone aggregate (d < 5 mm). The synthetic COX clay water was injected into the sample at pressures of p_w = 1.0 and 1.5 MPa over 5 months. Fig. 4.11 shows the response of axial and radial strain to the water injection. At p_w = 1.0 MPa, the sample expanded in the axial direction with time. Since the water flow had not yet reached the middle part where the radial strain was measured, a grad-ual radial compression was recorded within 1.5 months. After that, as the water flow reached this position at p_w = 1.5 MPa, a radial swelling began and increased with time until full saturation after about 3 months. The following measurement of water flow yielded a low water permeability of $6 \cdot 10^{-20}$ m^2. Switching off the water supply, the water pressure decreased gradually with time, but only small strains reversed. The remaining deformation is obviously the result of the swelling effect of the compacted mixture.
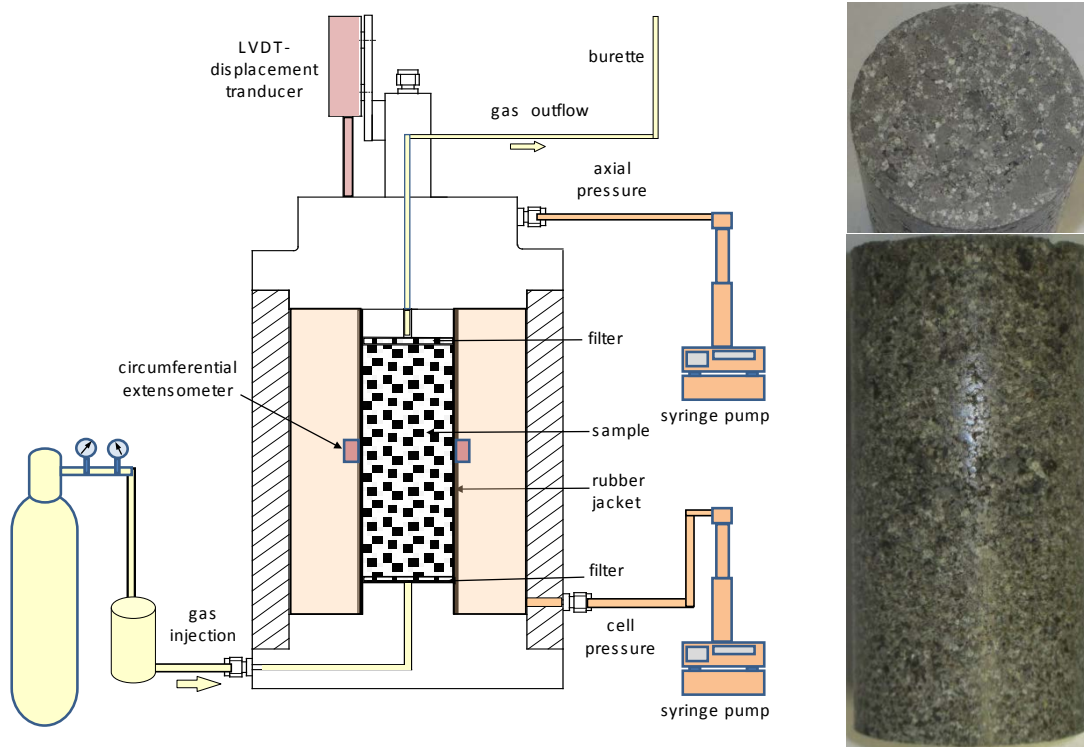
Fig. 4.10   Triaxial swelling test on a claystone-bentonite sample (60COX+40MX80)
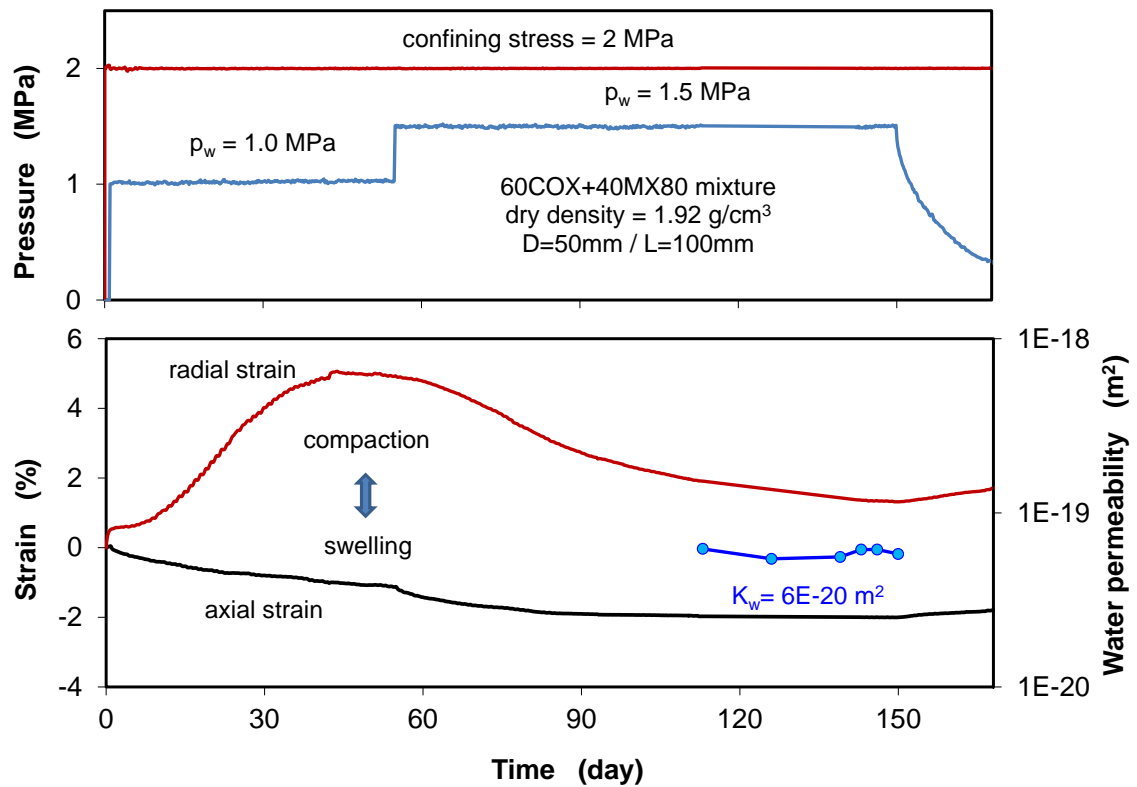
Fig. 4.11   Response of the compacted claystone-bentonite sample to water flow under injection pressures of 1.0 and 1.5 MPa and confining stress of 2 MPa

4.5.3 Swelling pressure

The swelling capacities of the compacted claystone-bentonite (60COX+40MX80, ρ_d = 1.86 g/cm^3) and bentonite-sand (70MX80+30Sand, ρ_d = 1.82 g/cm^3) mixtures were also examined by measurement of swelling pressures in volume-constrained conditions. The mixtures had been compacted in steel cells (D=50 mm, L=30mm) to the desired densities. Fig. 4.12 shows the test setup. The synthetic COX clay water was brought into the samples without applying pressure. Axial swelling pressure was recorded using a pressure sensor installed at the top of the cell between load piston and cap.
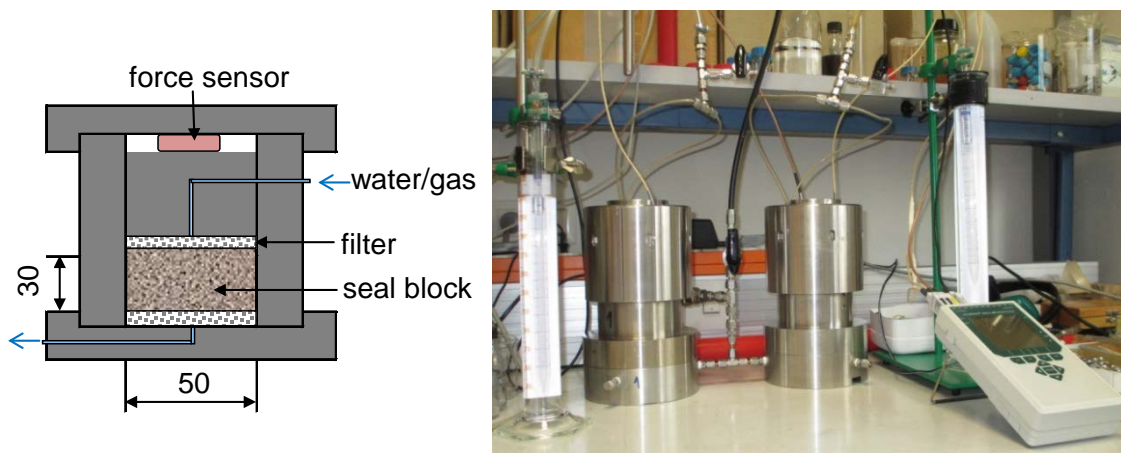
Fig. 4.12   Test setup for swelling pressure measurements on seal samples

Fig. 4.13 depicts the evolution of measured swelling pressures during the saturation process. The rapid water uptake within the first days led to a dramatic increase in the swelling pressure up to the individual peaks at both the samples. Following that, the swelling pressure of 70MX80+30Sand sample decreased slowly for several days and then increased again to stabilisation at 5.6 MPa, while the swelling pressure of 60COX+40MX80 sample increased with some fluctuations to a final value of 3.7 MPa. The claystone-bentonite mixture shows a quite high swelling pressure, even though its expansive bentonite content is low at 40 %. The swelling pressure increases with increasing the bentonite content as shown in the previous tests /ZHA 13a/14c/d/, where large swelling pressures of 6.0 to 9.5 MPa were measured on the compacted claystone-bentonite mixture with high bentonite contents of 40-60 %. Obviously, the higher fraction of the bentonite in its mixture with sand is the reason for the higher swelling pressure.
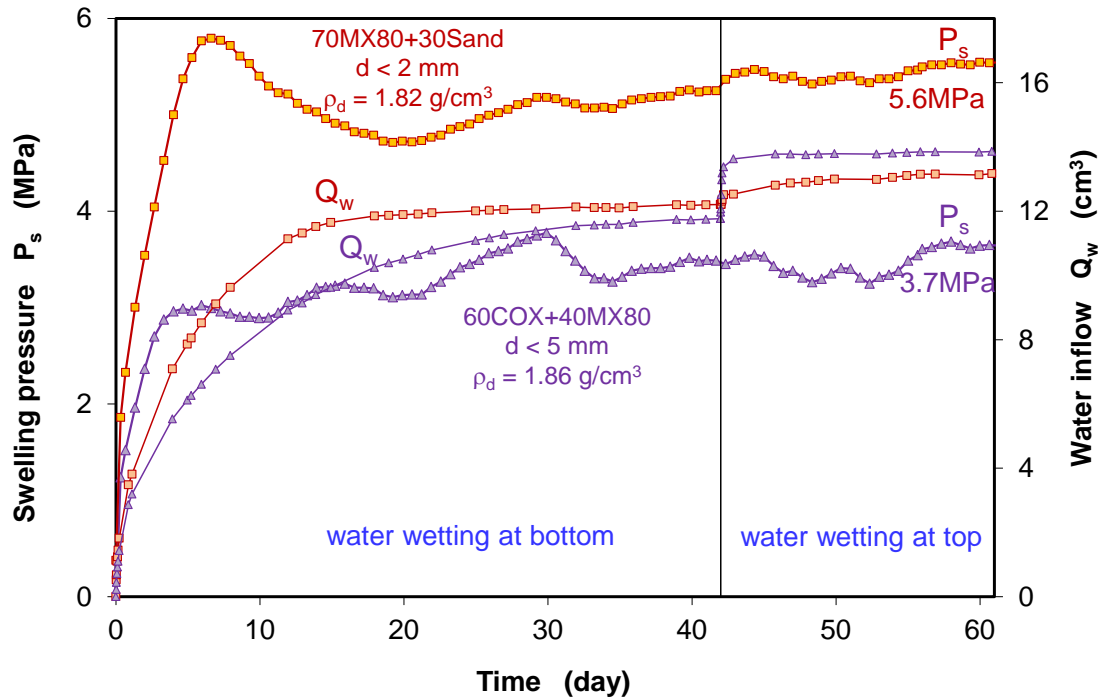
Fig. 4.13   Buildup of swelling pressure in the compacted claystone-bentonite and bentonite-sand mixtures during wetting with synthetic clay water

4.6   Water permeability

The main function of seals in a repository is to prevent fluid access into the repository and the release of radionuclides from it. Therefore, very low hydraulic conductivities of the seals are required from the beginning over long time periods of thousands of years. The water permeabilities of the compacted claystone-bentonite and bentonite-sand mixtures were determined by flowing synthetic clay water through the samples at an injection pressure of 0.5 MPa. Fig. 4.14 presents the measured water permeability values over time. All the compacted mixtures have very low water permeabilities:

- $K_w = 2 \cdot 10^{-19}$–$1 \cdot 10^{-19}$ m^2 for 80COX+20MX80 with grains d < 0.5 and 5 mm and dry densities ρ_d = 1.86–1.90 g/cm^3;

- $Kw = 1 \cdot 10^{-19}$–$3 \cdot 10^{-20}$ m^2 for 60COX+40MX80 with grains d < 0.5 and 5 mm and dry densities ρ_d = 1.86–1.92 g/cm^3;

- $Kw = 2 \cdot 10^{-20}$ m^2 for 70MX80+30Sand with grains d < 2 mm and dry density ρ_d = 1.82 g/cm^3.

In the previous tests ZHA 13a/14c/d/, a very low water permeability of $1 \cdot 10^{-19}$ m^2 was also measured on the crushed claystone with grains < 10 mm and a compacted dry density of 1.90 g/cm^3. All the studied seal materials exhibit the very low water permeabilities close to that of the intact clay rock ($K_w < 10^{-20}$ m^2).
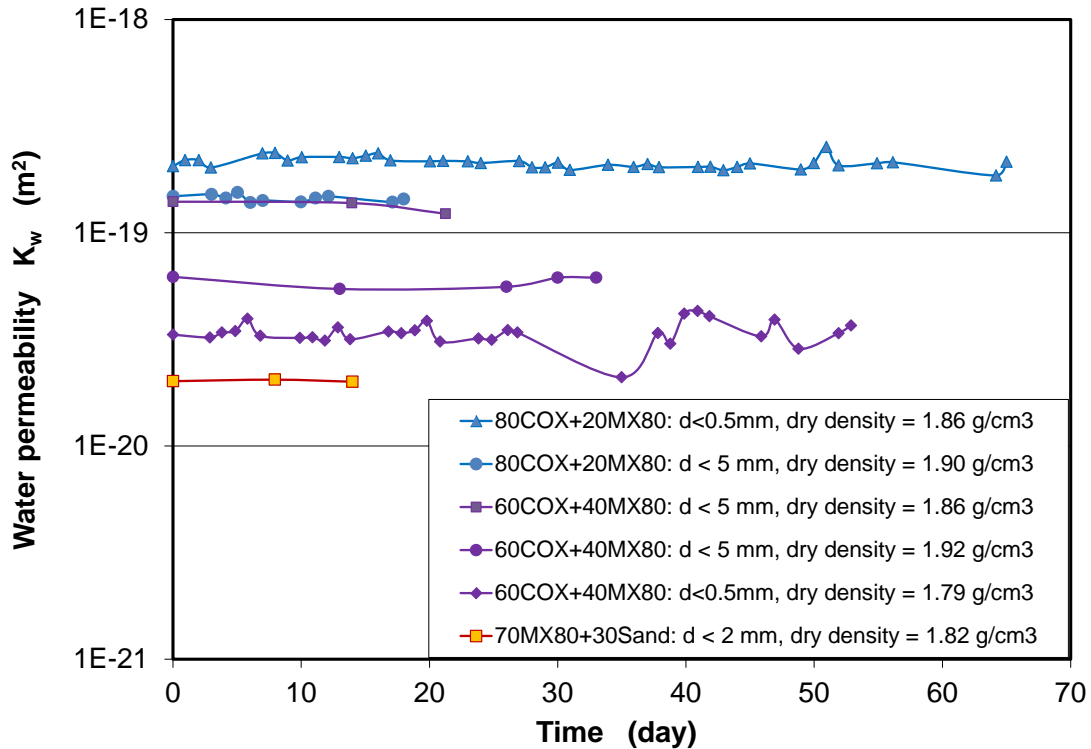
Fig. 4.14   Water permeabilities of the compacted claystone-bentonite and bentonite-sand mixtures

4.7   Gas migration

Gas migration properties of the seal materials were determined by injecting nitrogen gas into the water-saturated samples (D/L = 50mm/30mm) constrained in oedometer cells (see Fig. 4.12) or loaded in triaxial cells. The upstream gas pressure was stepwise increased with small increments of 0.2 to 0.5 MPa at intervals of several days until gas outflow occurred. The corresponding upstream pressure at the gas outflow is defined as the gas breakthrough pressure (P_b) of the sample. After the breakthrough event, the apparent effective gas permeability (K_g) was measured in relation with increased gas pressures. Following that, the inlet was switched off to estimate gas shut-in pressure (P_i) after declination of the upstream pressure with time to a lowest constant.

Three mixtures 70MX80+30Sand, 60COX+40MX80 and 80COX+20MX80 were tested. Their characteristics determined after testing are summarized in Table 4.3.

Table 4.3   Characteristics of the compacted mixtures for gas testing

Material property	70MX80+30Sand	60COX+40MX80	80COX+20MX80
Grain size d_{max} (mm)	2	5	5
Grain density ρ_s (g/cm^3)	2,75	2,73	2,72
Bulk density ρ_b (g/cm^3)	2,08	2,06	2,11
Dry density ρ_d (g/cm^3)	1,82	1,86	1,89
Porosity ϕ (%)	34,1	32,8	30,4
Water content w (%)	20,6	15,5	17,0
Saturation degree S_l (%)	107,8	86,2	103,6
Swelling pressure P_s (MPa)	6,1	3,6	2,7
Gas breakthrough pressure P_b (MPa)	6,1	2,6	1,2
Gas shut-in pressure P_b (MPa)	0,2	-	0,3

Fig. 4.15 shows results of the gas tests on the water-saturated mixtures in oedometer cells. The gas breakthrough pressures identified are P_b = 2.6 MPa for 60COX+40MX80 (Fig. 4.15a) and P_b = 1.2 MPa for 80COX+20MX80 (Fig. 4.15b) respectively. The values are lower than their respective swelling pressures of P_s = 3.7 and 2.7 MPa. In contrast, the event of gas breaking through the bentonite-sand mixture (70MX80+30Sand) occurred at a high pressure P_b = 6.1 MPa equal to the external confining stress (Fig. 4.15a). When the gas injection was stopped, the upstream pressure fell quickly and declined with time to a low value of $P_i \leq$ 0.3 MPa at 80COX+20MX80 (Fig. 3.15b) and $Pi \approx$ 0.2 MPa at 70MX80+30Sand (Fig. 4.15a). The shut-in pressure indicates the shut-off of the interconnected gas pathways and therefore is referred to as the minimum capillary displacement pressure and/or as the minimum internal gas pressure capable of maintaining the network. During the shut-in phase, the previously created gas pathways are going to reseal under effects of clay swelling and compression with reducing the pore pressure. Reopening the pathways again needs sufficiently high gas pressures to overcome the rebuilt capillary thresholds, as indicated by the second breakthrough tests.
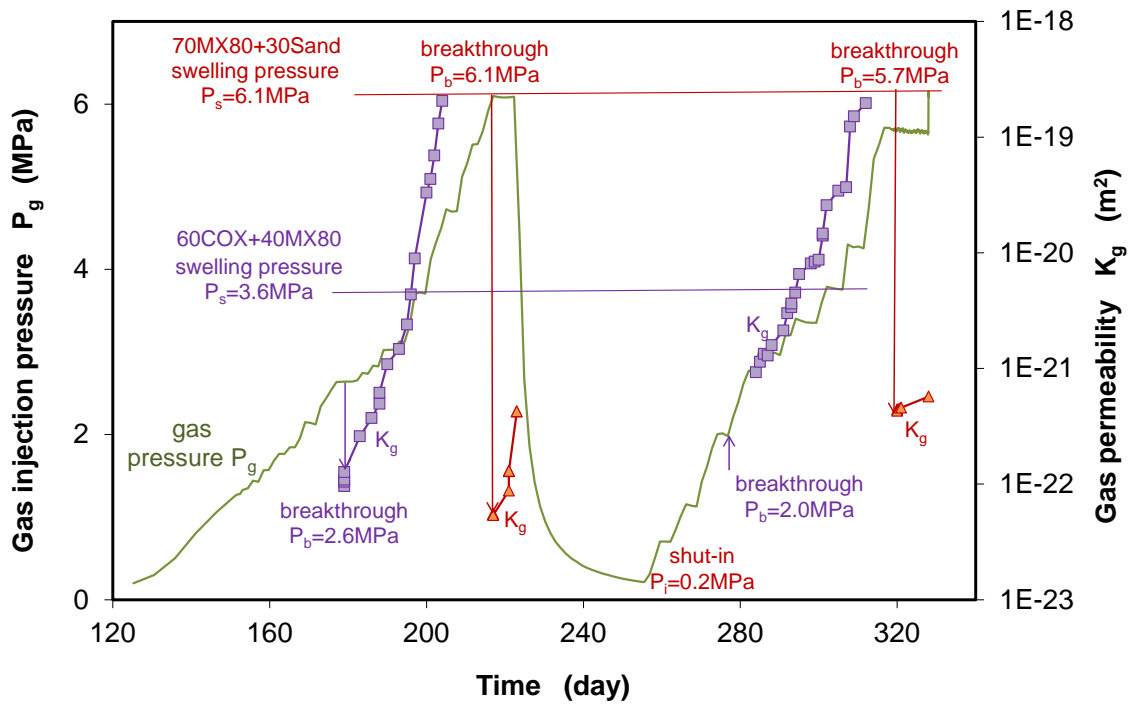
a. 60COX+40MX80 and 70MX80+30Sand mixtures
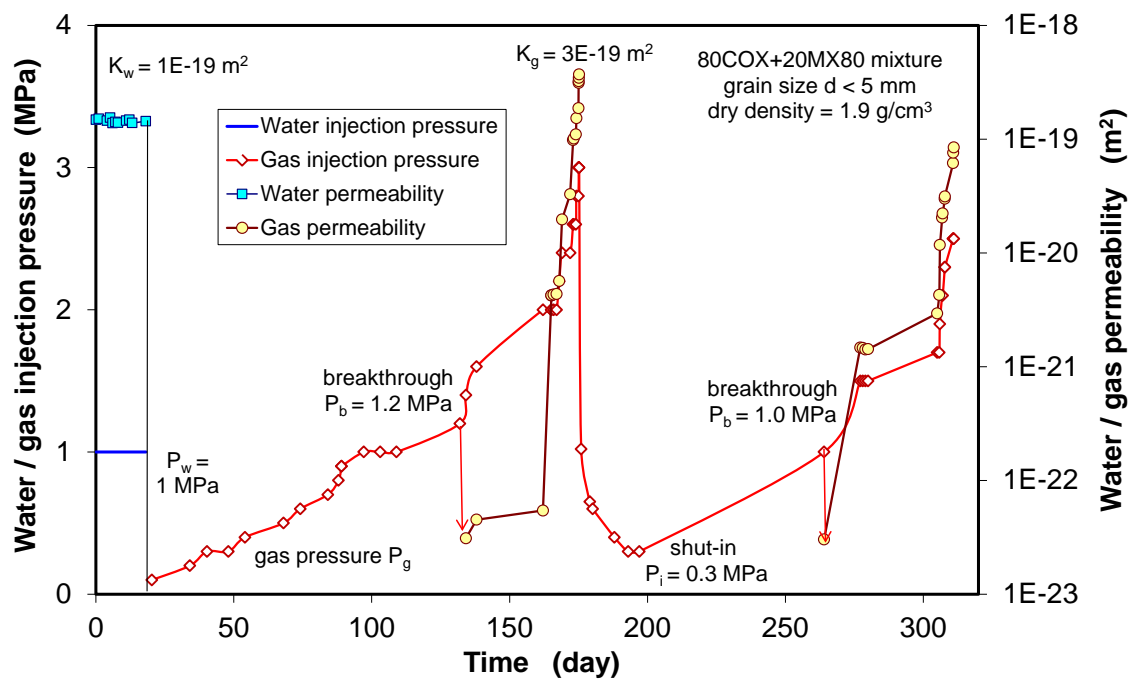
b. 80COX+20MX80 mixture

Fig. 4.15   Gas breakthrough pressures and permeability of the compacted claystone-bentonite and bentonite-sand mixtures

After breakthrough event, the effective gas permeability increases rapidly with increasing gas pressure, as shown in Fig. 4.16 for both the claystone-bentonite samples. At a given gas pressure, the permeability recorded during the second gas flowing phase is relatively higher than during the first phase. Post-testing measurements showed that the 70MX80+30Sand and 80COX+20MX80 samples were fully water-saturated, but another one 60COX+40MX80 not fully saturated. The full saturation calculated means that the gas passed only through a very limited number of thin pathways and no or negligible amount of water was displaced out of the thin channels.
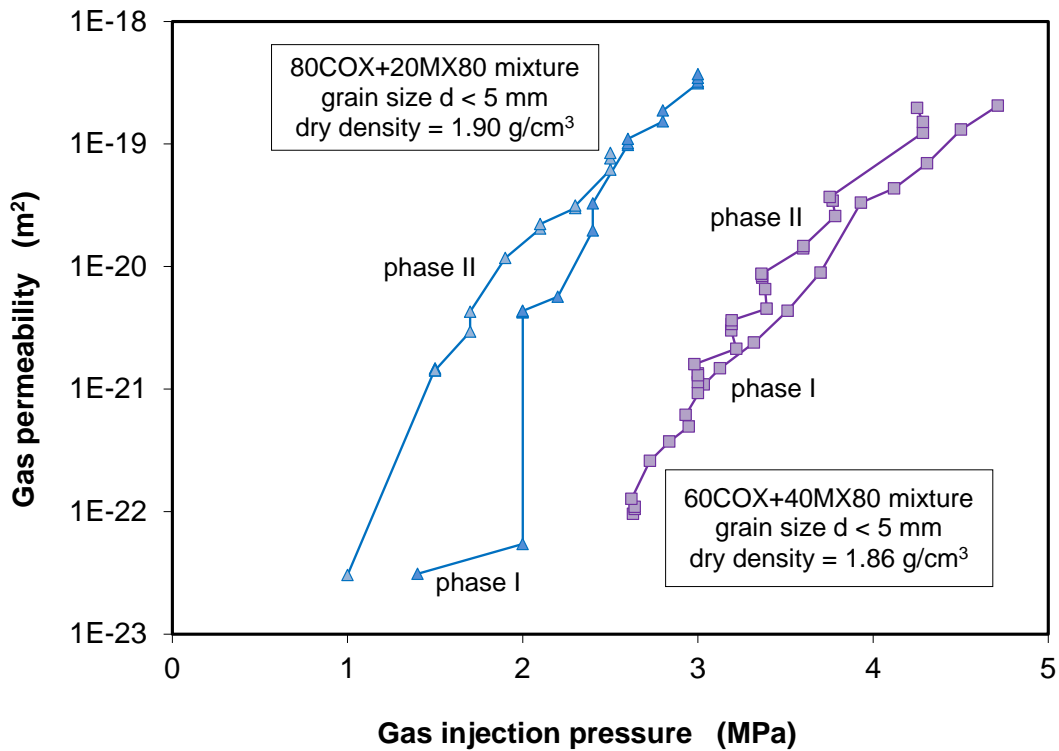
Fig. 4.16   Gas breakthrough permeability as a function of gas pressure

In another series of gas tests, the gas flow properties of three other compacted mixtures were simultaneously examined under hydrostatic confining stresses in a pressure vessel:

1. Claystone (d < 10 mm) with a compacted dry density of 1.93 g/cm^3;
2. MX80 bentonite powder (d < 0.5 mm) with a dry density of 1.76 g/cm^3;
3. Bentonite-sand mixture (MX80/Sand=65/35; d < 2 mm) with a dry density of 1.90 g/cm^3.

The samples were prepared by hand stamping the loose mixtures in rubber jackets of 100 mm diameter and 160 mm length, covered by sintered porous discs, and compacted in an oil pressure vessel up to a confining stress of 12 MPa. Fig. 4.17 illustrates schematically the assembly of the samples and the testing system. Each sample is connected via sintered porous discs to upstream and downstream lines at both end faces. Before gas testing, a water saturation phase had been performed using the synthetic COX clay water for a long duration of 1.5 years. However, only the compacted claystone was fully saturated and a very low water permeability of $K_w = 2 \cdot 10^{-20}$ m^2 was determined. Because no water outflow was detected at the other bentonite-based samples, their saturation state could not be estimated.
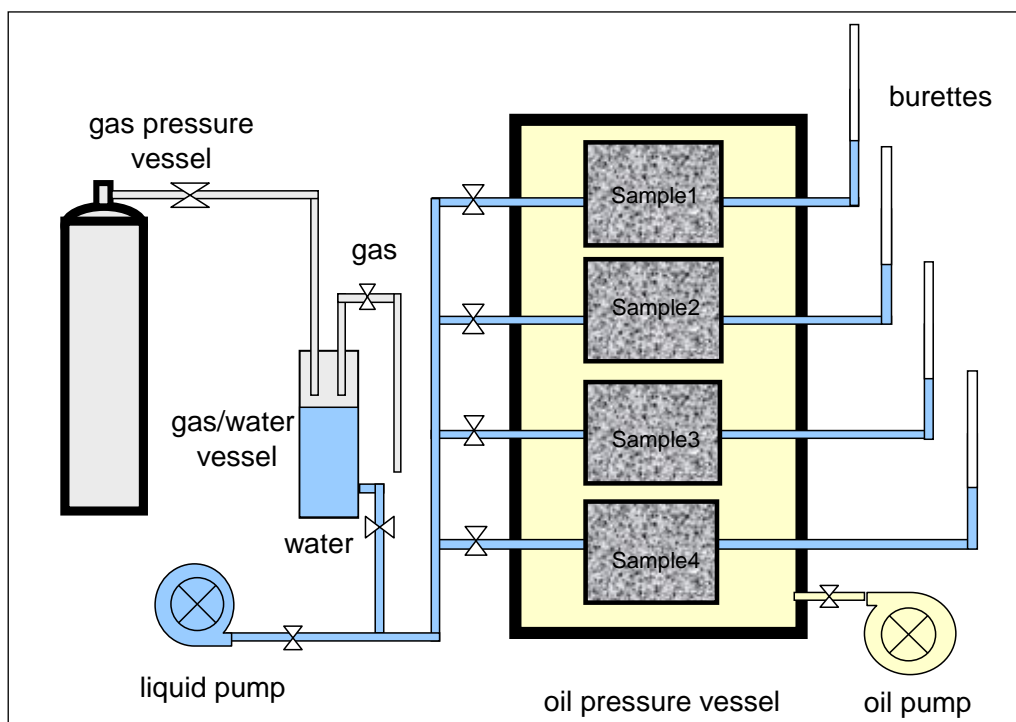
Fig. 4.17   Schematic illustration of the water and gas flow tests with seal mixtures

The following gas injection was performed by stepwise increasing pressure up to the levels of the applied confining stresses of 2 to 8 MPa. Fig. 4.18 depicts the evolution of applied confining stress, gas injection pressure, and gas permeability obtained on the compacted claystone. Whereas the gas breakthrough pressures observed at the compacted claystone are still below the confining stresses, both the compacted bentonite-based samples maintained gas tight at pressures close to each confining stress. This finding made on the compacted bentonite and bentonite-sand mixture is consistent with the common observations /BIR 13/ /SHA 15/, i.e. gas intrusion only occurs when the

pressure of the external gas phase equals or exceeds the confining pressure of the bentonite sample.
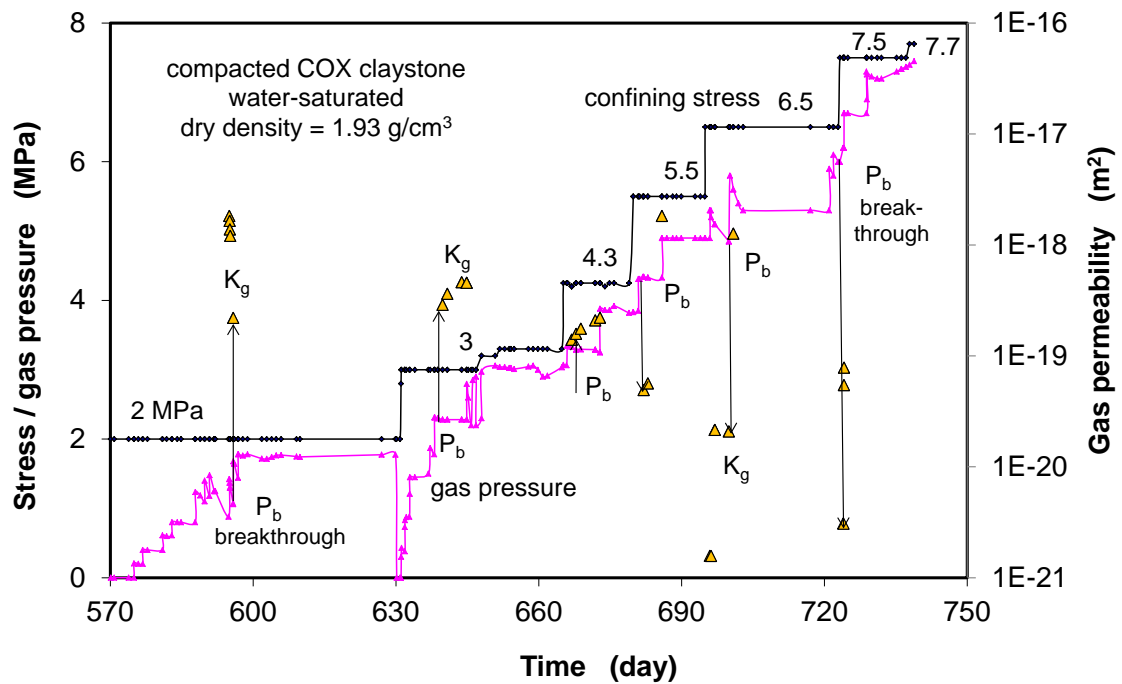
Fig. 4.18   Gas breakthrough pressures and permeabilities obtained on the compacted and water-saturated claystone aggregate at different confining stresses
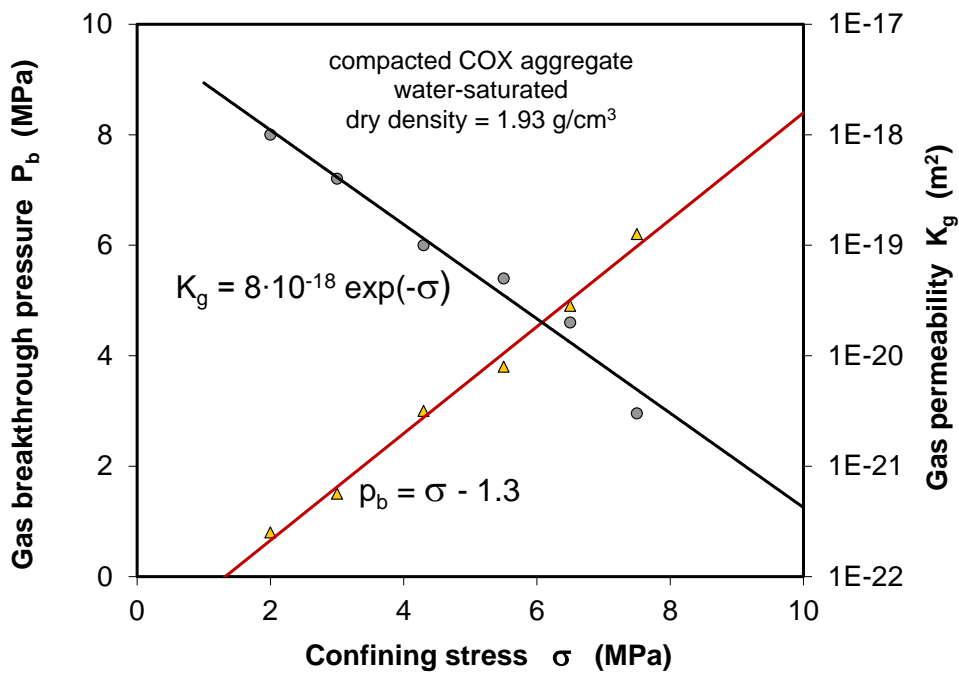
Fig. 4.19   Gas breakthrough pressure and permeability as function of confining stress

For the compacted claystone, the gas breakthrough pressures recorded are directly related to the confining stress. Fig. 4.19 illustrates the relationships of gas breakthrough pressure and permeability with confining stress for the compacted claystone backfill. Whereas the gas breakthrough pressure increase linearly with confining stress, the gas permeability decreases exponentially. The fitting curves can be presented by

$$P_b = a\sigma - b \tag{4.3}$$

where the factor $a = 1$ is estimated and the parameter $b = 1.3$ MPa determined is a stress threshold, at which the gas entry pressure is zero.

The relationship of gas permeability to the confining stress can be expressed by

$$K_g = K_o exp(-\sigma) \tag{4.4}$$

where the factor $K_o = 8 \cdot 10^{-18}$ m^2 determined is the gas permeability at zero confining stress ($\sigma = 0$).

An additional gas test was carried out on the 60COX+80MX80 sample with a dry density of 1.91 g/cm^3 at confining stress of 2 MPa. The sample (D/L = 50mm/100mm) had been fully saturated during the measurement of water permeability (Fig. 4.11). Fig. 4.20 shows that the gas pressure was stepwise increased from 0.3 to 1.8 MPa, during which no clear breakthrough event could be observed. Switching off the inlet, however, the gas pressure declined gradually with time down to 1.3 MPa at 6 months. It implies that the sample was not gas tight at pressures of higher than 1.3 MPa.
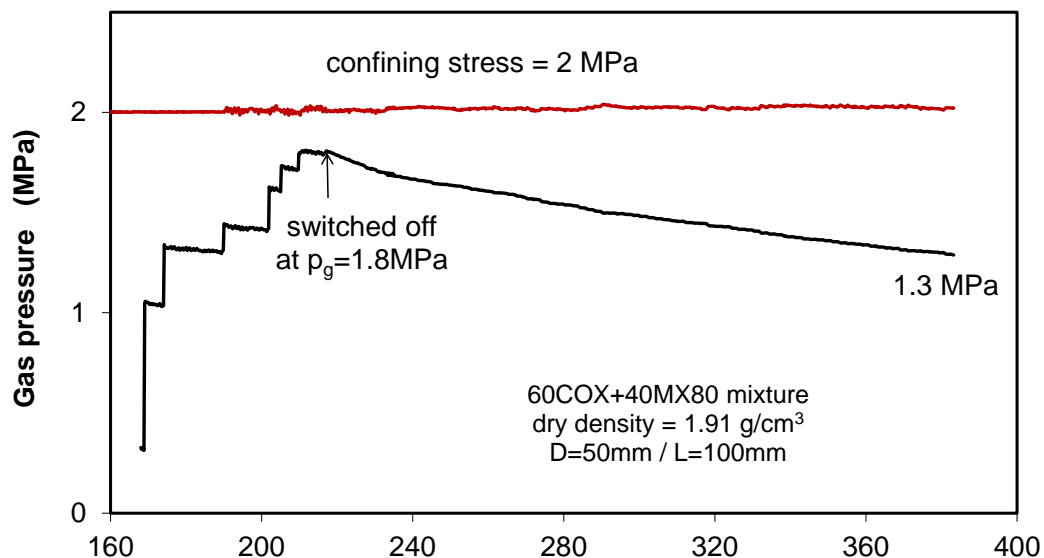
Fig. 4.20   Evolution of gas injection pressure after switching off the inlet to the water-saturated claystone-bentonite mixture

4.8   Borehole sealing tests

As a technical concept (chapter 2), the seals in drift are constructed with compacted blocks of clay-based mixtures between concrete plugs. Gaps between blocks and drift walls are filled with bentonite pellets.

In order to examine the sealing performance of the seal core in the seal/plug system, a small-scale borehole sealing test was designed and started in 2014. A central borehole of 100 mm diameter was drilled in a large claystone cylinder of 280 mm diameter and 200 mm length. The borehole was sealed with the compacted semi-circular blocks of the claystone-bentonite mixture (60COX+40MX80) and with MX80-bentonite powder (d < 0.5 mm) filling the gap of ~2.5 mm width between the borehole wall and the blocks. Unfortunately, shortly after test starting, a fail of the electric power supply caused the failure of the test. Because no large claystone cores were available, the envisaged borehole sealing test could not be performed within this project.

Instead of that, two small-scale borehole sealing tests were conducted on the compacted claystone-bentonite (60COX+40MX80) and bentonite-sand (70MX80+30Sand) mixtures in steel cylinders. The mixtures were compacted to cylindrical blocks of 95 mm diameter and 50 mm height with the desired densities:

- 60COX+40MX80 blocks: mixed with crushed claystone of d < 5 mm and MX80 bentonite powder of d < 0.5 mm with a ratio of COX/MX80 = 60/40, an average dry density of 1.88 g/cm^3 and water content of 7.0 %;
- 70MX80+30Sand blocks: mixed with MX80 bentonite of d < 0.5 mm and quartz sand of d < 2 mm with a ratio of MX80/Sand = 70/30, an average dry density of 1.82 g/cm^3 and water content of 10.7 %.

Fig. 4.18 shows photos of the 60COX+40MX80 and 70MX80+30Sand blocks and the assembled seals. The cylindrical blocks were cut along the length cross the central axis into semi-circular blocks and then installed in two layers into steel cylinders of 100 mm diameter and 100 mm length. The gap of 2.5 mm width between the steel wall and the blocks was filled with the bentonite powder and stamped by hand lightly to a dry density of ~1.20 g/cm^3. Both ends of each sample were covered with sintered porous discs allowing water and gas flow. Development of swelling pressure with water saturation

was recorded by a pressure sensor at the top of the cell between piston and cap. The assembly of the seals and the testing equipment is depicted in Fig. 4.19.

| compacted blocks | cut into two semi-circular blocks |

| first layer | pressed together | filling gaps |
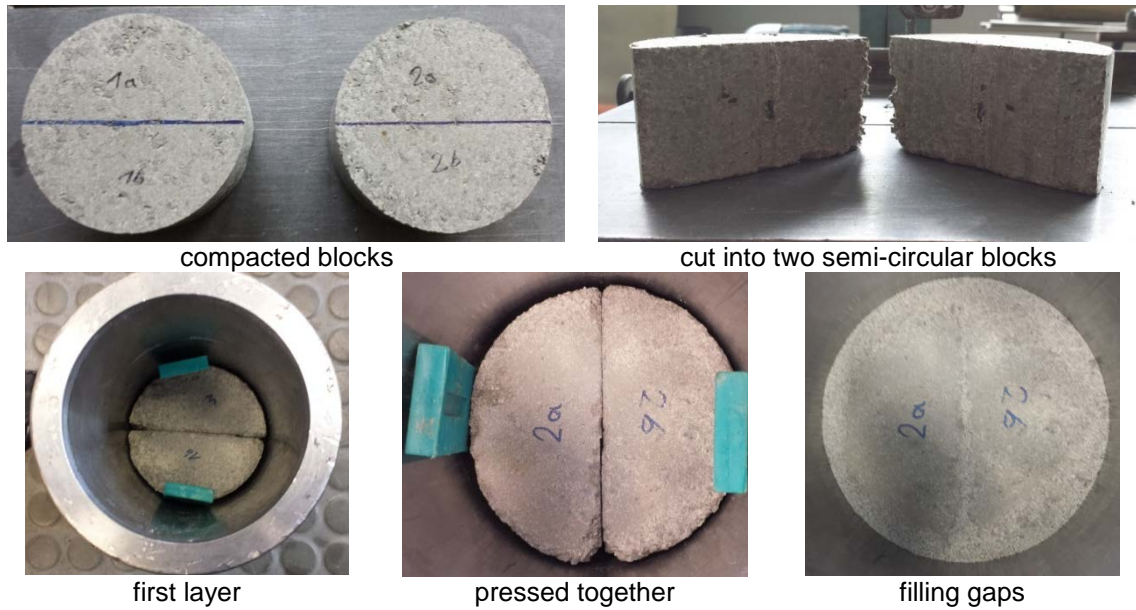
a. Installation of 60COX+40MX80 semi-circular blocks in a steel cylinder

| compacted blocks | cut to two semi-circular blocks |

| first layer | pressed together | filling gaps |
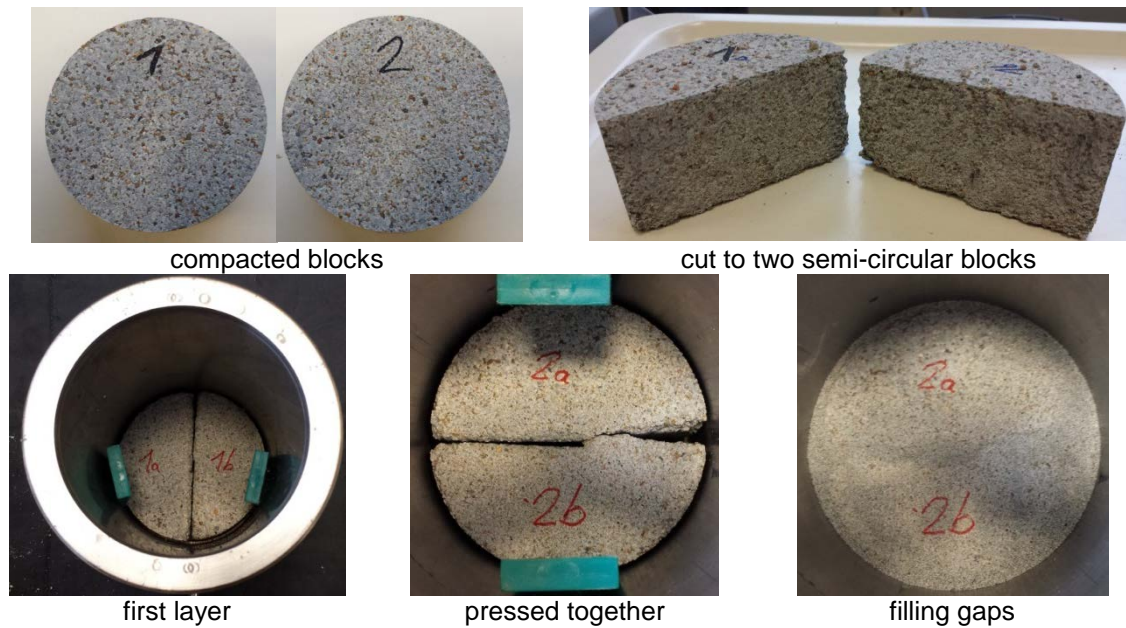
b. Installation of 70MX80+30Sand semi-circular blocks in a steel cylinder

Fig. 4.18   Installation of small-scale borehole sealing tests in steel cylinders with compacted blocks of the claystone-bentonite and bentonite-sand mixtures and bentonite powder filling the gaps
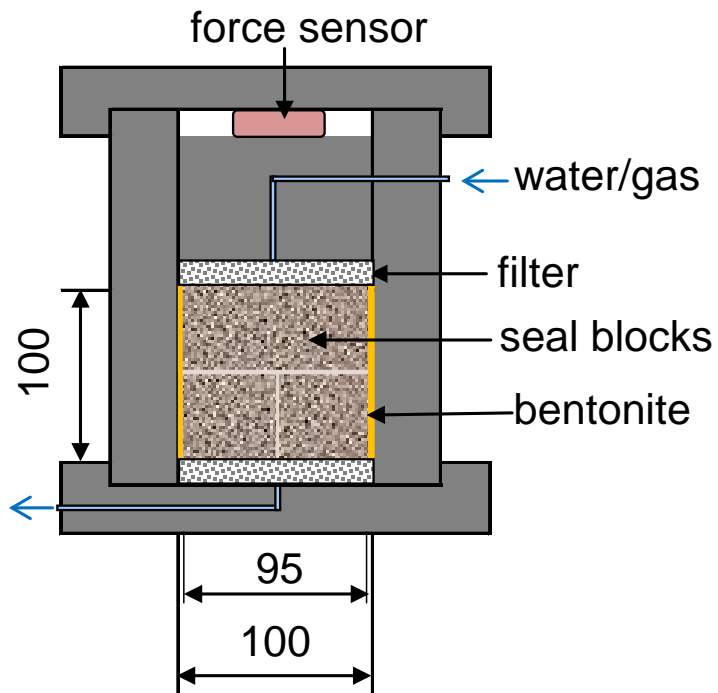
Fig. 4.19   Setup of the small-scale borehole sealing tests in steel cylinders with compacted blocks of claystone-bentonite and bentonite-sand mixtures

The realistic hydraulic conditions to be expected in the drift plug/seal systems were simulated for both parallel seal samples in the following sequence:

1. Water saturation by introduction of synthetic COX clay water to the assembled seals at atmospheric pressure in order to examine the water saturation and the resulting swelling pressure in the seals;
2. Increasing the water pressure up to high levels to simulate possibly high pressure gradients in the drift seals and to determine the hydraulic conductivity of the seals;
3. Gas injection to simulate gas generation and to examine gas migration through the seals.

Fig. 4.20 plots the evolution of water uptake and swelling pressure of the seals during the first water saturation phase over 8 months. Whereas the water uptake increaseed gradually with time, the resulting swelling pressure built up quickly up to 2.1 MPa at the 60COX+40MX80 seal and 2.5 MPa at the 70MX80+30Sand seal within one to two months. After the peak, the swelling pressures declined gradually to a same value of about 2.0 MPa for both the seals. This final value is relatively lower than the swelling pressures measured on the compacted blocks because the density and thus the swelling pressure of the bentonite powder inside the gap is much low.

During the second phase with water injection, the water pressure increased step-by-step up to 1.5 MPa forcing the water inflow over a year. Fig. 4.21 shows the applied water pressure and the amounts of the water injected into both seals. Unfortunately, the pump failed resulting in a large fluctuation of the pressure. After preparation and new starting, the water permeability of each seal was obtained at a constant pressure of 1.3 MPa: $K_w = 1 \cdot 10^{-19}$ m^2 for the claystone-bentonite seal and $K_w = 1 \cdot 10^{-20}$ m^2 for the bentonite-sand seal. These values are comparable to those obtained on the compacted blocks (cf. Fig. 4.14).

The third phase with gas testing is still going on. It will be added to the final report when the test will be finished.
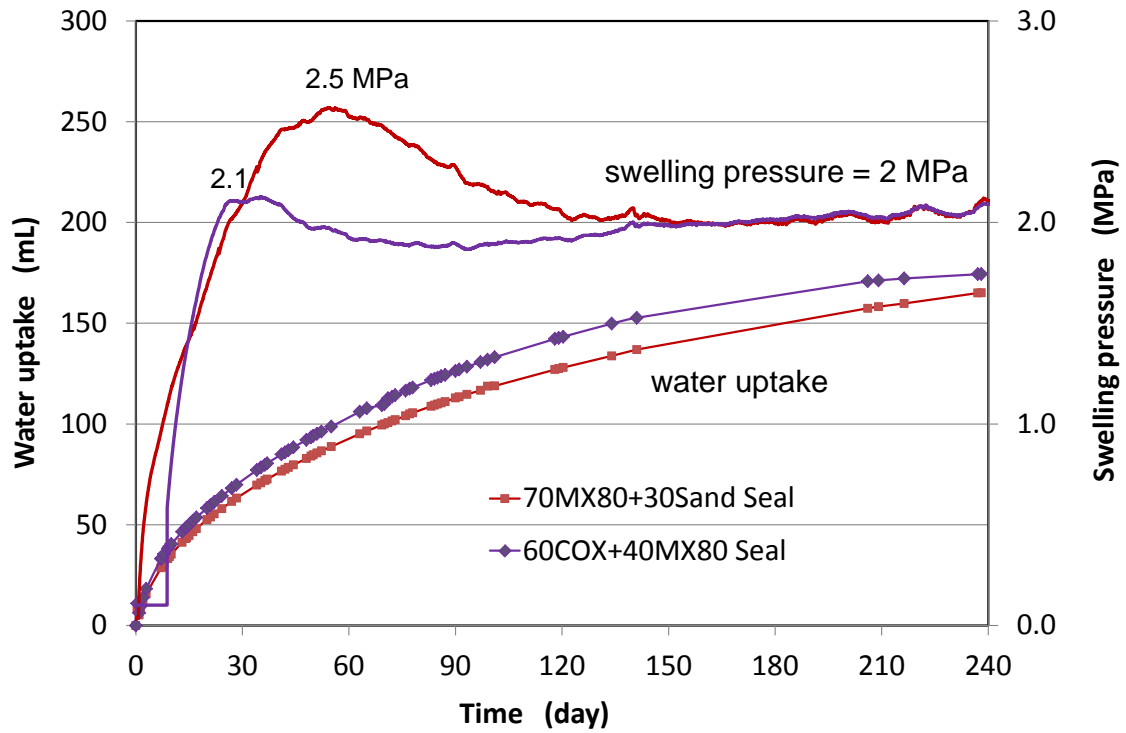
Fig. 4.20   Water uptake and resulting swelling pressure in the claystone-bentonite and bentonite-sand seals
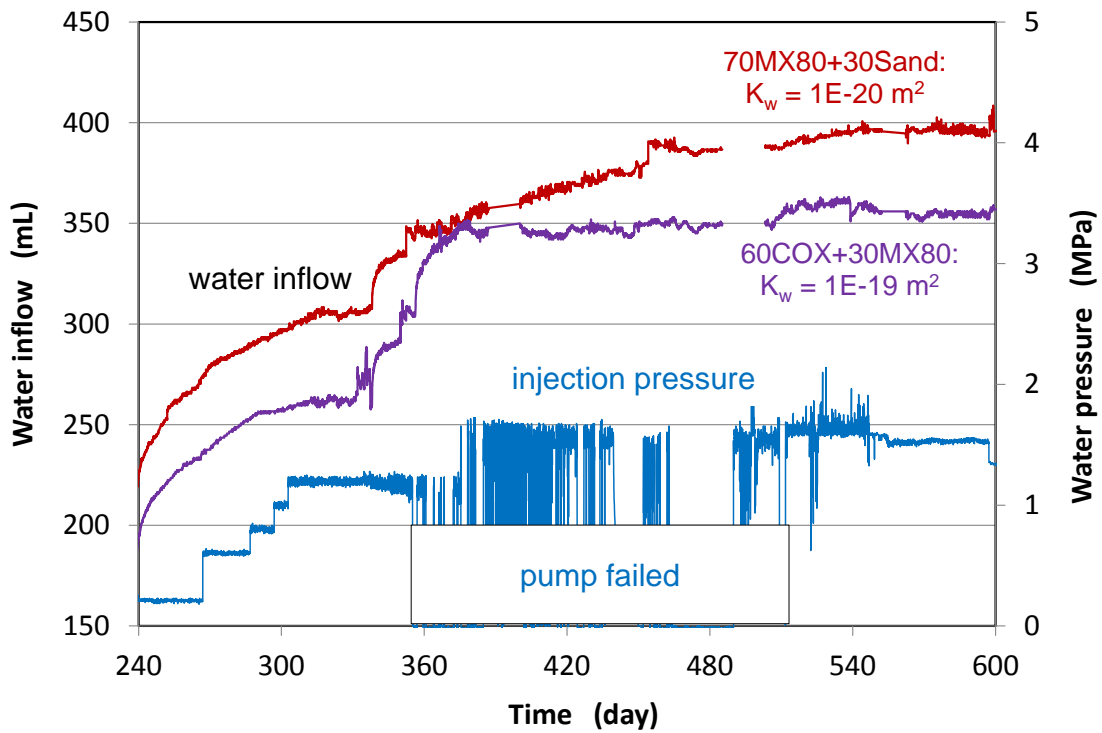
Fig. 4.21   Water inflow into the claystone-bentonite and bentonite-sand seals at increased injection pressures

5 Modelling of seal materials and claystone

For the last decade, GRS has used the FEM code CODE-BRIGHT /UPC 15/ for analysis of coupled thermo-hydro-mechanical (THM) processes in repositories in clay formations. This code was developed by the Technical University of Catalonia in Barcelona. The theories of the THM modelling are presented by the code developer /OLI 94/, /GEN 98/06/ and /UPC 15/. There are a large number of constitutive models implemented in the code for description of the THM behaviours of the geo-materials. For modelling and process analysis of a seal system, one has to identify which constitutive models are adequate for the individual elements of the seal system such as host rock, EDZ, clay-based seal, concrete plug, and others. The associated model parameters for the materials have to be determined from laboratory experiments. In order to enhance the predictive capability for the long-term performance of the seal system, it may be necessary to develop new constitutive equations for some specific aspects, for instance, long-term deformation of clay rock, permeability changes due to damage and reconsolidation, and so on. GRS defined main objectives of the modelling work in task 5.1 of the DOPAS project as follows:

- Identification of constitutive models and parameters for the studied seal materials including the bentonite, bentonite-sand mixture and claystone-bentonite mixture;
- Evaluation and improvement of the existing constitutive models for the clay rock by development of new constitutive equations for the long-term deformation, fracturing-induced permeability, permeability change by compression, water permeability of fractured claystone under load, and gas migration in water-saturated claystone;
- Simulation of typical laboratory experiments for verification of the constitutive models currently available from the code;
- Scoping calculation of the long-term performance of a drift seal.

5.1 Fundamental theories of THM modelling

5.1.1 THM coupling phenomena

Geological and geotechnical porous materials are composed of three species: mineral, water and air; and distributed as three phases: solid (s), liquid (l) and gas (g). The liquid phase contains liquid water and dissolved air, while the gas phase is a mixture of dry air and water vapour. In the porous media simultaneously subjected to thermal, hydrau-

lic and mechanical conditions, complex THM processes and interactions take place as for instance,

- Thermal loading inducing deformation and stress variations (T → M) and expansion of porewater as well as pore pressure changes (T → H);

- Mechanical loading leading to changes in porosity / cracks and hydraulic conductivity (M → H) as well as thermal conductivity (M → T);

- Pore pressure changes being directly related with the effective stress (H → M), and water saturation as well as water/gas flow influencing the heat transfer and the temperature field (H → T).

According to /GEN 06/, the important aspects of THM coupling are illustrated in Fig. 5.1.
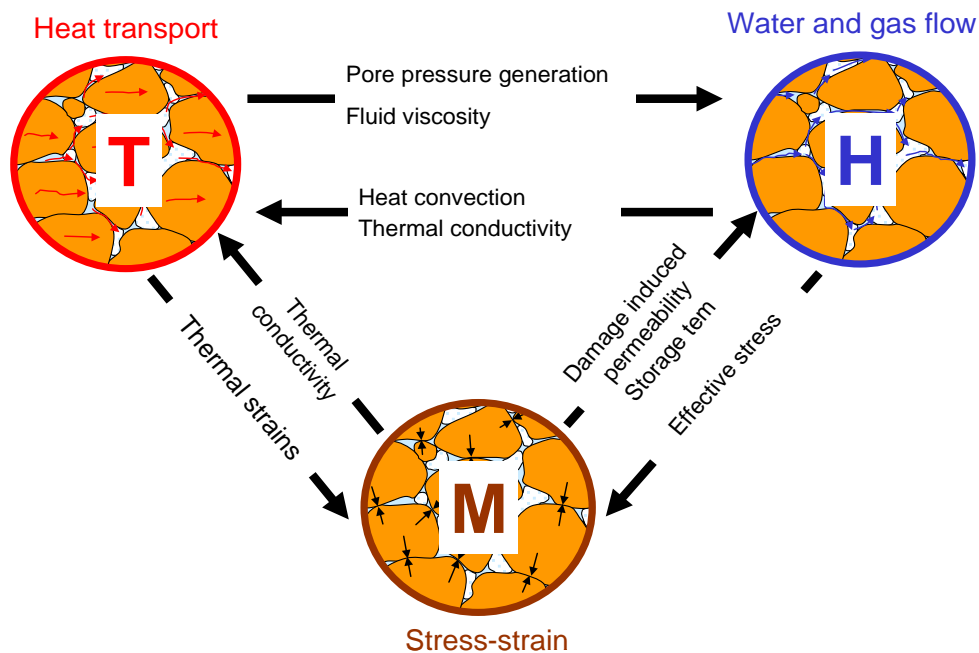
Fig. 5.1   Main relations between THM processes in porous media /GEN 06/

The development of CODE-BRIGHT takes into account the most important coupled THM phenomena /UPC 15/. A number of general assumptions are made in the formulation of the coupled THM problems encountered in unsaturated porous materials:

76

1. Dry air is considered a single species and, usually, it is the main component of the gaseous phase. Henry's law is used to express equilibrium of dissolved air.

2. Vapour concentration is in equilibrium with the liquid phase, and the psychrometric law expresses its concentration.

3. Thermal equilibrium between solid-liquid-gas phases is assumed, i.e. the three phases having the same temperature.

4. Balance of momentum for the medium as a whole is reduced to the equation of stress equilibrium together with a mechanical constitutive model to relate stresses with strains.

5. Small strains and small strain rates are assumed for solid deformation.

6. State variables are solid displacements, liquid pressure, gas pressure, and temperature.

5.1.2 Balance equations

For the calculations of coupled THM processes in the porous media, a set of balance equations for internal energy, solid mass, water mass, air mass, and stress equilibrium are to be solved in a consistent way /UPC 15/.

Energy balance:

Any energy supply is balanced by the total heat flux through the medium and its total internal energy:

$$\frac{\partial}{\partial t}\left(E_s\rho_s(1-\phi) + E_l\rho_l S_l\phi + E_g\rho_g S_g\phi\right) + \nabla \cdot \left(\boldsymbol{j}_c + \boldsymbol{j}_{Es} + \boldsymbol{j}_{El} + \boldsymbol{j}_{Eg}\right) = f^E \quad (5.1)$$

where E_s, E_l and E_g are specific internal energies corresponding to solid, liquid and gas phase, respectively; ρ_s, ρ_l and ρ_g are the densities of the three phases; ϕ is the porosity, S_l is the volumetric liquid fraction and S_g is the volumetric gas fraction with respect to the pore volume, $S_l + S_g = 1$; $\boldsymbol{i}_c$ is the conductive heat flux; $\boldsymbol{j}_{Es}$, $\boldsymbol{j}_{El}$ and $\boldsymbol{j}_{Eg}$ are the advective energy flux of each of the three phases with respect to a fixed reference sys-

tem; f^E is the energy supply per unit volume of medium; t is time and ∇ is the divergence operator.

Solid mass balance:

The mass balance of solid present in the medium is expressed as:

$$\frac{\partial}{\partial t}\left(\rho_s(1-\phi)\right) + \nabla \cdot (\boldsymbol{j_s}) = 0 \tag{5.2}$$

where ρ_s is the density of the solid and $\boldsymbol{j_s}$ is the flux of solid.

Water mass balance:

Water is present in liquid and gas phases. The total mass balance of water is expressed as:

$$\frac{\partial}{\partial t}(\theta_l^w S_l \phi + \theta_g^w S_g \phi) + \nabla \cdot \left(\boldsymbol{j_l^w} + \boldsymbol{j_g^w}\right) = f^w \tag{5.3}$$

where θ_l^w and θ_g^w are the masses of water per unit volume of liquid and gas, respectively; $\boldsymbol{j_l^w}$ and $\boldsymbol{j_g^w}$ denote the total mass fluxes of water in the liquid and gas phases (water vapour), with respect to a fixed reference system. f^w is an external supply of water per unit volume of medium.

Air mass balance:

Dry air is present in liquid and gas phases. The total mass balance of dry air is expressed as:

$$\frac{\partial}{\partial t}(\theta_l^a S_l \phi + \theta_g^a S_g \phi) + \nabla \cdot \left(\boldsymbol{j_l^a} + \boldsymbol{j_g^a}\right) = f^a \tag{5.4}$$

where θ_l^a and θ_g^a are the masses of dry air per unit volume of liquid and gas, respectively; $\boldsymbol{j_l^a}$ and $\boldsymbol{j_g^a}$ denote the total mass fluxes of dry air in the liquid and gas phases, with respect to a fixed reference system; f^a is an external supply of dry air per unit volume of medium.

Stress equilibrium:

The balance of momentum for the porous medium reduces to the equilibrium equation in total stresses:

$$\nabla \cdot \boldsymbol{\sigma} + \boldsymbol{b} = 0 \tag{5.5}$$

where $\boldsymbol{\sigma}$ is the stress tensor and $\boldsymbol{b}$ is the vector of body forces.

Equilibrium restrictions:

Equilibrium restrictions are given for the concentration of water vapour in gas and of dissolved air in water. The mass of water vapour per unit volume of gas $\left(\theta_g^w\right)$ is determined via the psychrometric law:

$$\theta_g^w = \left(\theta_g^w\right)^0 exp\left[\frac{-(P_g - P_l)M_w}{R(273.15+T)\rho_l}\right] \tag{5.6}$$

where P_l and P_g are liquid and gas pressures, respectively, $\left(\theta_g^w\right)^0$ is the vapour density in the gaseous phase in contact with a planar surface (i.e. when $P_g - P_l = 0$), M_w is the molecular mass of water (0.018 kg/mol), R is the gas constant (8.314 J/mol·K) and T is the temperature (in degree Celsius). $\left(\theta_g^w\right)^0$ is depending on temperature. The vapour partial pressure is computed by means of the ideal gas law.

The solubility of air in water is controlled by Henry's law:

$$\omega_l^a = \frac{P_a}{H} \cdot \frac{M_a}{M_w} \tag{5.7}$$

where ω_l^a is the mass fraction of air in the liquid, P_a is the partial pressure of air, M_a is the molecular mass of air (0.02895 kg/mol) and H = 10000 MPa is Henry's constant. According to the definition of partial density, $\theta_l^a = \omega_l^a \cdot \rho_l$.

5.2 Modelling of seal materials

5.2.1 Basic properties

Three seal materials are selected for modelling and analysing the long-term performance of a drift seal:

1. The compacted bentonite (MX80) that has been extensively characterised as buffer/seal in HLW repositories in crystalline and clay rocks, for instance, by SKB / Clay Technology /ÅKE 10/13/ with determined material parameters;
2. The compacted bentonite-sand mixture with a ratio of MX80/Sand = 70/30 that has being investigated by ANDRA for drift sealing in the COX clay rock /DEL 15/;
3. The compacted claystone-bentonite mixture with a ratio of COX/MX80 = 60/40 as a favourable alternative material for drift sealing in clay rock;

The basic properties of the selected materials are summarised in Table 5.1. The data of the homogeneous MX80 bentonite are taken from literature /ÅKE 10/, while the data of the 70MX80+30Sand and 60COX+40MX80 mixtures are obtained from our own experiments presented in the previous chapter 4. Moreover, the data of the tested COX claystone are also complied herein.

Table 5.1   Basic characteristics of the selected seal materials

Material parameter	MX80 Bentonite	70MX80+ 30Sand	60COX+ 40MX80	COX Claystone
Grain density ρ_s (g/cm^3)	2.78	2.75	2.73	2.70
Dry density ρ_d (g/cm^3)	1.57	1.80	1.90	2.28
Bulk density ρ_b (g/cm^3)	1.84	2.00	2.03	2.41
Void ratio e $(-)$	0.742	0.528	0.437	0.184
Porosity ϕ $(-)$	0.435	0.345	0.304	0.156
Intrinsic permeability k_o (m^2)	5x10^{-21}	2x10^{-20}	6x10^{-20}	6x10^{-21}
Water content w (%)	17.0	9.0	7.0	5.5
Degree of water saturation S_l (%)	61.0	47.0	44.0	81.0

5.2.2 Hydraulic constitutive models

Advective and diffusive transport of liquid and gas are considered the main processes in the drift seal. The following hydraulic models are adopted for description of the hydraulic behaviour of the selected seal materials.

5.2.2.1 Hydraulic conductivity

It is assumed that the advective liquid and gas flows follow Darcy's law:

$$q_\alpha = -\boldsymbol{K}_\alpha(\nabla P_\alpha - \rho_\alpha \boldsymbol{g}) \tag{5.8}$$

where $\boldsymbol{K}_\alpha = \boldsymbol{k}\, k_{r\alpha}/\mu_\alpha$ is the permeability tensor. The intrinsic permeability tensor ($\boldsymbol{k}$) depends on the pore structure of the porous medium. It is assumed here that the hydraulic properties are isotropic for the seal materials, $\boldsymbol{k} \rightarrow k$. $k_{r\alpha}$ is the value of relative permeability that controls the variation of permeability in the unsaturated regime and μ_α denotes the dynamic viscosity. α stands either for l or g depending on whether liquid or gas flow is considered. $\boldsymbol{g}$ is the gravity vector. The variation of intrinsic permeability with porosity is given by:

$$k = k_o \cdot \frac{\phi^3}{(1-\phi)^2} \cdot \frac{(1-\phi_0)^2}{\phi_0^3} \tag{5.9}$$

where ϕ_0 is a reference porosity. Based on the measured data (Table 5.1), the k–ϕ relationships for the seal materials are illustrated in Fig. 5.2. Obviously, the permeability decreases with decreasing porosity.

5.2.2.2 Relative permeability

The relative permeabilities of the liquid and gas phases are dependent on the degree of liquid saturation according to:

$$k_{rl} = A \cdot S_l^\lambda \tag{5.10a}$$

$$k_{rg} = 1 - k_{rl} \tag{5.10b}$$

where S_l is the degree of liquid saturation defined in equation (5.11), A and λ are parameters. $A = 1$ is commonly adapted, whereas λ depends on the material properties and varies in a range between 2 and 5 for the clay-based materials. Fig. 5.3 illustrates

the relative liquid and gas permeability with $\lambda = 2, 3, 4, 5$ as a function of degree of water saturation. It is obvious that the effective liquid flow is strongly dependent on the λ-value. At $\lambda = 5$, the liquid flow firstly occurs as the saturation degree is over 40 %.
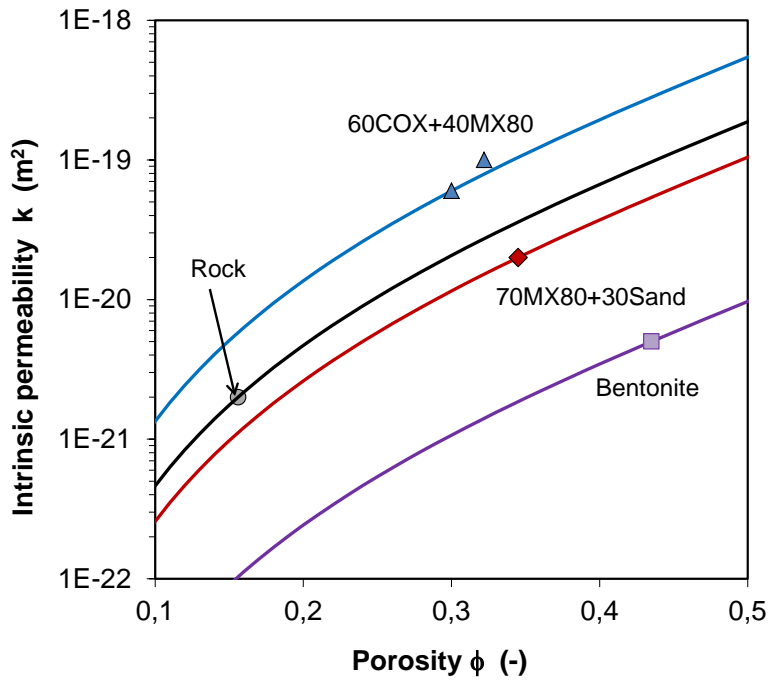
Fig. 5.2   Intrinsic permeability as a function of porosity for the seal materials
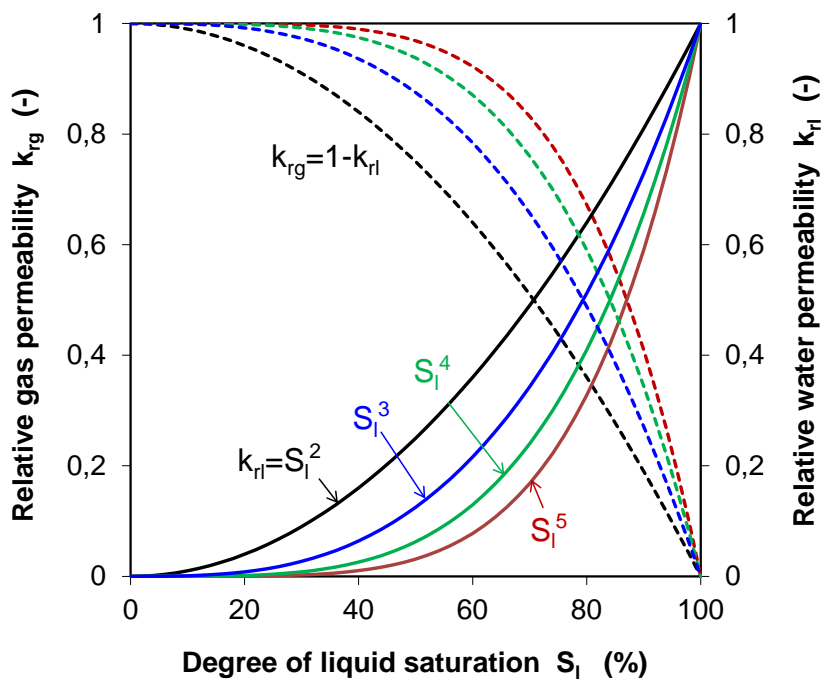
Fig. 5.3   Relative water and gas permeability as a function of water saturation

The degree of liquid saturation S_l is defined as

$$S_l = \frac{\rho_d \cdot w}{\rho_l \cdot \varphi}$$
(5.11)

where w is the liquid water content, ρ_l the liquid density, ρ_d the dry density and φ the porosity of the solid material.

5.2.2.3   Vapour diffusion

The molecular diffusion of vapour is governed by Fick's law:

$$\boldsymbol{i}_g^w = -\boldsymbol{D}_g^w \nabla \omega_g^w = -\left(\phi \rho_g S_g \tau \boldsymbol{D}_m^w I + \rho_g \boldsymbol{D}_g'\right) \cdot \nabla \omega_g^w$$
(5.12)

where $\boldsymbol{i}_g^w$ is the non-advective mass flux of water in gas, $\boldsymbol{D}_g^w$ is the dispersion tensor, ω_g^w is the mass fraction of water in gas, τ is the tortuosity and $\boldsymbol{D}_g'$ is the mechanical dispersion tensor. Usually, a constant dispersion coefficient corresponding to the molecular diffusion of vapour in air is assumed:

$$D_m^w = \tau D \left(\frac{(273.15+T)^n}{P_g}\right)$$
(5.13)

where P_g is given in MPa. The parameters $\tau = 1$, $n = 2.3$ and $D = 5.9 \cdot 10^{-12}$ m²/s are adopted for the seal materials. $\boldsymbol{D}_g'$ can be neglected if air flow is insignificant.

5.2.2.4   Water retention curve

In the highly compacted clay-based materials, the hydration is an essential process of water transport in humid conditions, which is governed by the relationship between degree of water saturation S_l and matric suction s (= P_g - P_l), usually called water retention curve. The suction is determined by the psychrometric law (equation 4.1 or 5.6). The van Genuchten model /VAN 80/ is usually applied for approaching the S_l - s relationship

$$S_l = \left[1 + \left(\frac{s}{P_o}\right)^{\frac{1}{1-\beta}}\right]^{-\beta}$$
(5.14)

where P_o and β are the material parameters. Based on the test data presented in section 4.3 (cf. Fig.4.4a-d), the retention parameters of the selected seal materials will be estimated below.

Taking the density of normal water $\rho_w = 1.0 \ g/cm^3$ and the parameters ρ_d and ϕ constant for the materials in volume-constraint conditions, the degree of water saturation S_l is obtained from the measured water content w according to equation (5.11). Fig. 5.4 shows the water retention curves for the bentonite (a), bentonite-sand mixture (b), claystone-bentonite mixture (c), and claystone (d), respectively. It can be identified that the S_l-values at low suctions close and equal to zero are over 100 % indicating "over-saturation". The maximum values are S_{lm} = 170 % for the compacted bentonite with a dry density of 1.57 g/cm³, S_{lm} = 150 % for 70MX80+30Sand mixture, S_{lm} = 120 % for 60COX+40MX80 mixture, and S_{lm} = 120 % for the claystone. A major reason for the calculated "oversaturation" may be that the actual density of water in such highly-compacted clay materials is higher than the normal one. Values of up to 1.4 g/cm³ are reported in literature /MIT 76/ for the density of adsorbed water on sodium montmorillonite (a 10 Å thick layer). Moreover, due to the compressibility of water, the water density in the highly-compacted clay materials may increase with swelling pressure in rigid confinement.

The "oversaturation" brings difficulties for the determination of the water retention curve. Taking into account the confined and unconfined conditions of the samples, two evaluation methods are suggested for approximation of the S_l - s relationship.

When the water content – suction ($w - s$) data are obtained from unconfined samples (free-swelling), the corresponding degrees of water saturation S_l for a given porosity (φ) and dry density (ρ_d) can be obtained according to equation (5.11) using the normal water density of $\rho_w = 1.0 \ g/cm^3$. The part of the "oversaturation" with $S_l > 100$ % is neglected, for instance, for the compacted bentonite in Fig. 5.4a.

When the $w - s$ data are obtained from volume-constraint samples, the maximum water content reached at zero suction is considered corresponding to the full saturation, w_m $\rightarrow S_{lm}$ = 100 %, and the degree of water saturation at any suction is defined as a ratio of the water content to its maximum

$$S_l = \frac{w}{w_m} = \frac{S_l}{S_{lm}} \tag{5.15}$$

Based on the measured $w - s$ data from the confined and unconfined mixtures, the S_l - s relationships approached by the van Genuchten model (Eq. 5.14) are established for each material. The associated parameter values are summarized in Table 5.2.
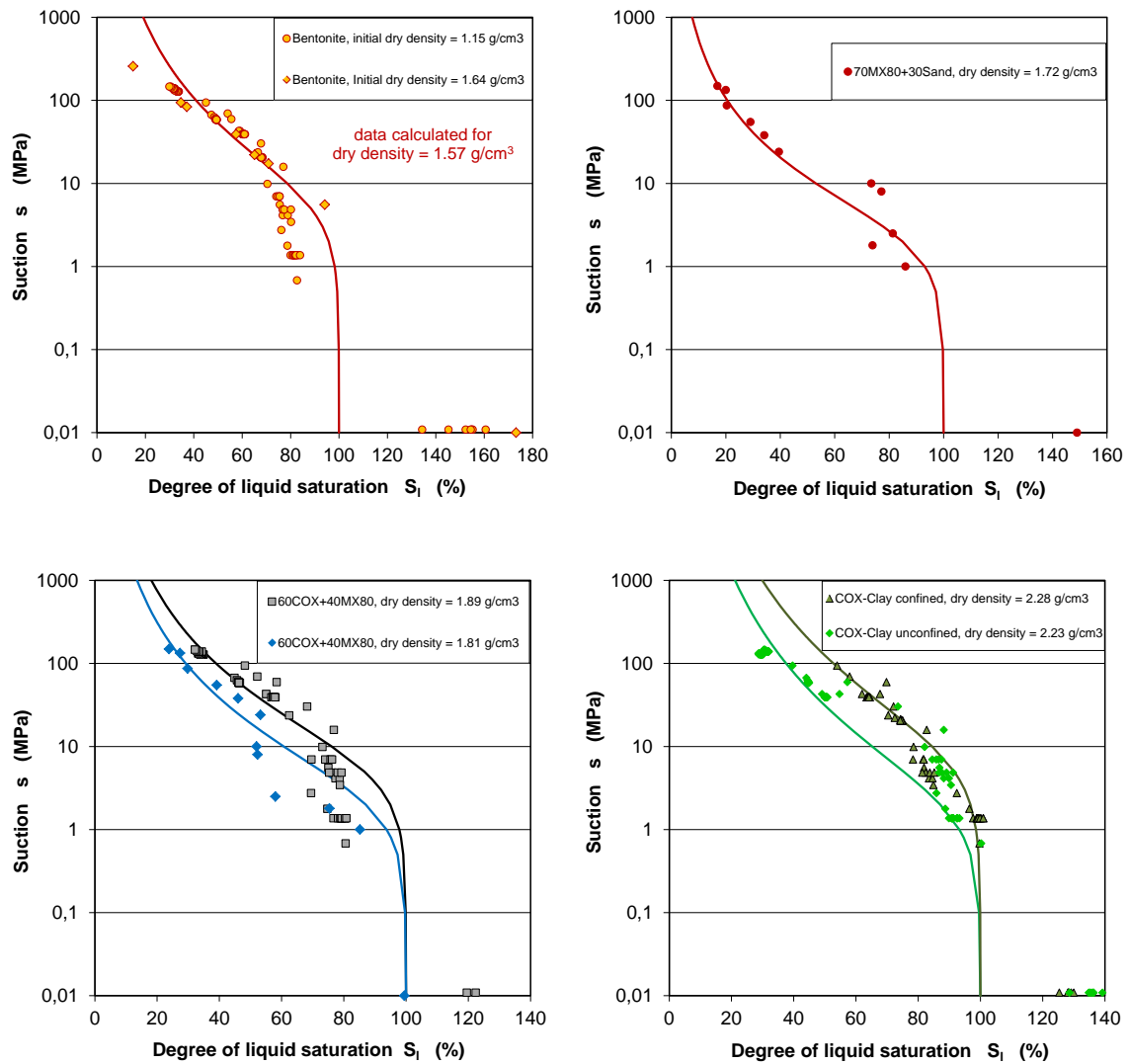
Fig. 5.4   Water retention curves expressed by the van Genuchten model for the se-
lected seal materials

Fig. 5.5 illustrates the water retention curves for the compacted bentonite with a dry
density of 1.57 g/cm³ (a), bentonite-sand mixture with a dry density of 1.72 g/cm³ (b),
claystone-bentonite mixture with dry densities of 1.89 and 1.81 g/cm³ (c), and claystone
with dry densities of 2.28 and 2.23 g/cm³ (d), respectively. For the bentonite two water
retention curves are established: curve A matching the data in the low saturation area
(S_l < 80 %) and curve B closing to the data in the high saturation range. It is difficult for
the van Genuchten model to gather a unique curve for the whole range. The retention
curve for the compacted bentonite-sand mixture is determined by the evaluated satura-
tion degree according to equation (5.15). For the compacted 60COX+40MX80 mixture,
two curves are estimated for the upper and low boundary respectively. For the clay-

stone at a given suction, the degree of saturation in unconfined condition (b) seems to be relatively lower than in confined condition (a). A reversal conclusion shall be reasonable. More precise tests are needed to confirm the conclusion.

Table 5.2   Water retention parameters associated in the van Genuchten model for the seal materials

Material parameter	MX80 bentonite-a	MX80 bentonite-b	70MX80+ 30Sand	60COX+ 40MX80-a	60COX+ 40MX80-b	COX Clay-a	COX Clay-b
P_o (MPa)	6.5	2.0	0.3	0.5	0.1	0.5	0.2
β (-)	0.25	0.15	0.25	0.15	0.16	0.15	0.15
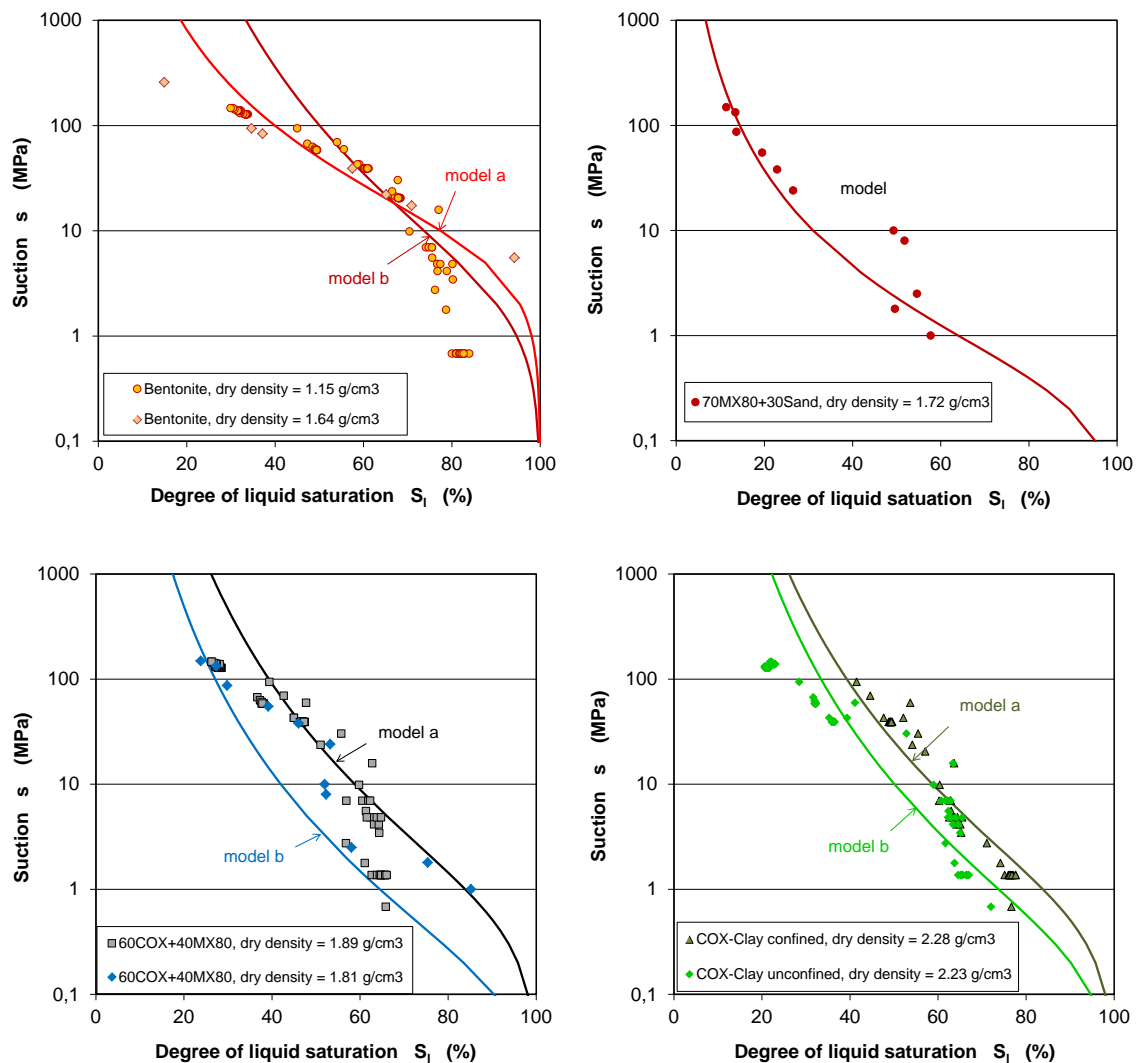
Fig. 5.5   Water retention curves expressed by the van Genuchten model for the selected seal materials

It can also be recognized that the van Genuchten model largely overestimates the suctions in the low saturation area and $s \to \infty$ as $S_l \to 0$. This shortage may be overcome by adding a term for suction to approach the upper limit /UPC 15/

$$S_l = \left[1 + \left(\frac{s}{P_o}\right)^{\frac{1}{1-\beta}}\right]^{-\beta} \cdot \left[1 - \frac{s}{P_1}\right]^{-\gamma} \tag{5.16}$$

where P_o, β, P_1 and γ are the material parameters. The parameters are estimated by fitting the data and summarized in Table 5.3. The parameter $\gamma = 1$ and the maximum suction $P_1 = 350\ MPa$ are taken for all the materials. The modified retention curves are compared with the data in Fig. 5.6. It is obvious that the modified model fits the data for the whole range and $s \to P_1$ as $S_l \to 0$.

Table 5.3   Water retention parameters associated in the modified van Genuchten model for the seal materials

Material parameter	MX80 bentonite	70MX80+ 30Sand	60COX+ 40MX80-a	60COX+ 40MX80-b	COX Clay-a	COX Clay-b
P_o (MPa)	1.1	0.2	0.1	0.03	0.15	0.05
β (-)	0.1	0.2	0.1	0.1	0.1	0.1
P_1 (MPa)	350	350	350	350	350	350
γ (-)	1	1	1	1	1	1

87
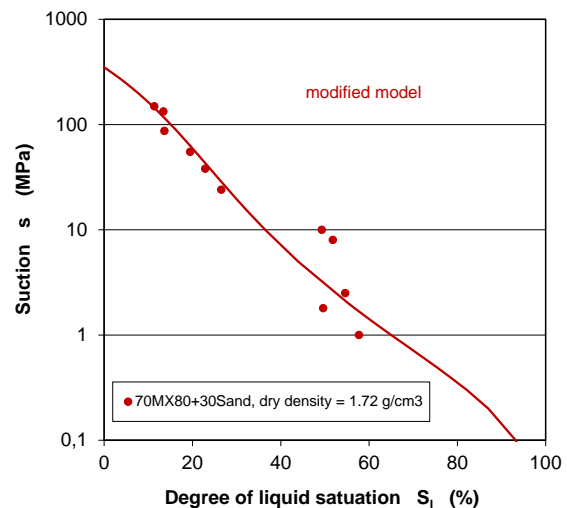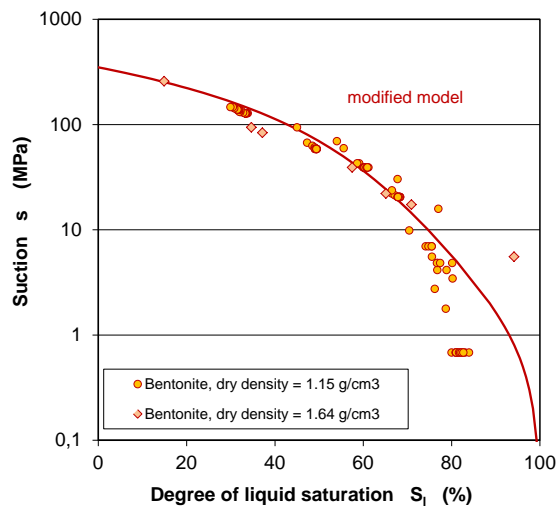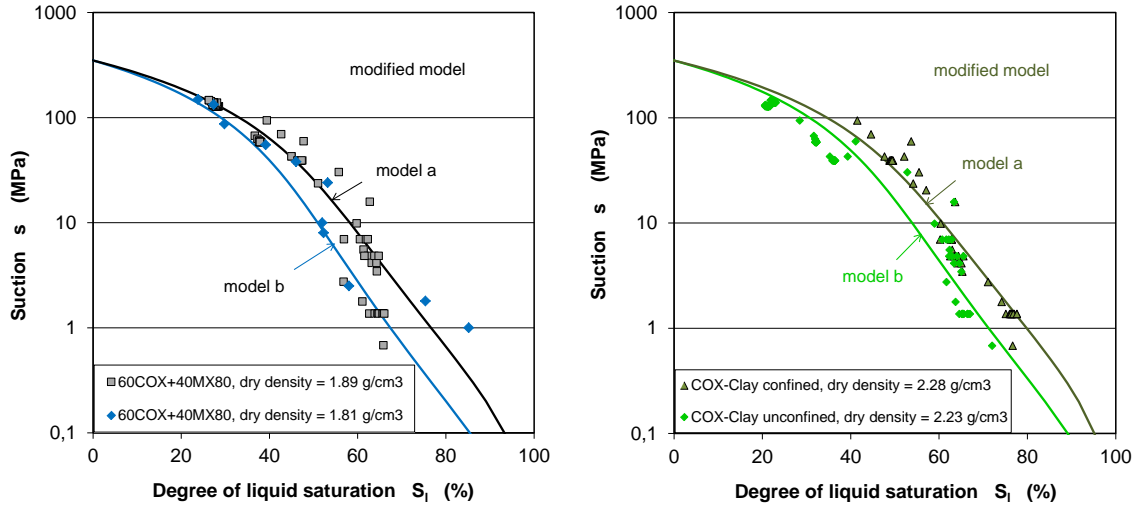
Fig. 5.6   Water retention curves expressed by the modified van Genuchten model
            for the selected seal materials

5.2.3   Mechanic constitutive models

5.2.3.1   Stress invariants

Mean effective stress: $p = \dfrac{1}{3}(\sigma'_x + \sigma'_y + \sigma'_z)$ (5.17)

where $\sigma'_x, \sigma'_y, \sigma'_z$ are the effective stresses.

Second stress invariant: $J = \sqrt{\dfrac{1}{2} trace(\mathbf{s}:\mathbf{s})} = \dfrac{1}{\sqrt{3}}q,\quad \mathbf{s} = \boldsymbol{\sigma} - p\mathbf{I}$ (5.18)

$$q = \dfrac{1}{\sqrt{2}}\sqrt{(\sigma'_x - \sigma'_y)^2 + (\sigma'_y - \sigma')^2 + (\sigma'_z - \sigma'_x)^2 + 6(\tau'_{xy} + \tau'_{yz} + \tau'_{zx})}$$ (5.19)

where q is the deviatoric stress, $\tau'_{xy}, \tau'_{yzy}, \tau'_{zx}$ are the shear stresses.

Lode's angle: $\theta = -\dfrac{1}{3}\sin^{-1}(1.5\sqrt{3}\det\mathbf{s}/J^3)$ (5.20)

$\theta = -\pi/6$ means triaxial compression and $\theta = \pi/6$ extension.

88

5.2.3.2 Elasto-plastic model

In saturated porous materials, the mechanical behaviour is best understood in terms of effective stress $\boldsymbol{\sigma}' = \boldsymbol{\sigma} - P_l\boldsymbol{m}$, where $\boldsymbol{m}^T$ is an auxiliary vector $[1,1,1,0,0,0]$. For unsaturated materials it is necessary to consider two independent stress variables: net stresses $(\boldsymbol{\sigma} - P_l\boldsymbol{m})$ and capillary suction $s = (P_g - P_l)$. The net stress is the excess of total stress over gas pressure. If full saturation is achieved, the net stress becomes effective stress. The mechanical constitutive equation takes the incremental form:

$$d\boldsymbol{\sigma}' = \boldsymbol{D}d\boldsymbol{\varepsilon} + \boldsymbol{h}ds \tag{5.21}$$

where $\boldsymbol{\sigma}'$ is used for net stresses, $\boldsymbol{\varepsilon}$ is the strain sensor. $\boldsymbol{D}$ is the constitutive stiffness matrix, defined by Young's modulus E, shear modulus G and Poisson's ratio v, and $\boldsymbol{h}$ is a constitutive vector relating changes of suction to changes in net stress.

An elasto-plastic model named Barcelona Basic Model (BBM) is implemented in CODE-BRIGHT, which is able to represent many mechanical features of unsaturated materials. The yield function is expressed by

$$q^2 - M^2(p + p_s)(p_o - p) = 0 \tag{5.22}$$

where p_o the net isotropic yield stress, p_s the isotropic tensile strength depending on suction s, and M a constant value characterising the critical failure state line

$$q = M \cdot p \tag{5.23}$$

It is assumed that the apparent cohesion increases with suction by

$$p_s = p_{so} + k \cdot s \tag{5.24}$$

where p_{so} is the isotropic tensile strength in saturated conditions, k is a parameter.

The net isotropic yield stress p_o is considered to be dependent on suction through

$$p_o = p^c\left(\frac{p_o^*}{p^c}\right)^{\frac{\lambda(o)-k_{io}}{\lambda(s)-k_{io}}} \quad ; \quad \lambda(s) = \lambda(o)\left[(1-r)\exp(-\beta s) + r\right] \tag{5.25}$$

where p_o^* is the net yield stress for saturated conditions, $\lambda(o)$ and $\lambda(s)$ are the slopes of the virgin compression lines for saturated and unsaturated conditions, r is a constant related to the matrix stiffness, β provides the rate of change of $\lambda(s)$ with suction, k_{io} is

the initial slope of the isotropic unloading-reloading paths for saturated conditions, p^c is a reference stress.

Hardening depends on plastic strain according to

$$\frac{dp_o^*}{p_o^*} = \frac{v}{\lambda(o) - k_{io}} d\varepsilon_v^p \tag{5.26}$$

where $v = 1 + e$ is the specific volume, e is the void ratio.

Volumetric elastic strains induced by changes of net mean stress and suction are given by

$$d\varepsilon_v^e = d\varepsilon_{vp}^e + d\varepsilon_{vs}^e \tag{5.27a}$$

$$d\varepsilon_{vp}^e = \frac{k_i}{v} \frac{dp}{p}; \qquad\qquad k_i = k_{io}(1 + \alpha_i s) \tag{5.27b}$$

$$d\varepsilon_{vs}^e = \frac{k_s}{v} \frac{ds}{s + p_{at}}; \qquad\qquad k_s = k_{so}\left(1 + \alpha_{sp} \ln\left(\frac{p}{p_{ref}}\right)\right)\exp(\alpha_{ss}s) \tag{5.27c}$$

where k_{io} and k_i are the slopes of the isotropic unloading-reloading paths for saturated and unsaturated conditions, respectively, k_{so} and k_s are the slopes of the wetting-drying paths for saturated and unsaturated conditions at a given stress p in the elastic domain, p_{at} and p_{ref} are the atmospheric pressure and the reference pressure, α_i, α_{sp} and α_{ss} are parameters.

Deviatoric elastic deformations are computed through shear modulus G and the Poisson ratio v:

$$d\varepsilon_q^e = \frac{G}{3} dq; \qquad\qquad G = \frac{3(1 - 2v)}{2(1 + v)} \frac{(1 + e)}{k_i} p \tag{5.28}$$

5.2.3.3   Parameters

For the MX80 bentonite with a dry density of 1.57 g/cm^3 in the BRIE experiment /ÅKE 13/, the parameter values were obtained on the basis of the data of the FEBEX bentonite with a dry density of 1.55 g/cm^3 /GEN 98/. Only the parameter k_{io} - value is changed

from 0.05 (FEBEX) to 0.02 (MX80) for matching the relatively higher swelling pressure measured on MX80 bentonite. Most of the mechanical parameters for the 70MX80+30Sand and 60COX+40MX80 mixtures are obtained directly from our laboratory experiments and partly by back calculations.

Fig. 5.7 shows the compaction curves of the bentonite-sand and claystone-bentonite mixtures, based on which the elastic and plastic stiffness parameters k_{io} and $\lambda(s)$ as well as the yield stress p_o^* are obtained. Since the parameter k_{io} of the claystone-bentonite mixture shows almost independence of the water saturation, the parameter $\alpha_i = 0$ is thus assumed. The comparison between the compaction curves indicates that both the compacted mixtures are much stiffer than the pure bentonite.
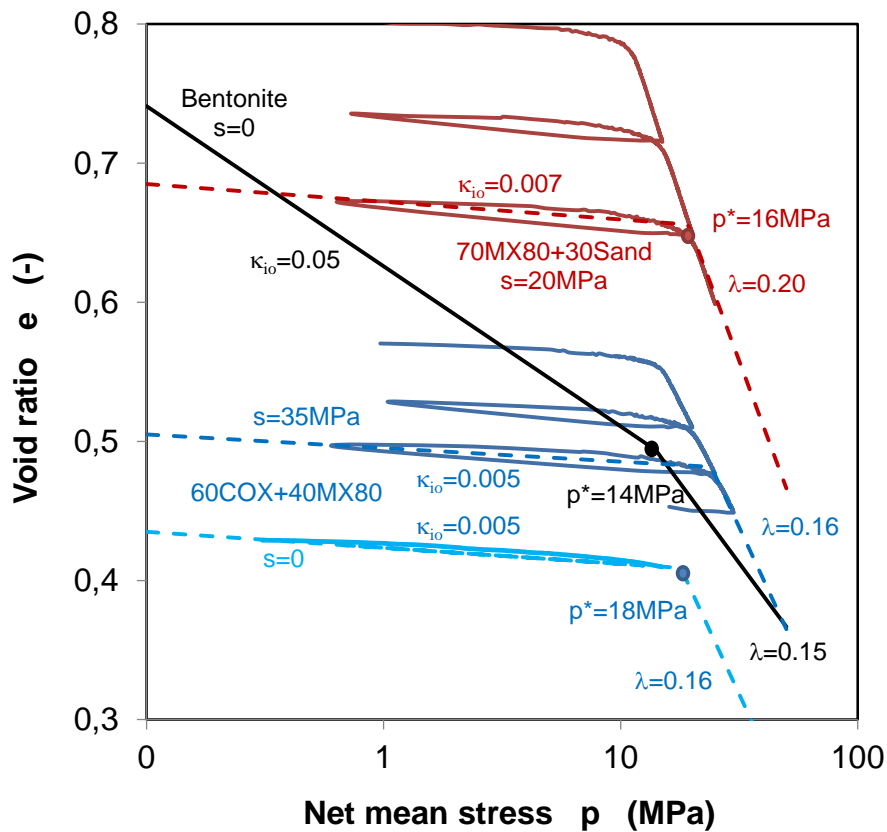
Fig. 5.7   Determination of the compaction parameters for the seal materials

The initial elastic parameters K, G and E are calculated for saturated conditions at $p = 1$ MPa and $e = e_o$, $K = p(1+e)/k_{io}$, $G = 3K(1-2\nu)/2(1+\nu)$, $E = 2G(1+\nu)$.

The swelling parameters k_{so}, α_{sp} and α_{ss} are estimated by back calculations of the swelling pressures measured on the bentonite-sand and claystone-bentonite mixtures (see later). The estimated values of the BBM parameters are summarized in Table 5.5 for the selected seal materials.

Table 5.5   BBM model parameters for the selected seal materials

Parameter in equation	Symbol	Unit	Bentonite	70MX80+ 30Sand	60COX+ 40MX80
5.27b	k_{io}	-	0.05/0.02	0.007	0.005
5.27b	α_i	-	0.003	-	-
5.27c	k_{so}	-	0.3	0.3	0.022
5.27c	α_{sp}	-	-0.1638	-	-
5.27c	α_{ss}	MPa^{-1}	-0.03	-	-
5.27c	p_{ref}	MPa	0.01	-	-
5.28	ν	-	0.4	0.35	0.35
Bulk modulus	K	MPa	35	285	340
Shear modulus	G	MPa	7.5	95	113
Young's modulus	E	MPa	20	255	305
5.23	M	-	1.0	-	-
5.24	k	-	-0.1	-	-
5.25	p^c	MPa	0.1	-	-
5.25	p_o^*	MPa	14	16	18
5.25/5.26	$\lambda(o)$	-	0.15	0,2	0,16
5.25	r	-	0.75	-	-
5.25	$ß$	MPa^{-1}	0.05	-	-

5.2.4   Simulations of water saturation and swelling pressure

5.2.4.1   Water saturation

The water saturation tests on the compacted 70MX80+30Sand and 60COX+40MX80 mixtures as well as the COX claystone have been described in section 4.4. Most of them are modelled in this section. Additionally, the previous hydration tests performed on the pure MX80 bentonite /KRÖ 04/ are also simulated. The basic characteristics of the samples are summarized in Table 5.6.

Table 5.6   Basic characteristics of the samples in the water saturation tests: MX80 bentonite, 70MX80+30Sand and 60COX+40MX80 mixtures, and COX claystone

Parameter	Bentonite	70MX80+30Sand		60COX+40MX80			COX Clay
Test	/KRÖ 04/	1 group-II	2 group-III	1 group-I	2 group-III	3 group-III	1 group-II
D (mm)	50.0	50.0	50,0	50.0	50,0	50,0	47.2
L (mm)	10.0	98.0	100,0	100.0	100,0	100,0	101.3
ρ_d (g/cm^3)	1.52	1.49	1,79	1.79	1,87	1,91	2.29
ϕ (%)	45.7	46.0	35,0	34.5	31,0	30,0	15.1
w (%)	10.0	9.0	9,0	5.45	7,0	7,0	3.70
S_l (%)	33.3	32.7	46,0	30.0	41,6	44,4	58.3

The initially unsaturated samples were placed in steel cylinders of 50 mm diameter and 100 mm length and wetted from an end face with the synthetic clay water at atmospheric pressure. The tests are modelled using CODE-BRIGHT (v3ß) as a coupled HM problem by an axisymmetric geometry with 100 elements as shown in Fig. 5.8. The liquid pressure at the entre face is kept at atmospheric level, P_l = 0.1 MPa, and the atmospheric gas pressure is kept for the whole sample, P_g = 0.1 MPa. The other boundaries are isolated with zero fluid flow, Q_l = 0. The initial suction s_o is obtained from the water retention curve and the initial water saturation S_{lo} for each sample. The initial stresses are nearly zero: $\sigma_1 = \sigma_2 = \sigma_3$ = 0.15 MPa. A constant temperature maintains at 20 °C. The calculations are performed by solving the balance equations of solid (Eq. 5.2), water mass (Eq. 5.3) and stress equilibrium (Eq. 5.5). As a result, the distribution of water saturation in the sample at the end of each saturation period is predicted.
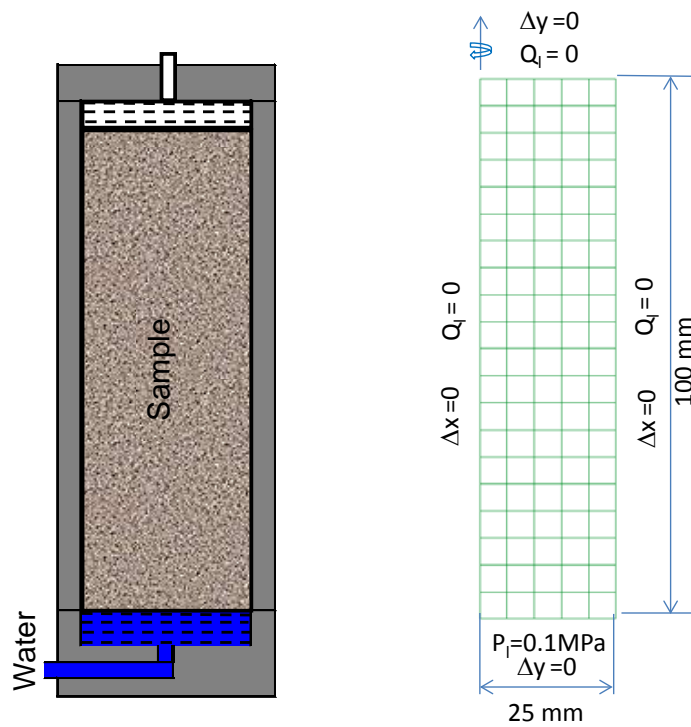
Fig. 5.8   Model geometry and boundary conditions for modelling the water saturation
of the seal materials

5.2.4.1.1 Bentonite

The hydration tests on the compacted MX80 bentonite in /KRÖ 04/ are predicted using different sets of the hydraulic parameters, which have been established here or taken from literature /ÅKE 13/ for the bentonite used in the BRIE-Experiment in Äspö-URL in Sweden and from /GEN 98/ for the bentonite used in the FEBEX-Experiment in Grimsel-URL in Switzerland. The hydraulic parameters and the water retention parameters of the van Genuchten model (Eq. 5.14) are summarized in Table 5.7. Fig. 5.9 shows the water retention curves together with the test data. GRS-A and BRIE model curves are close to each other and agree well with the data in the low saturation range of $S_l <$ 80 %. FEBEX model curve exhibits the same shape but lies slightly below the other curves. GRS-B curve is more close to the data in the high saturation range and below the other curves in this region. For the initial degree of water saturation of S_{lo} = 33.3 % in the bentonite samples, the corresponding suction values s_o are determined from the respective retention curves. The exponent of the power law for the relative permeability, $k_{rl} = S_l^{\lambda}$, is differing from a model to another with $\lambda = 3, 4$ and 5.

94

Table 5.7   Summary of the hydraulic parameters in different models for the bentonite

Material parameter	GRS-A Model	GRS-B Model	BRIE Model /ÅKE 13/	FEBEX Model /VOL 96/
ϕ_o $(-)$	0.43	0.43	0.44	0.43
k_o (m^2)	6×10^{-21}	6×10^{-21}	6.4×10^{-21}	6×10^{-21}
$k_{rl}(-)$	S_l^5	S_l^5	S_l^4	S_l^3
P_o (MPa)	6.5	2.0	10.0	7.0
β $(-)$	0.25	0.15	0.28	0.35
s_o (MPa)	180	1000	165	58
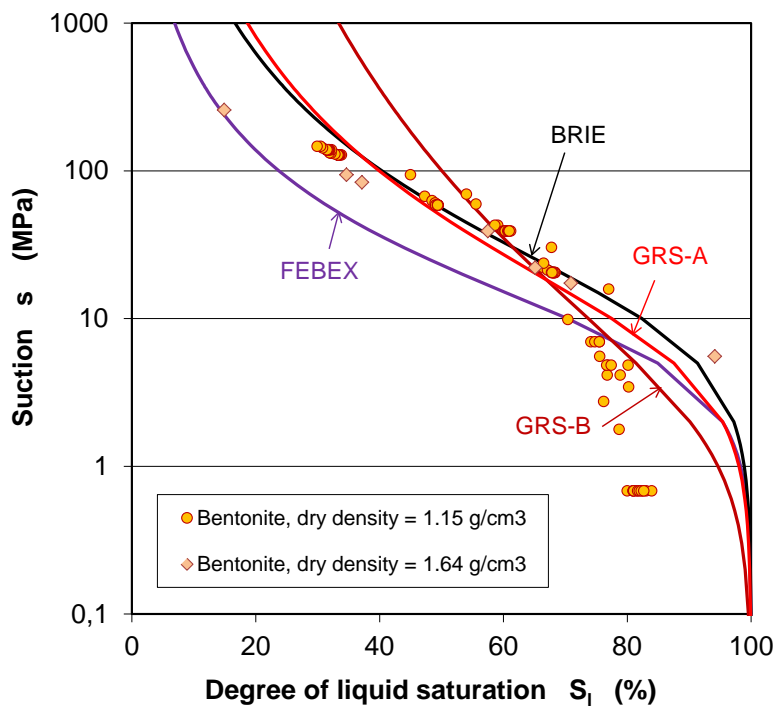
Fig. 5.9   Water retention curves used for modelling the water uptake of the com-
pacted bentonite

The modelling results are compared in Fig. 5.10 with the measured distributions of wa-
ter saturation in the samples at different time periods using models: (a) BRIE, (b)
FEBEX, (c) GRS-A, and (d) GRS-B. It can be seen that the application of the retention
curves of BRIE, FEBEX and GRS-A more or less overestimates the hydration rate, par-
ticularly for the long saturation durations after a month. In contrast, GRS-B model pro-
vides an excellent agreement with the measurements at the various saturation periods.
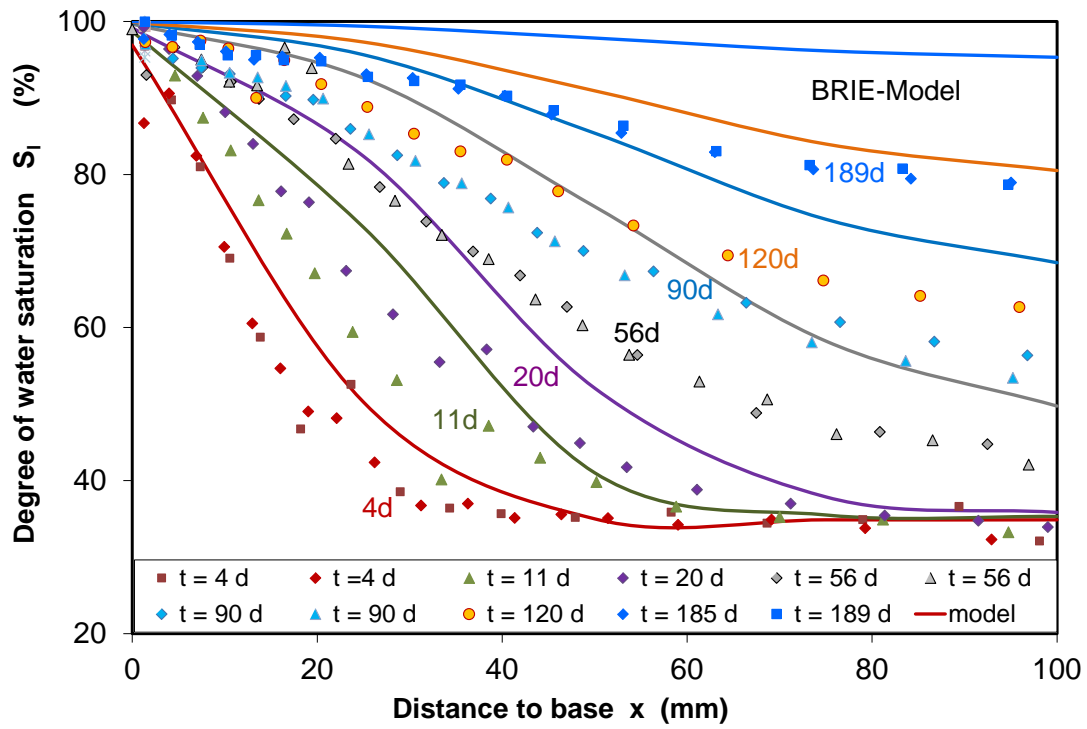
a. Prediction using BRIE model parameters
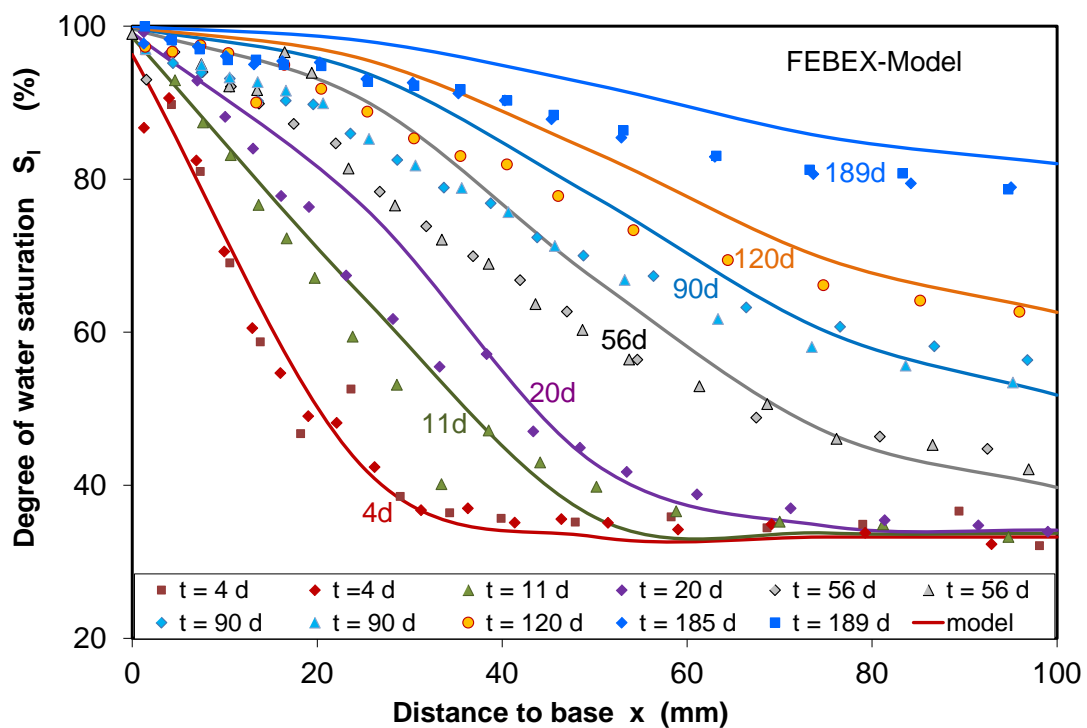
b. Prediction using FEBEX model parameters
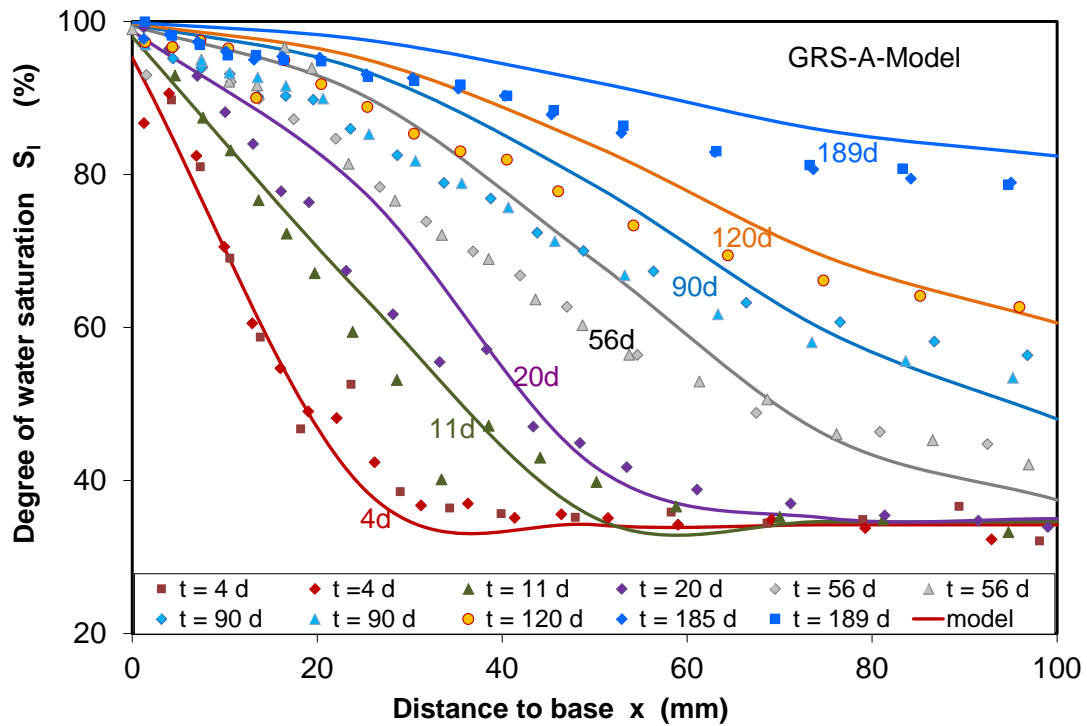
c. Prediction using GRS-A model parameters
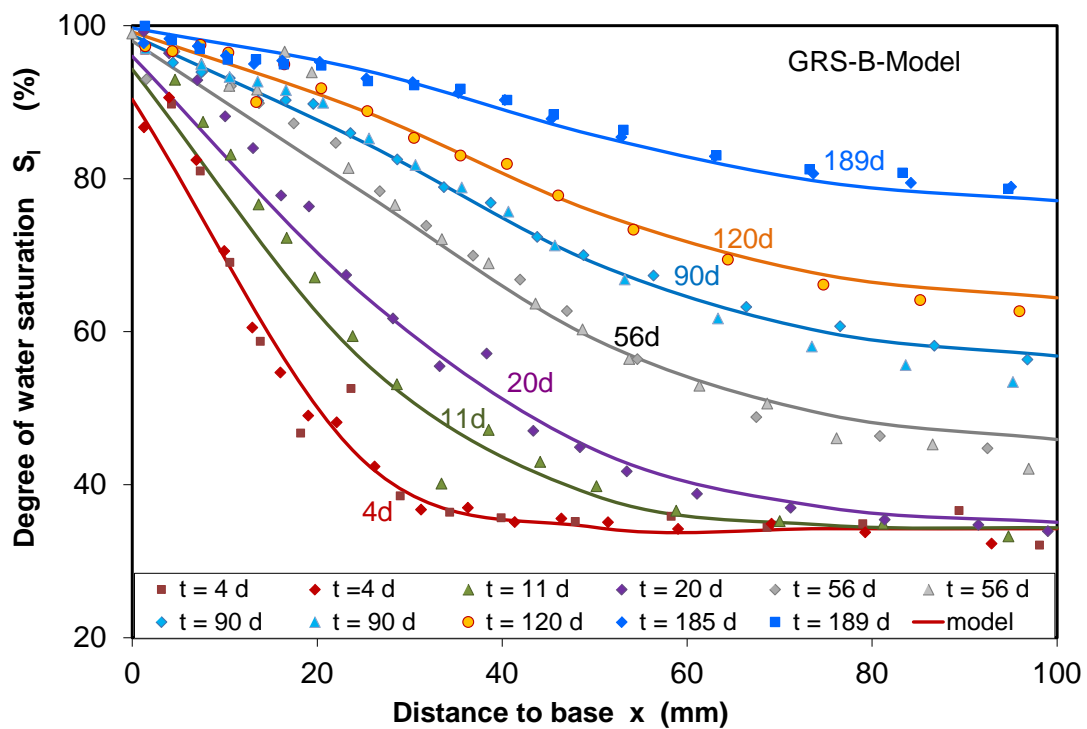
d. Prediction using GRS-B model parameters

Fig. 5.10   Comparison of water saturation measured on MX80 bentonite /KRÖ 04/
and predicted using the different hydraulic parameters

Additionally, the modified retention curve in Fig. 5.6a with the associated parameters in Table 5.3 is also used for modelling the hydration tests. The initial suction of $s_o = 154$ MPa is resulted from the initial saturation degree of $S_{lo} = 33.3$ %. Fig. 5.11 shows the comparison between the model prediction and the data. A good agreement between them is also reached.
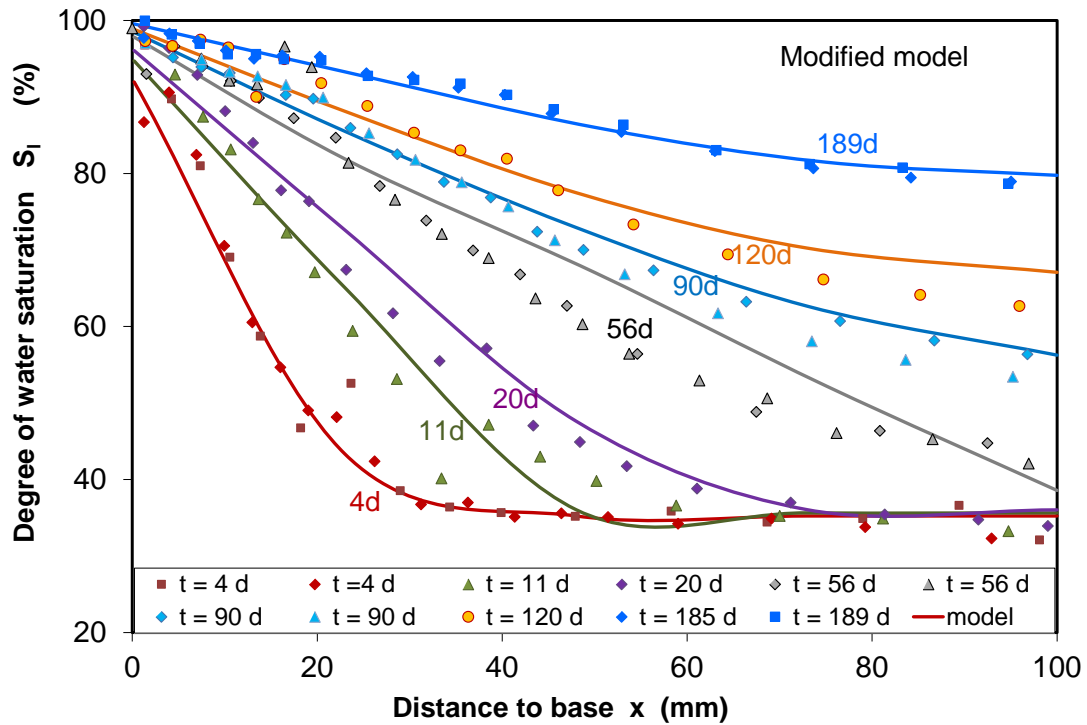
Fig. 5.11   Comparison of water saturation measured on MX80 bentonite /KRÖ 04/ and predicted using the modified water retention curve

5.2.4.1.2 Bentonite-sand mixture

Two water saturation tests on the 70MX80+30Sand mixture are simulated using the van Genuchten retention curve (Fig. 5.5b) and also the modified model (Fig. 5.6b). The associated retention parameters, the other hydraulic parameters, and the initial properties of these two samples are summarized in Table 5.8. The modelling results are compared in Figs. 5.12 with the measured distributions of water saturation in the samples at different time periods. The distribution of water saturation of sample 1 with a porosity of 46 % at 9.5 months can be very well predicted by the models with both the retention curves, while the water saturation in sample 2 with a low porosity of 35 % at 14 months is largely overestimated. The saturation time is largely dependent on the porosity of the material. The lower the porosity, the longer the saturation is required.

Table 5.8   Hydraulic parameters of the bentonite-sand mixture

Hydraulic parameters	ϕ_o = 0.345, k_o = 2x10^{-20} m^2, $k_{rl} = S_l^5$
van Genuchten model (1)	P_o = 0.3 MPa, β = 0.25
Modified model (2)	P_o = 0.2 MPa, β = 0.2, P_1 = 350 MPa, λ = 1
Initial properties of sample 1	ϕ_o = 0.46, S_{lo} = 32.7 %, s_{o-1} = 9 MPa, s_{o-2} = 15 MPa
Initial properties of sample 2	ϕ_o = 0.35, S_{lo} = 46.0 %, s_{o-1} = 3 MPa, s_{o-2} = 4 MPa
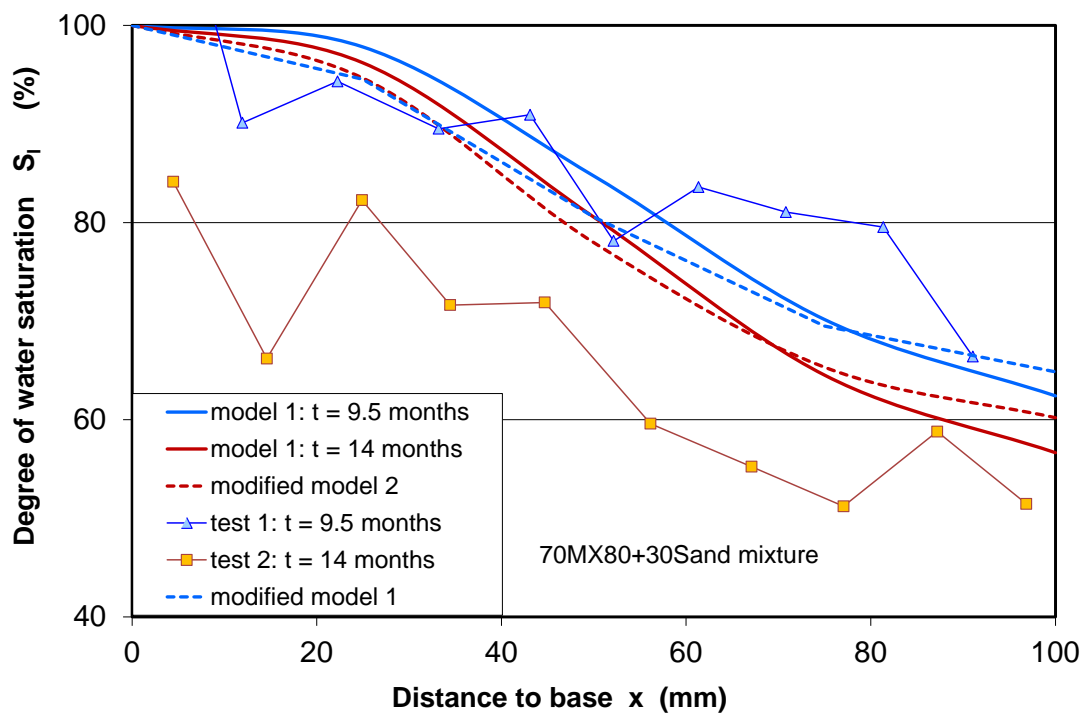
Fig. 5.12   Predictions of the water saturation in the bentonite-sand mixture using the van Genuchten model (solid line) and the modified model (dash line)

5.2.4.1.3 Claystone-bentonite mixture

Three water saturation tests on the 60COX+40MX80 mixture are simulated using the van Genuchten retention curve b in Fig. 5.5c and the modified model b in Fig. 5.6c for a dry density of 1.81 g/cm^3. The associated retention parameters, the other hydraulic parameters, and the initial properties of the tested samples are summarized in Table 5.9. The modelling results are illustrated in Fig. 5.13 with the measured distributions of wa-

ter saturation in the samples at different time periods. The predictions using the van Genuchten retention curve (solid line) and the modified retention curve (dash line) are close to the measured data for sample 1 but slightly overestimate for the other two samples. The measured low degrees of water saturation in the water entre sides are probably caused by measurement errors.

Table 5.9   Hydraulic parameters of the claystone-bentonite mixture

| Hydraulic parameters	ϕ_o = 0.304, k_o = 6x10^{-20} m^2, $k_{rl} = S_l^5$
van Genuchten model (1)	P_o = 0.1 MPa, β = 0.16
Modified model (2)	P_o = 0.03 MPa, β = 0.1, P_1 = 350 MPa, λ = 1
Sample-1 initial properties	ϕ_o = 0.345, S_{lo} = 30.0 %, s_{o-1} = 400 MPa, s_{o-2} = 87 MPa
Sample-2 initial properties	ϕ_o = 0.31, S_{lo} = 41.6 %, s_{o-1} = 75 MPa, s_{o-2} = 35 MPa
Sample-3 initial properties	ϕ_o = 0.30, S_{lo} = 44.4 %, s_{o-1} = 50 MPa, s_{o-2} = 22 MPa
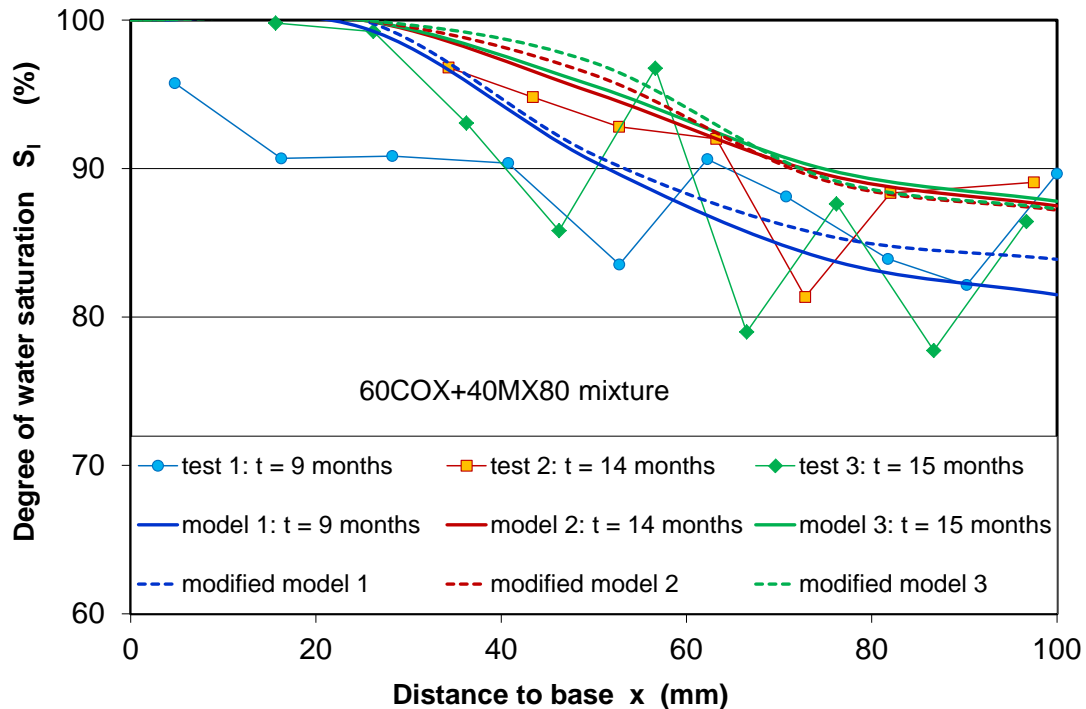
Fig. 5.13   Predictions of the water saturation in the claystone-bentonite mixture using the van Genuchten model (solid line) and the modified model (dash line)

5.2.4.1.4 Claystone

A water saturation test on the COX claystone is simulated using the van Genuchten retention curve b in Fig. 5.5d and the modified model b in Fig. 5.6d obtained from the unconfined samples. The associated retention parameters, the other hydraulic parameters, and the initial properties of the sample are summarized in Table 5.10. The modelling results based on both the models are shown in Fig. 5.14 together with the measured distribution of water saturation in the sample after testing at 9.5 months. The model curves lie within the scatter of the data.

Table 5.10   Hydraulic parameters of the COX claystone

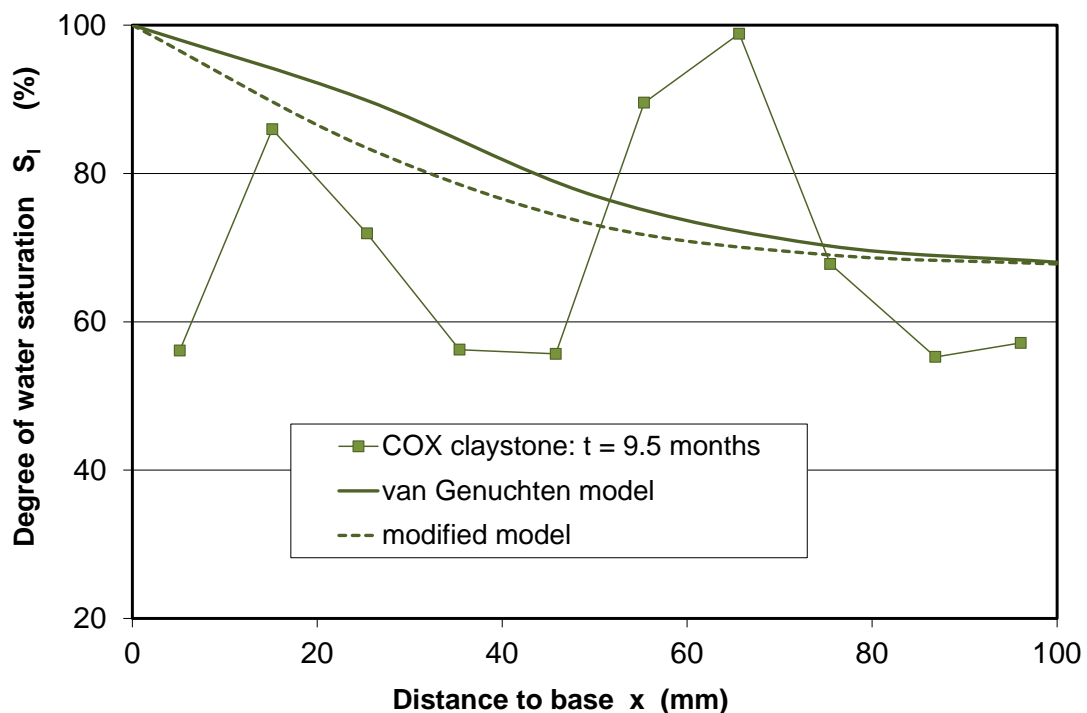| Hydraulic parameters	ϕ_o = 0.156, k_o = 6x10^{-21} m^2, $k_{rl} = S_l^5$
van Genuchten model (1)	P_o = 0.2 MPa, β = 0.15
Modified model (2)	P_o = 0.05 MPa, β = 0.1, P_1 = 350 MPa, λ = 1
Sample initial properties	ϕ_o = 0.151, S_{lo} = 58.3 %, s_{o-1} = 4 MPa, s_{o-2} = 6 MPa

Fig. 5.14   Predictions of the water saturation in the claystone mixture using the van Genuchten model (solid line) and the modified model (dash line)

5.2.4.2 Swelling pressure

5.2.4.2.1 Bentonite-based mixtures

The swelling pressure tests on the compacted bentonite-sand (70MX80+30Sand) and claystone-bentonite (60COX+40MX80) mixtures have been described in section 4.5 and selected for modelling. The initial unsaturated samples in steel cells of 50 mm diameter and 30 mm height are modelled by an axisymmetric geometry with 50 elements, see Fig. 5.15. The initial properties of the mixtures are

- 70MX80+30Sand: ρ_d = 1.82 g/cm^3, ϕ = 34.0 %, w_o = 11.0 %, S_{lo} = 59.0 % g/cm^3
- 60COX+40MX80: ρ_d = 1.86 g/cm^3, ϕ = 32.0 %, w_o = 10.0 %, S_{lo} = 58.0 % g/cm^3

The samples are confined with the fixed boundaries. The liquid pressure at the bottom is kept at atmospheric level, $P_l = 0.1$ MPa, and the gas pressure is atmospheric, $P_g = 0.1$ MPa. The other boundaries are isolated with zero fluid flow, $Q_l = 0$. The low initial stresses are applied with $\sigma_1 = \sigma_2 = \sigma_3 = 0.11$ MPa. A constant temperature is kept at 20 °C. The calculations are performed by solving the balance equations of solid (Eq. 5.2), water mass (Eq. 5.3) and stress equilibrium (Eq. 5.5).
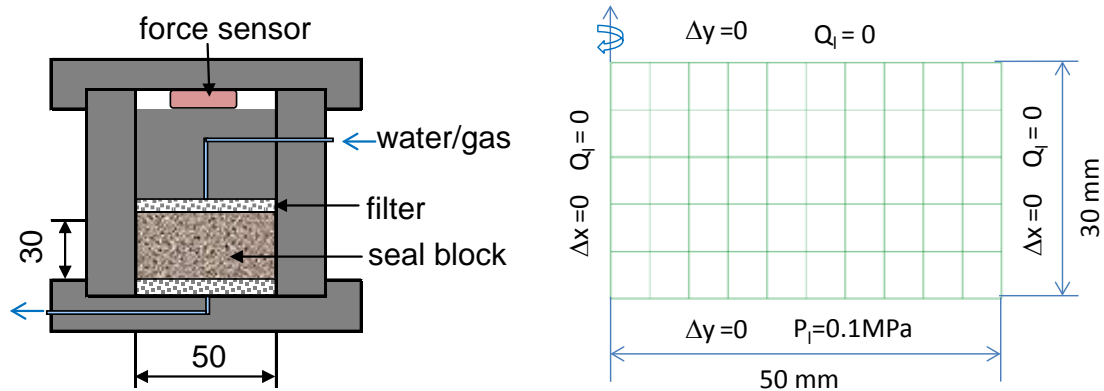
Fig. 5.15 Model geometry and boundary conditions for modelling the swelling pressure of the seal materials

The BBM model with the estimated mechanical parameters summarized in Table 5.5 is adopted for the mechanical behaviour of the seal materials. The hydraulic models and parameters in Table 5.1 are adopted. The water retention curve in Fig. 5.5b and the curve b in Fig. 5.5c are adopted for 70MX80+30Sand and 60COX+40MX80 mixture,

respectively. Both have been already used for modelling the water saturation tests, see Figs. 5.12 and 5.13. The initial suctions are obtained to be s_o = 1.4 MPa for 70MX80+30Sand and s_o = 2 MPa for 60COX+40MX80.

Fig. 5.16 compares the modelled and measured evolution of swelling pressure for 70MX80+30Sand (a) and 60COX+40MX80 (b) mixture respectively. The sensitivity of the relative permeability parameter λ is examined using two values of λ = 5 for model A and λ = 3 for model B. The calculated development of swelling pressure with λ = 3 (model B) is faster than using λ = 5. But the increased rates are still lower than the observations during the first stage. Obviously, the evolution of swelling pressure is directly related to the hydration process. Even though the fluctuations of the swelling pressure could not be reflected, the maximum values are provided by the model: p_s = 5.6 MPa for the bentonite-sand mixture and p_s = 3.7 MPa for the claystone-bentonite mixture. Since the swelling pressures are much lower than those pre-consolidation pressures of 14 to 18 MPa, the seal materials remain in the elastic domain during hydration and the plastic parameters the plastic parameters do not play any role in the computation /GEN 98/.

a.   Bentonite-sand mixture

103
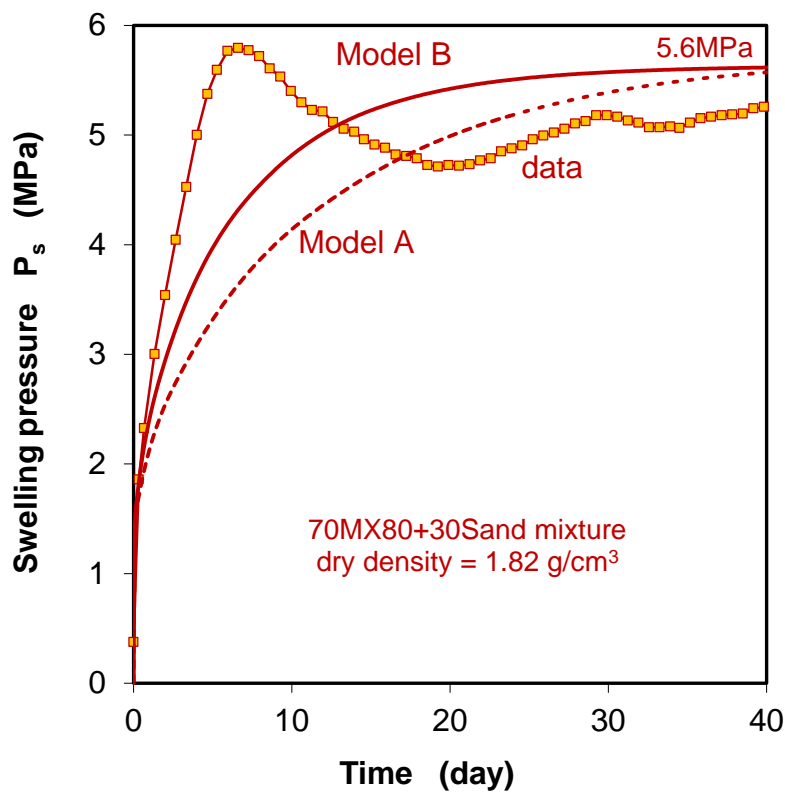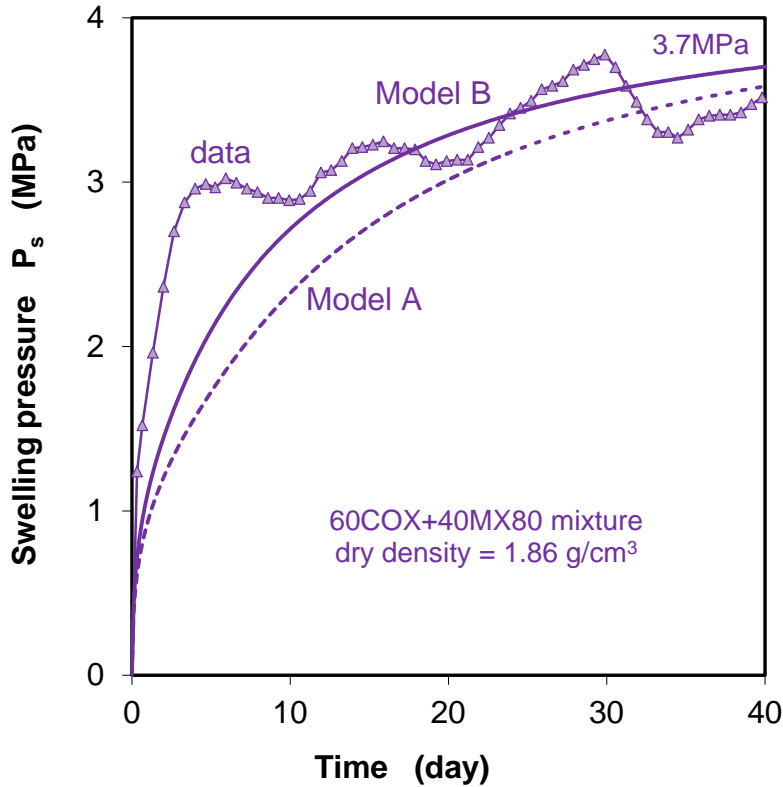
b. Claystone-bentonite mixture

Fig. 5.16   Predictions of the swelling pressure developed in the compacted benton-ite-sand (a) and claystone-bentonite (b) mixture during hydration

5.2.4.2.2 Bentonite

Within the framework of the Bentonite Rock Interaction Experiment (BRIE) in Äspö-URL, water uptake tests were performed on the compacted MX80 bentonite blocks by Clay Technology /ÅKE 13/. The blocks with a dry density = 1.587 g/cm^3 were sized to a height of 100 mm and diameter of 298 mm. A hole of 40 mm was drilled in the centre of each block. The blocks were installed in steel cylinders with steel lids mounted on the top and the bottom. A plastic filter was mounted on the inside of the cylinder for water supply, while the central hole was sealed with a dummy. The cylinder and the top lid were equipped with holes for measurements of total pressure and relative humidity. Fig. 5.17 illustrates schematically the setup of the test and positions of the measurements.
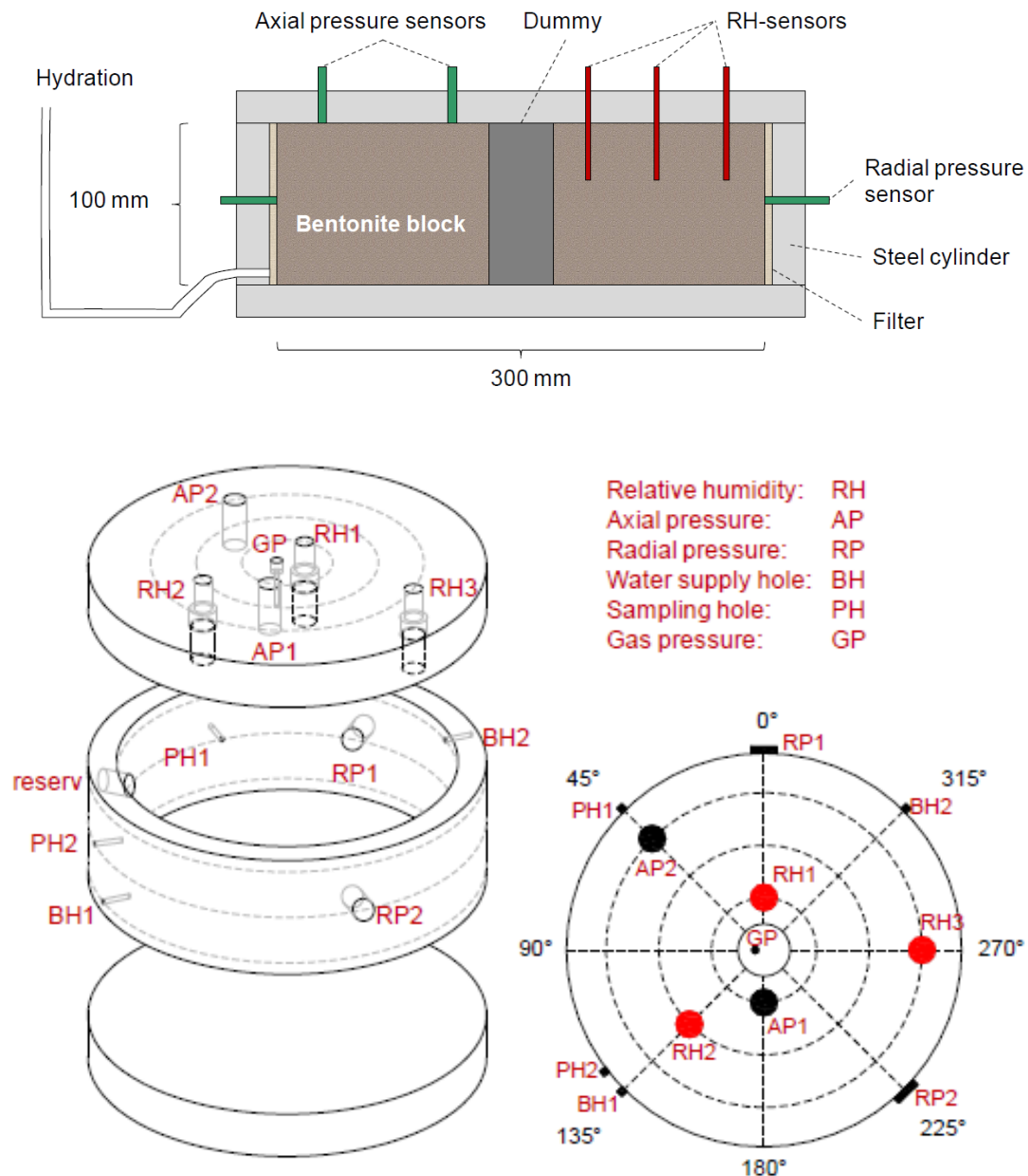
Fig. 5.17   Schematic setup of BRIE water uptake tests on the compacted bentonite
and measurement locations /ÅKE 13/

BRIE-test 1 is selected for modelling the hydration process and the resultant buildup of swelling pressure in the compacted bentonite. An axisymmetric geometry with 120 elements is established for the hollow cylinder, see Fig. 5.18. Considering the initial water filling of the outer slot, the outer diameter of 145 mm is defined for the model. The sample is characterized with a dry density = 1.587 g/cm³, porosity = 44.0 %, water content = 11.75 %, and saturation degree = 42.0 %. The block is fixed with zero boundary deformation. The liquid pressure at the outer boundary is kept at atmospheric level, P_l

$= 0.1$ MPa, and the gas pressure is atmospheric, $P_g = 0.1$ MPa. The rest boundaries are isolated with zero fluid flow, $Q_l = 0$. The initial stress are applied with $\sigma_1 = \sigma_2 = \sigma_3 = 0.15$ MPa. A constant temperature remains at 20 °C. GRS-A, B and BRIE models with the hydraulic parameters are applied (see Table 5.7). However, a unique value of the relative permeability parameter $\lambda = 4$ is obtained from back analysis for all the models. In correspondence to the initial saturation of $S_{lo} = 42.0$ %, an initial suction of $s_o = 95$ MPa is obtained for GRS-A and BRIE model, while $s_o = 290$ MPa for GRS-B. The BBM parameters for the bentonite are adopted (see Table 5.5). Coupled HM calculations are performed by solving the balance equations of solid (Eq. 5.2), water mass (Eq. 5.3) and stress equilibrium (Eq. 5.5).
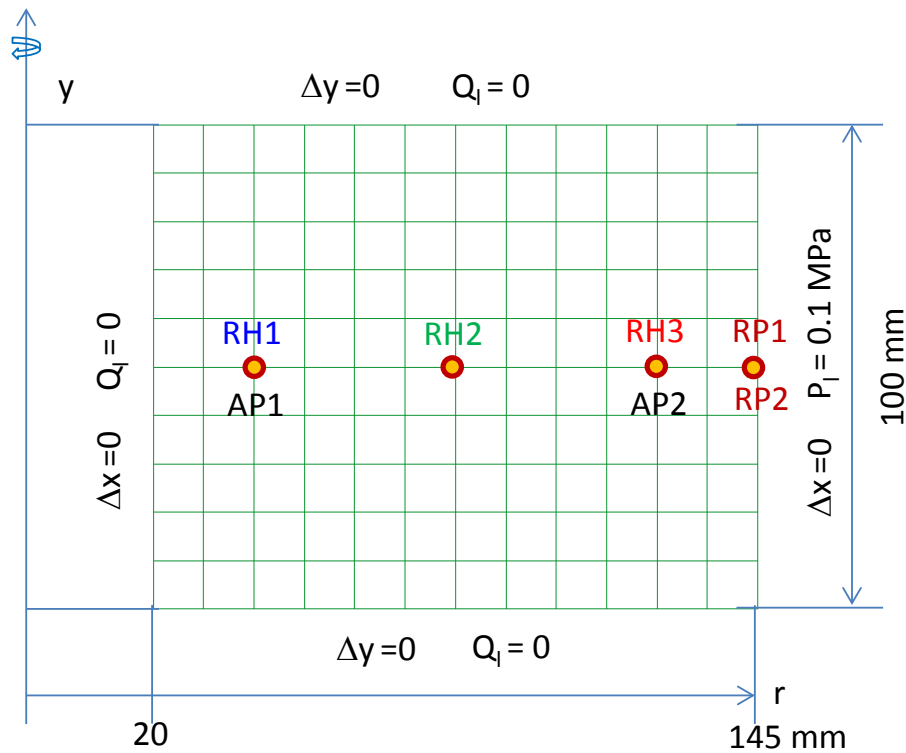
Fig. 5.18 Model geometry and boundary conditions for modelling the hydration and swelling pressure in the compacted bentonite in BRIE-tests

Modelling results are compared with the evolution of measured relative humidity (RH) and total or swelling pressures ($AP,\ RP$) in the sample at the different locations. The distributions of water saturation in the samples after testing at 107 days (test 2) and 203 days (test 1) are also predicted.

From the computing output of the degree of water saturation S_l, one can derive the RH-values by reformulating and combining equations (4.1) and (5.14)

$$RH = exp\left[-\frac{v_{wo}\,\omega_v}{RT} \cdot s\right]$$ (5.29)

with $\quad s = P_o \cdot \left[S_l^{-1/\beta} - 1\right]^{(1-\beta)}$

Fig. 5.19 shows the modelling results of the RH–evolution at the different positions in the sample using the model BRIE (a), GRS-A (b) and GRS-B (c), respectively. It can be recognized that both BRIE and GRS-A models are close to but somewhat overestimate the measured relative humidities, whereas GRS-B model provides much lower RH–values for the first two months but agrees well with the data for the later stages.

The modelling resutls of the distribution of water saturation are illustrated in Fig. 5.20 together with the data at 107 days (test 2) and 203 days (test 1). Whereas BRIE model systematically overestimates (Fig. 5.20a) and GRS-B contrarily underdetermines the water saturation (Fig. 5.20b), GRS-A model deliveres a very close agreement with the distributions of water saturation at those saturation times, see Fig. 5.20a.

Finally, the development of swelling pressure during the water saturation is predicted using the most adequate water retention model GRS-A. Fig. 5.21 shows the modelling results in comparison with the observed buildup of swelling pressure at the different locations. It is obvious that the swelling pressures in radial direction RP at the outer side (r = 0.145 m) and in axial direction at the position r = 0.04 m are well captured by the model. The meaured axial swelling pressures at r = 0.12 m are overestimated by the model, but the calculated axial swelling pressures match the upper curve of the radial swelling pressure. Generally speaking, the hydration process and the resulting swelling pressure in the bentonite can be reasonablly revealed by the coupled HM modelling with GRS-A water retention parameters.
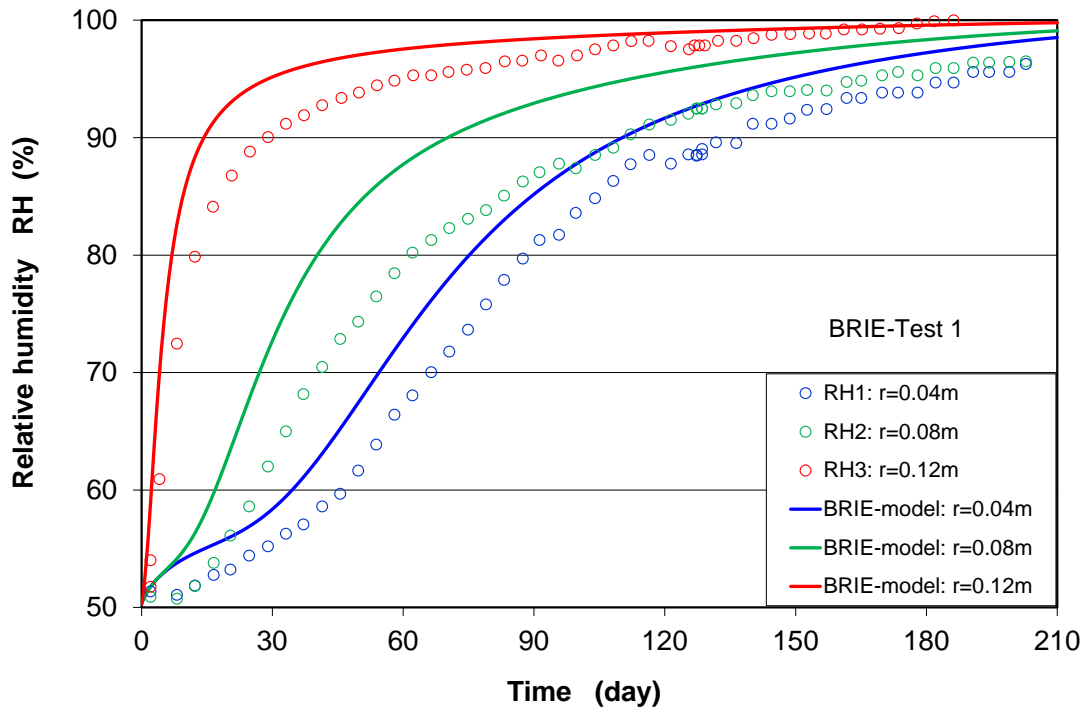
a. Prediction using BRIE model parameters
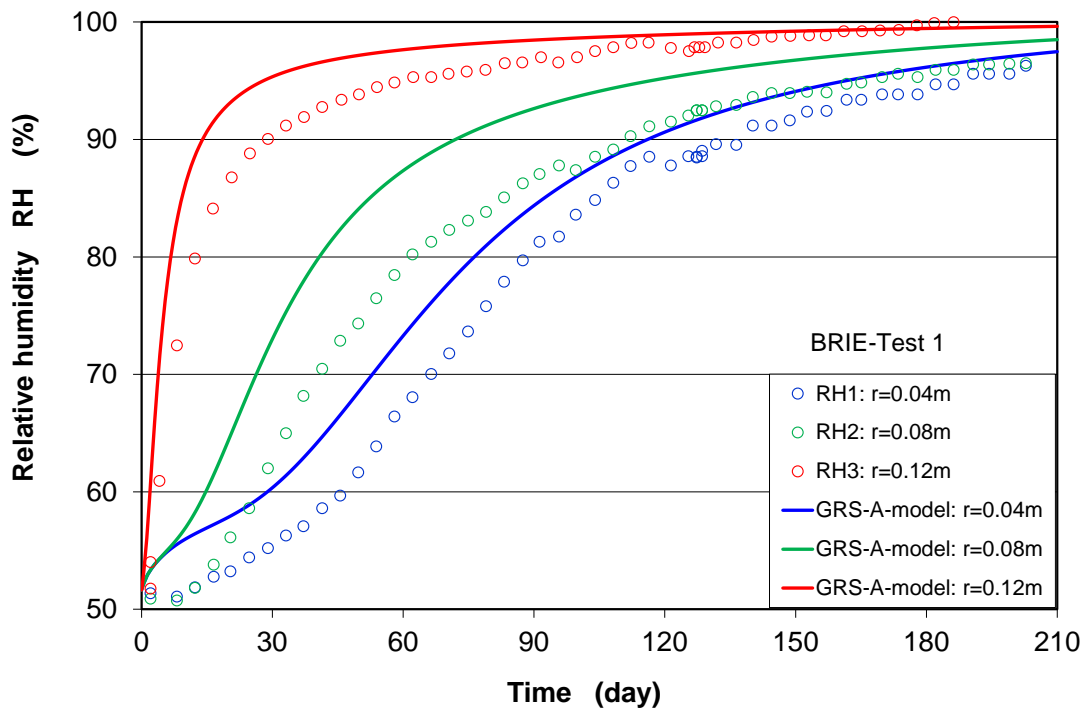
b. Prediction using GRS-A model parameters
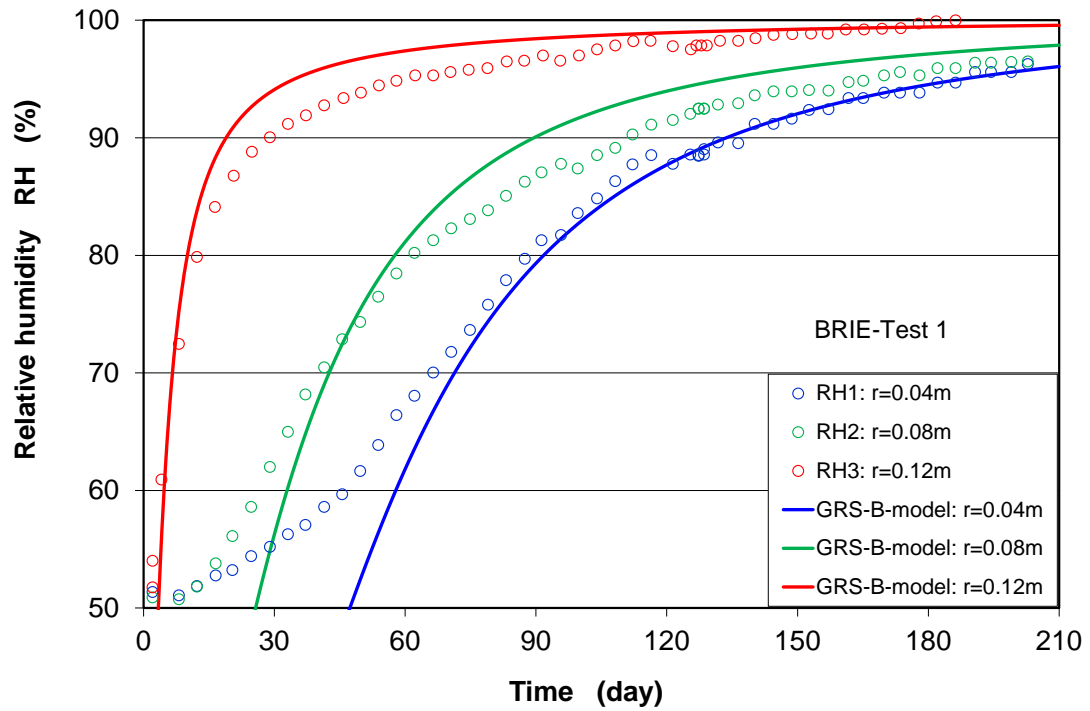
c. Prediction using GRS-B model parameters

Fig. 5.19   Modelled evolution of water saturation of the compacted bentonite at differ-
ent locations during the laboratory BRIE test /ÅKE 13/
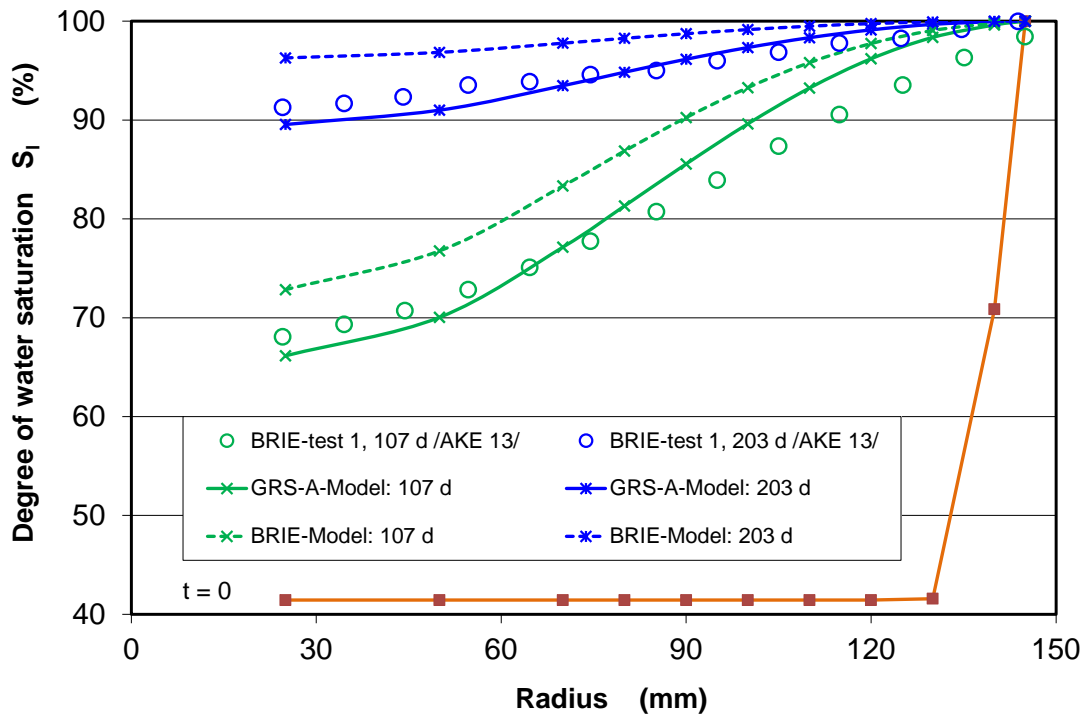
a. Predictions using BRIE and GRS-A model parameters
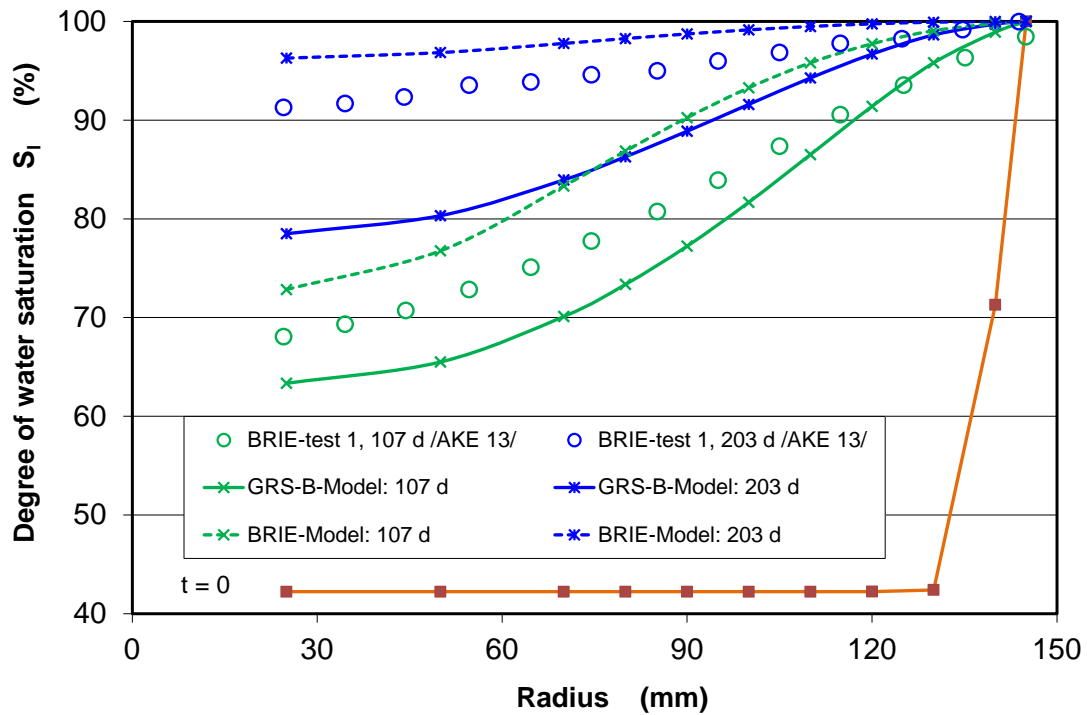
b. Predictions using GRS-A and GRS-B model parameters

Fig. 5.20   Modelled distributions of water saturation in the compacted bentonite at different times during the laboratory BRIE-test /ÅKE 13/
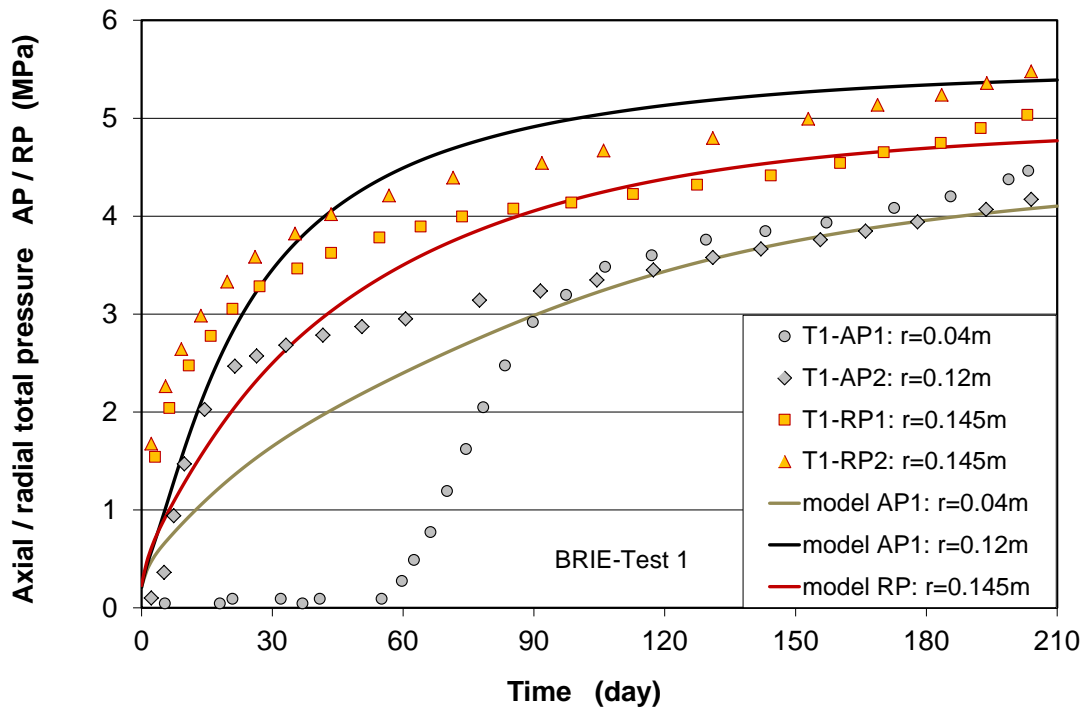
Fig. 5.21   Modelling results of swelling pressure development in the compacted bentonite during the BRIE water uptake test /ÅKE 13/

5.3 Modelling of clay rock

From comprehensive modelling exercises during the last decade, it has been recognized that the existing constitutive models are to be improved for reliable prediction of the long-term performance of the clay host rock during the repository operation and post-closure phases, especially with regard to the time-dependent deformation, permeability variations with damage and recompaction, water conductivity of fractured claystone, and gas migration behaviour. In the framework of this project, it was attempted to establish specific functions for the improvement of the existing models with the following aspects:

- time-dependent deformation of claystone;
- permeability changes during damage and recompaction;
- water permeability of fractured claystone under load; and
- gas migration in water-saturated and fracture-resealed claystone.

The detailed model formulations have been presented in the project reports (THM-TON interim report /ZHA 13a/ and DOPAS deliverables /ZHA 14a/) and publications /ZHA 14b/15a/b/. These constitutive equations will be briefly summarized as follows. They were originally planned to be implemented in CODE-BRIGHT in the framework of the CODE-BRIGHT-Consortium. The implementation work is still undergoing.

5.3.1 Hydraulic constitutive models

The hydraulic laws as adopted for the compacted seal materials (section 5.2.2) may be applied for modelling of the hydraulic behaviour of the clay rock without cracking effects. In case of a clay rock subjected to fracturing due to mechanical loading, for instance, in the EDZ near the underground openings, the permeability increases significantly with fracturing. The cubic law (Eq. 5.9) is no longer adequate for the fracturing-induced permeability. Therefore, it is necessary to develop a new model for that.

5.3.1.1 A permeability model for claystone damage and recompaction

Considering the varying stress conditions subject to the clay rock in the near-field of a potential repository, hydro-mechanical responses of the COX claystone were experi-

mentally investigated with measurements of deformation and gas permeability during damage and recompression /ZHA 13a/15b/. The results are overviewed in chapter 3. The complete behaviour of the claystone before and after failure is schematically highlighted in Fig. 5.22 in terms of differential stress ($\Delta\sigma = \sigma_1 - \sigma_3$), volumetric strain ($\varepsilon_v$), and permeability ($k$) vs. axial strain ($\varepsilon_1$).

The claystone behaves elasto-plastically with volume compaction until the onset of dilatancy at a high stress σ_D. The volume compaction closes up the pores so that the permeability does not increase. Further increasing the stress leads to initiation and propagation of microcracks. As the peak stress σ_B is reached, the microcracks coalesce to a continuous network or shear fracture resulting in a spontaneous increase in permeability. The increased permeability remains relatively constant after the fracture percolation over the post-failure phase. When the minor principle stress σ_3 in the damaged claystone (EDZ) increases ($\Delta\sigma$ decreases), for instance, with the convergent compression of the surrounding rock and the resistance of the backfill, the fractures are going to reclose (ε_v decreases) and the permeability reduces. A high degree (if not full) of the fracture reseal can be expected over long time periods under combined impact of the mechanical load and the moisture-induced swelling of clay into the fracture interstices.

Based on the experimental results, a new model was established for approaching the permeability variations with deformation, damage and recompaction:

$$
k = \begin{cases}
k_c & (\sigma_1 - \sigma_3) < \sigma_B & (5.30a) \\
k_o \cdot exp(-r\sigma_3) \cdot \left(1 - \exp\left(-\frac{\Delta\varepsilon_D}{\varepsilon_B}\right)\right) & \sigma_B \geq (\sigma_1 - \sigma_3) \geq \sigma_R & (5.30b) \\
D \cdot (\Delta\varepsilon_R)^3 & (\sigma_1 - \sigma_3) < \sigma_R & (5.30c)
\end{cases}
$$

During the pre-failure phase, $(\sigma_1 - \sigma_3) < \sigma_B$, the very low permeability of the natural intact claystone does not increase but decreases slightly with volume compaction. For the purpose of simplification, the permeability value can be assumed constant (Eq. 5.30a). As measured, k_c–values of the COX and OPA claystones are in a range of 10^{-20} – 10^{-21} m^2.

Beyond the peak stress during the post-failure phase, $\sigma_B \geq (\sigma_1 - \sigma_3) \geq \sigma_R$, the fracturing-induced permeability increases spontaneously, which is contributed by the connectivity and the conductivity of cracks. It can be expressed with the percolation probability of cracks belonging to the conducting part of a network and the ultimate permeability

112

after fully fracturing (Eq. 5.30b). The percolation probability is expressed as an exponential function of crack dilatancy: $p = (1 - exp(-\Delta\varepsilon_D/\varepsilon_B))$, where $\Delta\varepsilon_D = |\varepsilon_v - \varepsilon_B|$ is the dilatancy with reference to the volumetric strain ε_B at the percolation threshold equal to the peak stress σ_B. The ultimate fracture permeability increases exponentially with decreasing the minor principle stress: $k_f = k_o \cdot exp(-r\sigma_3)$, where k_o is the permeability at zero minor principle stress $\sigma_3 = 0$ and γ is a parameter characterizing the dilatability of the interconnected cracks. The values of the parameters have been estimated to be k_o = $3\cdot10^{-13}$ m^2 and γ = 1.9 MPa^{-1} for the COX claystone. The comparison with the test data in Fig. 3.4 confirms the percolation model.
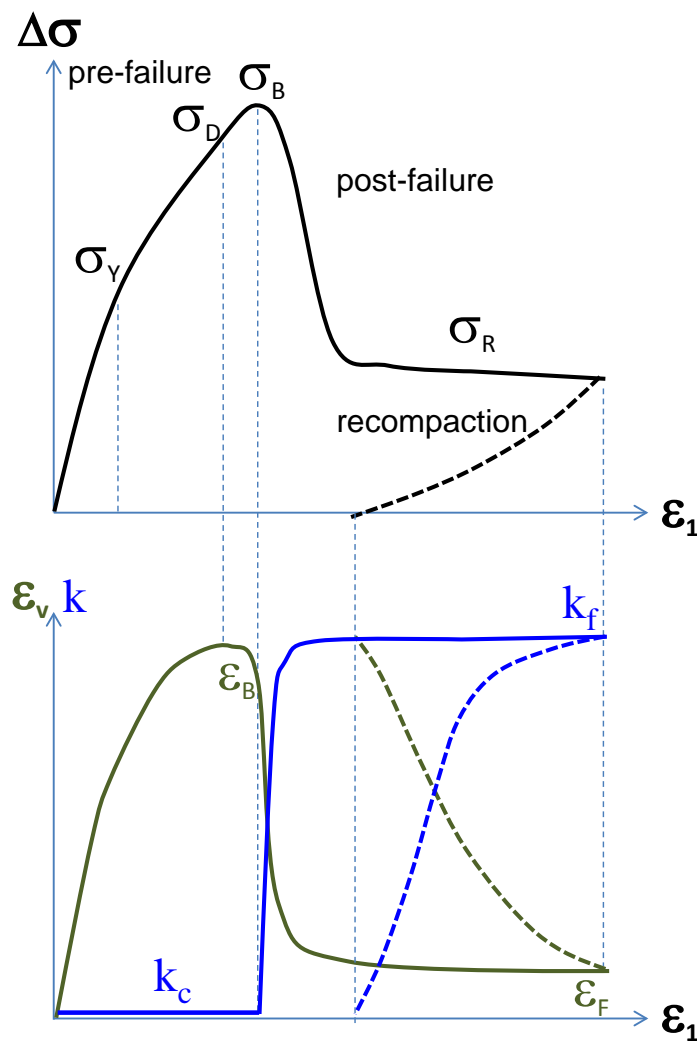

Fig. 5.22   Stress-strain-permeability behaviour of claystone during damage and recompaction (σ_Y = yield stress, σ_D = dilatancy threshold, σ_B/ε_B = peak failure stress/volumetric strain, σ_R = residual strength, k_c = initial permeability, ε_F = volumetric strain at ultimate fracturing and k_f = final fracture permeability)

When the fractured claystone is recompacted with increasing σ_3 to $(\sigma_1 - \sigma_3) < \sigma_R$, the fracture permeability tends to decrease following the cubic law (Eq. 5.30c), where $\Delta\varepsilon_R = |\varepsilon_F - \varepsilon_v|$ represents the residual void in the fractures, ε_F is the maximum dilatancy at the final damaged state and $D = k_f/\varepsilon_F^3$ is a parameter characterising the final damaged state. As the residual fracture void tends to zero, $\Delta\varepsilon_R \to 0$, the fracture permeability disappears. The parameter D has been estimated from the data to lie in a range of $7\cdot10^{-10}$ m^2 to $1\cdot10^{-7}$ m^2, depending on the damage intensity of the claystone. A comparison made in Fig. 3.9 shows a satisfactory agreement of the cubic law with the data obtained from the hydrostatic and deviatoric recompressions.

5.3.1.2   A water conductivity model for fractured claystone

It has to be pointed out that the above mentioned permeability model is based on the gas permeability measurements under mechanical loads. It cannot be directly applied for modelling the water permeability because the significant water-enhanced sealing effects are not taken into account. As observed in our experiments (section 3.4), the water permeability of the fractured claystone is three to seven orders of magnitude lower than the gas permeability. An empirical equation was established for the water permeability of fractured claystone in relation with effective confining stress (Eq. 3.7):

$$K_w = K_{wo} \cdot exp(-\beta \cdot \sigma') \tag{5.31}$$

where $\sigma' = \sigma - p_w$ is the effective stress, σ is the total stress, p_w is the porewater pressure, K_{wo} is the initial water permeability at zero confining stress $\sigma_{eff} = 0$, and β is a parameter characterising the compressibility of the water flow pathways. K_{wo}-values determined on the artificially-fractured COX samples are quite low ranging from 2×10^{-16} to 4×10^{-20} m^2 compared with their gas permeability of $\sim10^{-13}$ m^2. A unique β-value of 0.6 MPa^{-1} is obtained. The model matches the test data well (Fig. 3.12) and therefore can be used for modelling the water permeability of fractured claystone during recompaction.

5.3.1.3   A gas breakthrough model for water-saturated claystone

Gas flow through fractured and water-unsaturated claystone could be modelled by using Darcy's law and the permeability model (equations 5.30b-c). As the fractures be-

come water-saturated, however, gas entry and flow through needs driving forces to overcome the capillary thresholds rebuilt up in the fractures. The gas migration behaviour of the fractured and water-resaturated claystone was investigated and characterised with two key parameters named gas breakthrough pressure and permeability. They are strongly related with the water (intrinsic) permeability of the fractured claystone and external confining stress. Based on the experimental data, the respective relationships were formulated in /ZHA 14b/ and briefly represented below as a gas flow model for fractured and water-resaturated claystone.

The gas breakthrough pressure can be expressed as function of intrinsic permeability and minor confining stress (Eq. 3.8)

$$P_b = B \cdot (K_o)^{-1/n} \cdot exp(-\gamma\sigma_3) \tag{5.31}$$

where P_b is the gas breakthrough pressure, K_{wo} is the initial intrinsic permeability at zero minor confining stress $\sigma_3 = 0$, B, n and γ are parameters. Their values have been estimated to be $B = 2\times10^{-7}$ MPa·m$^{2/3}$, $n = 3$ and $\gamma = 0.2$ MPa^{-1} for the fractured claystone with very low water permeabilities of $K_o = 5\times10^{-19}$ to 5×10^{-20} m^2. The model prediction provides a reasonable agreement with the data (Fig. 3.15). Obviously, the gas breakthrough pressures are below the conservative fracturing condition by neglecting the tensile strength, $P_b < \sigma_3$. This model may also be applicable for the intact claystone with lower permeabilities of $K_o < 1\times10^{-20}$ m^2.

Gas pressure rising reopens some weakly-resealed fissures as well as dilate the gas-occupied pathways. The growth of the fissure networks allows gas to flow easier, so that the effective gas permeability increases as shown in Fig. 3.16. The gas breakthrough permeability can be expressed as a function of gas pressure P_b:

$$K_g = K_{go} \cdot exp[\omega(P_b - P_{bo})] \tag{5.32}$$

where K_{go} is the gas permeability at the initial breakthrough pressure P_{bo}, ω is the parameters characterising the dilatability and interconnectivity of the gas pathways. Fitting the data leads to $\omega = 1.5$ to 2.5 MPa^{-1}.

Actually, the dilation of the pathways and the resulting permeability increase is determined by the effective confining stress, namely the difference between the total stress

and pore pressure. Therefore, the gas breakthrough permeability can be related to the minor effective principal stress σ_3'

$$K_g = K_{go} \cdot exp(-\mu\sigma_3') \tag{5.33}$$

where $\sigma_3' = \sigma_3 - p_g = \sigma_3 - (p_i + p_o)/2$, p_i, p_o and p_g are the upstream, downstream and mean gas pressure, respectively, K_{go} is the gas permeability at $\sigma_3' = 0$, and η is a parameter characterising the dilatability and interconnectivity of the gas pathways. Fitting the data yields varying K_{go} values of 1×10^{-10} up to 3×10^{-7} m^2 but a unique value of $\eta = 3.5$ MPa^{-1}.

5.3.2   Mechanical constitutive models

An elastoplastic damage model was originally developed by /VAU 03/ for description of the mechanical behaviour of clay rock. This model considers the claystone as a composite material composed of a clay matrix connected by bonds. The clay matrix behaves like a typical elastoplastic soil, while the bonds (mainly carbonates) behave like a typical quasi-brittle material that can be represented by a damage elastic law. The stress-strain behaviour of the composite material is assumed to be determined by coupling both responses of matrix and bonds under compatible conditions.

However, the micro-structure observations made on the relatively clay-rich COX and OPA claystones /AND 05/and /BOC 10/ showed that the hard mineral grains (quartz, calicite and others) are embedded in the clay matrix and the connections between neighbouring clay particles are mainly through adsorbed porewater. The effects of the solid-bonds should not be significant. So the behaviour of the clay matrix is dominating. Currently, this model has been enhanced by introducing a modified Lemaitre law for the viscoplastic deformation of claystone /RUI 15/. This so called visco-elastoplastic model is briefly described as follows.

The visco-elastoplastic model is formulated for unsaturated claystone. The Mohr-Coulomb criterion is adopted for yield surface in the stress space that separates the elastic and plastic parts of the mechanical response.

Elastic law:
$$d\sigma_{ij} = D_{ijkl}^e \left(d\varepsilon_{kl} - \delta_{kl} \frac{ds}{K_s} - d\varepsilon_{kl}^{vp} \right) \tag{5.34}$$

where σ_{ij} = effective stresses

ε_{kl} = total strains

ε_{kl}^{vp} = viscoplastic strains

D_{ijkl}^e = elastic stiffness matrix

K_s = bulk modulus against suction change ds ($s = p_g - p_l$)

δ_{kl} = Kronecker delta.

For the simplicity, the claystone is here assumed to be isotropic. The linear elastic stiffness D_{ijkl}^e is determined by Young's modulus E and Poisson's ratio ν of the claystone. Volumetric swelling of the claystone is assumed to be linearly related to suction change ds by the bulk modulus K_s. Wetting (suction decrease) leads to swelling and in contrast drying (suction increase) results in shrinkage:

$$d\varepsilon_v^s = \frac{ds}{K_s} \tag{5.35}$$

Mohr-Coulomb yield function:

$$F = \left(\cos\theta + \frac{1}{\sqrt{3}}\sin\theta \cdot \sin\varphi \right) J - \sin\varphi \cdot (c\cot\varphi + p) \geq 0 \tag{5.36}$$

where θ is Lode's angle (Eq. 5.20), φ is the friction angle, c is the cohesion, which depends on suction following the law: $c(s) = c_o + s \cdot \tan\varphi$, and $p_t = c \cdot \cot\varphi$ is the isostatic tensile strength.

Plastic potential:

$$G = \left(\cos\theta + \frac{1}{\sqrt{3}}\sin\theta \cdot \sin\varphi \right) J - \omega \cdot \sin\varphi \cdot (p + p_t) \tag{5.37}$$

where ω is a parameter defining the non-associativity of the plastic flow: $\omega = 1$ when associated and $\omega = 0$ for zero dilatancy.

<u>Hardening-softening law</u>:

An isotropic hardening-softening law is considered, governed by the evolution of the strength parameters (φ, c). The equivalent plastic deformation is the selected state variable to control this evolution, which is defined as:

$$\varepsilon_{eq}^p = \left(\frac{2}{3} \boldsymbol{\varepsilon}^p : \boldsymbol{\varepsilon}^p\right)^{1/2} \tag{5.38}$$

where $\boldsymbol{\varepsilon}^p$ is the plastic deformation tensor.

The way in which the angle of friction varies depends on the equivalent plastic deformation, as outlined in Fig. 5.23. The laws of evolution in each one of the listed areas are shown in Table 5.11. Cohesion evolves as a function of the mobilized friction angle and at any point is given by the following expression: $c_{mov} = c_{peak} \cdot \cot \varphi_{ini} \cdot \tan \varphi_{mov}$.
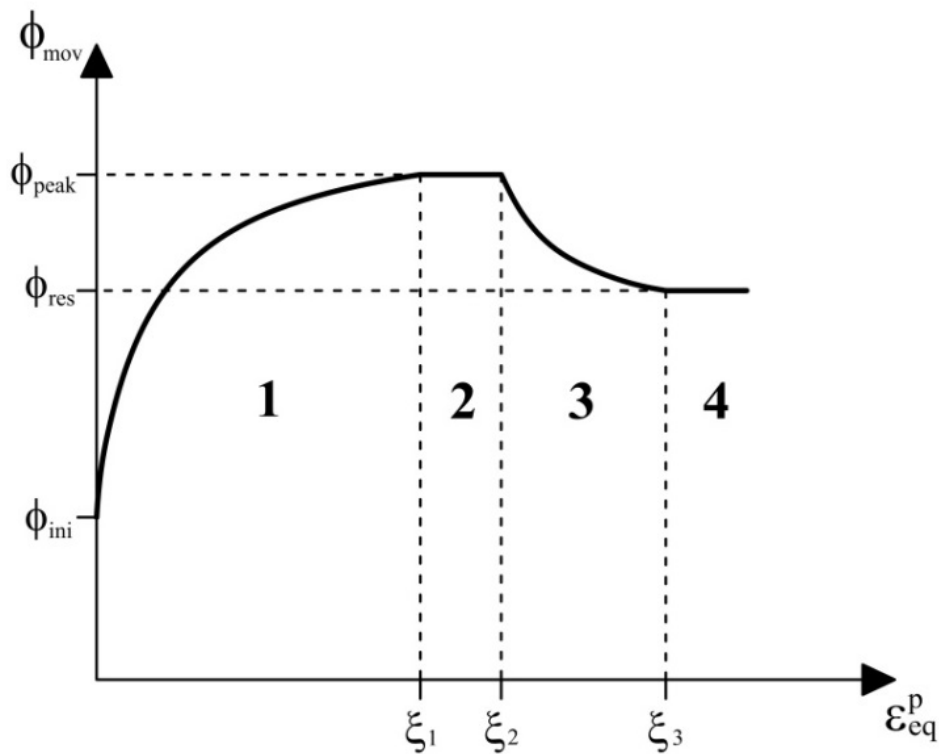

Fig. 5.23   Evolution of the friction angle

Table 5.11   Laws of evolution of the friction angle

Zone 1	$\varphi_{mov} = \varphi_{ini} + \dfrac{\varepsilon_{eq}^p}{a_{hard} + \dfrac{\varepsilon_{eq}^p}{\Delta\varphi_{hard}}}, \quad \Delta\varphi_{hard} = \dfrac{\xi_1}{\dfrac{\xi_1}{\varphi_{peak} - \varphi_{ini}} - a_{hard}}$
Zone 2	$\varphi_{mov} = \varphi_{peak}$
Zone 3	$\varphi_{mov} = \varphi_{peak} - \dfrac{\varepsilon_{eq}^p - \xi_2}{a_{soft} + \dfrac{\varepsilon_{eq}^p - \xi_2}{\Delta\varphi_{soft}}}, \quad \Delta\varphi_{soft} = \dfrac{\xi_3 - \xi_2}{\dfrac{\xi_3 - \xi_2}{\varphi_{peak} - \varphi_{res}} - a_{soft}}$
Zone 4	$\varphi_{mov} = \varphi_{res}$

φ_{mov} = mobilized friction angle, φ_{ini} = initial friction angle at yield surface, φ_{peak} = peak friction angle at peak failure strength, φ_{res} = residual friction angle at residual strength, ξ_1 = equivalent plastic strain at which the maximum strength is reached, ξ_2 = equivalent plastic strain at which softening begins, ξ_3 = equivalent plastic strain at which the residual strength is reached, α_{hard} = constant that controls the curvature of the function in the hardening branch, α_{soft} = constant that controls the curvature of the function in the softening branch.

Creep law

For description of the creep deformation of claystone, a modified Lemaitre law is adopted taking into account strain-hardening effect. The strain rate is expressed as function of deviatoric stress and equivalent plastic strain

$$\dot{\boldsymbol{\varepsilon}}^{vp} = \frac{2}{3} \frac{\dot{\varepsilon}_{eq}^{vp}}{q} \mathbf{s} \tag{5.39}$$

$$\dot{\varepsilon}^{vp} = \gamma (q - \sigma_s)^n (1 - \varepsilon_{eq}^{vp})^m \tag{5.40}$$

where γ is a parameter of viscosity, σ_s is a threshold of the deviatoric stress from which the viscoplastic deformation is activated, n and m are material constants and ε_{eq}^{vp} is the state variable of the viscoplastic response, defined as:

$$\varepsilon_{eq}^{vp} = \int\limits_{o}^{t} \left(\frac{2}{3} \dot{\boldsymbol{\varepsilon}}^{vp} : \dot{\boldsymbol{\varepsilon}}^{vp} \right)^{1/2} dt \tag{5.41}$$

The long-term creep experiments performed on the claystone /ZHA 13a/15a/ showed that the typical creep strain curve can be divided into three sequential stages, transient creep with decreasing rates, stationary creep with a constant rate, and tertiary creep with increasing rate to failure. The modified Lemaitre law features the transient creep with rate decrease. Taking $\varepsilon_{eq}^{vp} = 0$, this model may also be suitable for description of the stationary creep.

Based on the long-term creep test data, a model was formulated for the stationary creep of the claystone by modification of the Mitchell law /MIT 92/ that had been derived through thermodynamically analysis of soil flow by application of absolute reaction rate theory

$$\dot{\varepsilon}^{vp} = A \, \exp\left(-\frac{Q}{RT}\right) \sinh(\alpha \cdot q) \tag{5.42}$$

where T is the absolute temperature (K), R is the universal gas constant ($8.32 \cdot 10^{-3}$ kJmol^{-1}K^{-1}), Q is the apparent activation energy (kJmol^{-1}), A is a parameter in s^{-1}, and α is a parameter in MPa^{-1}.

If $\alpha q < 1$, then $\sinh(\alpha q) \approx \alpha q$, and the strain rate is directly proportional to q

$$\dot{\varepsilon}^{vp} = A \, \exp\left(-\frac{Q}{RT}\right)(\alpha \cdot q) \tag{5.43}$$

This is the case for ordinary Newtonian fluid flow and diffusion. According to /RUT 93/, the linear stress/strain rate relation implicates that the viscoplastic deformation of the saturated claystone is controlled by diffusive mass transfer or pressure solution processes in interfaces between grains.

For most deformation problems of soils and rocks, $\alpha q > 1$, so then $\sinh(\alpha q) \approx 1/2 \exp(\alpha q)$, and equation (5.42) becomes

$$\dot{\varepsilon}^{vp} = \frac{A}{2} \exp\left(-\frac{Q}{RT}\right) \exp(\alpha \cdot q) \tag{5.44}$$

It is considerable to incorporate the stationary creep model into the code for prediction of the long-term deformation of clay host rock during the repository post-closure phase.

5.3.2.1 Mechanical parameters

Elastic parameters

In the framework of an ANDRA/GRS joint programme /ZHA 15c/ for investigation of the anisotropic behaviour of the COX claystone, the elastic parameters were determined in directions parallel and perpendicular to the bedding planes. Fig. 5.24 shows the averaged Young's modulus E_1 / Poisson's ratio v_1 parallel to bedding and E_2 / v_2 normal to bedding as a function of deviatoric stress at radial stress of 5 MPa. The elastic parameters increase in the beginning of $\Delta\sigma$ < 10 MPa due to hardening effect and then tend to constant until peak failure. The constant values shall be representative for the intact claystone, while the low values may be for the disturbed state. The five independent elastic parameters and the anisotropic parameters are summarized in Table 5.12 and compared with the OPA clay /BOC 10/ and the Tournemire shale /NIA 97/. One can identify that the elastic stiffness of the COX clay rock is higher than that of the Opalinus clay but lower than the Tournemire shale. The elastic anisotropy of the COX clay rock is less significant compared with the other two clay rocks.
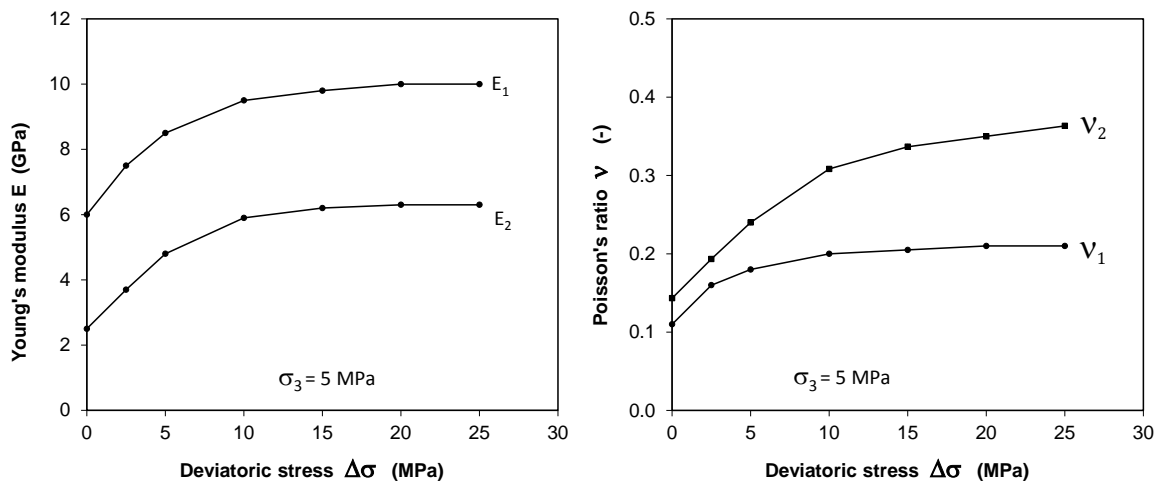

Fig. 5.24   Anisotropic elastic parameters of the COX claystone as a function of deviatoric stress: Young's modulus / Poisson's ratio E_1 / v_1 parallel and E_2 / v_2 normal to bedding planes

Table 5.12   Anisotropic elastic parameters of three clay rocks

Clay rock	E_1 (GPa)	E_2 (GPa)	G_2 (GPa)	ν_1	ν_2	$R_E=E_1/E_2$	$R_\nu=\nu_2/\nu_1$
COX Bure-490m /ZHA 15c/	10.0	6.3	5.0	0.21	0.35	1.6	1.7
OPA, Mont-Terri /BOC 10/	10.0	4.0	3.5	0.25	0.35	2.5	1.4
Tournemire /NIA 97/	30.0	10.0	5.0	0.15	0.30	3.0	2.0

Neglecting the anisotropy, the isotropic elastic parameters can be obtained:

$$E = \frac{2E1 + E2}{3}; \ \ v = \frac{2v1 + v2}{3}; \ \ G = \frac{E}{2(1 + 2v)}; \ \ K = \frac{E}{3(1 - 2v)} \qquad (5.45)$$

where E = Young's modulus, v = Poisson's ratio, K = bulk modulus, and G = shear modulus. The calculated data for the COX claystone are summarized in Table 5.13 and illustrated in Fig. 5.25.

Table 5.13   Isotropic elastic parameters of COX claystone at radial stress of 5 MPa

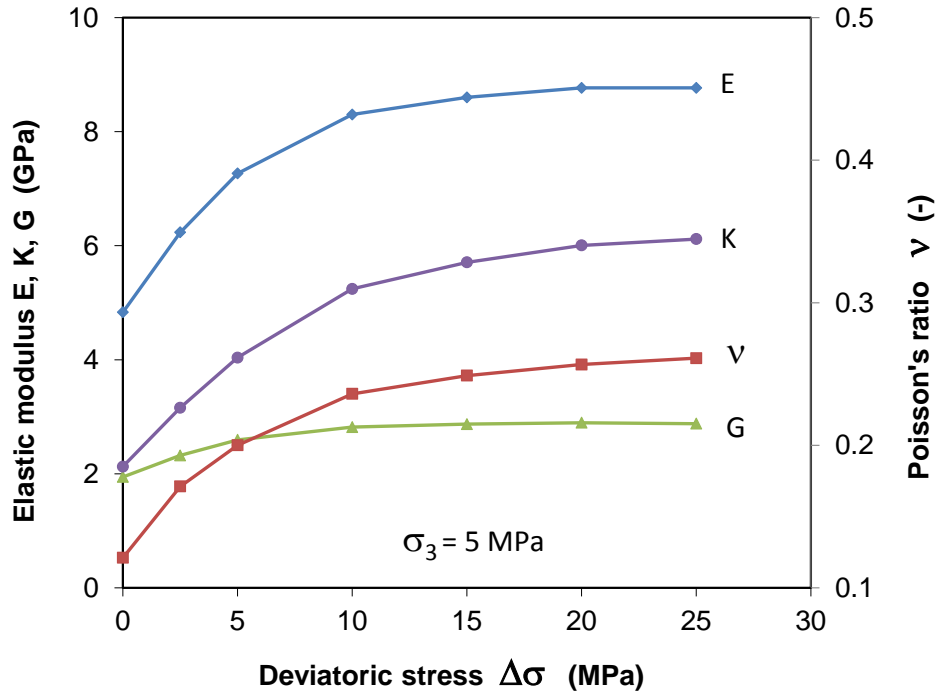| $\Delta\sigma$ (MPa)	E (GPa)	ν	G (GPa)	K (GPa)
0	4.83	0.12	1.95	2.13
2.5	6.23	0.17	2.32	3.16
5	7.27	0.20	2.60	4.04
10	8.30	0.24	2.82	5.24
15	8.60	0.25	2.87	5.71
20	8.80	0.26	2.90	6.00
25	8.80	0.26	2.88	6.12

Fig. 5.25 Isotropic elastic parameters of the COX claystone as a function of devia-
toric stress

Swelling parameters

The swelling and shrinking of the claystone is assumed to be linearly related with suc-
tion (Eq. 5.35). The swelling bulk modulus K_s is estimated on the basis of the test data
as shown in Fig. 5.26. The COX and OPA samples were dried at a low humidity of RH
= 23 % (suction s = 206 MPa) and then wetted with vapour at RH = 100 % (s = 0). The
volume expansion from the wetting part up to the full saturation (s = 206 MPa → 0) was
measured to $d\varepsilon_v$ ≈ 1.5 % yielding K_s ≈ 14 GPa. The free swelling after water saturation
has to be considered for the complete swelling behaviour of the claystone in the future.

Yield parameters

The yield parameters in (Eq. 5.36) are determined from the triaxial compression tests
($\theta = -\pi/6$) for the COX claystone: c = 2.5 MPa and φ = 26°. Fig. 5.27 compares the
yield boundary with the measured data for the COX claystone. Beyond the yield limit,
further load leads to initiation and growth of microcracks until the peak failure. The evo-
lution of the stress-strain is modelled through hardening plasticity. The peak strength
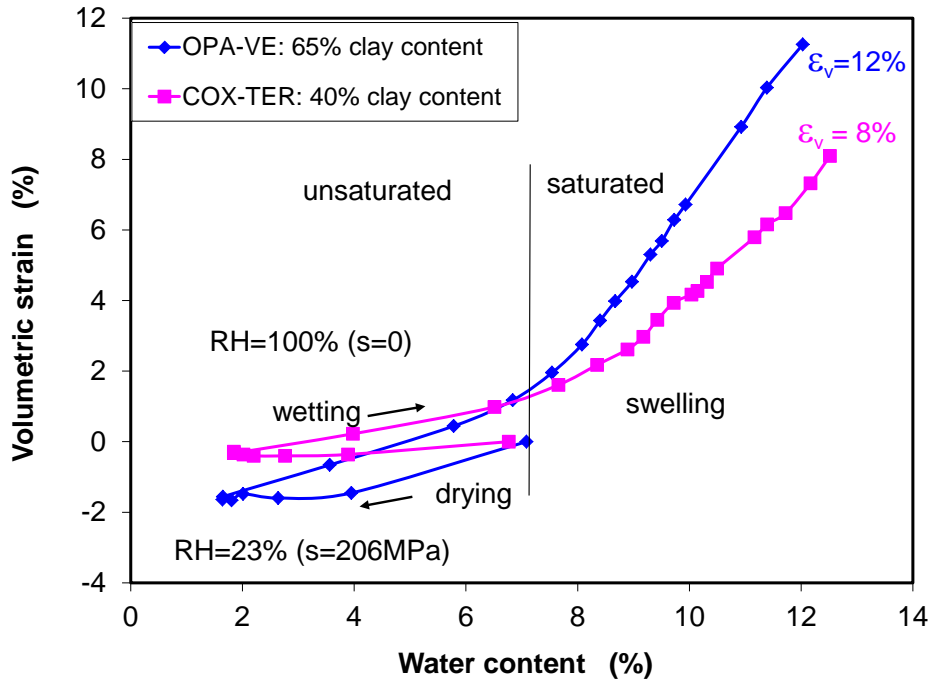parameters are determined to c = 6 MPa and φ = 26°.

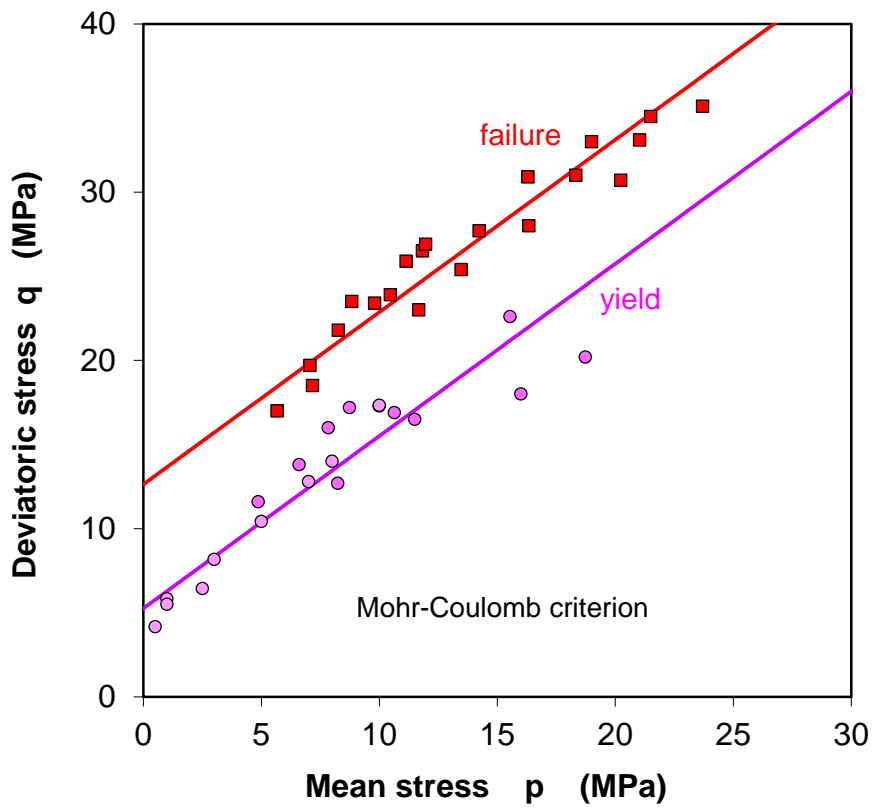Fig. 5.26   Swelling and shrinkage of the COX and OPA claystones as a function of water content

Fig. 5.27   Yield and peak failure boundaries of the COX claystone

The creep parameters in equation (5.42) for the stationary creep of the claystone have been established: $R = 8.32 \cdot 10^{-3}$ kJmol^{-1}K^{-1}, $Q = 45$ kJmol^{-1}, $A = 2.5 \cdot 10^{-4}$ s^{-1}, $\alpha = 0.2$ MPa^{-1}. Fig. 5.28 shows the comparison of this hyperbolic model with the creep rates as a function of deviatoric stress. Taking the creep threshold $\sigma_s = 2.0$ MPa and $\varepsilon_{eq}^{vp} = 0$, fitting the data yields the parameters of the Lemaitre power law (Eq. 5.40): $\gamma = 4.5 \cdot 10^{-9}$ d^{-1}, $n = 2.5$ and $m = 530$.
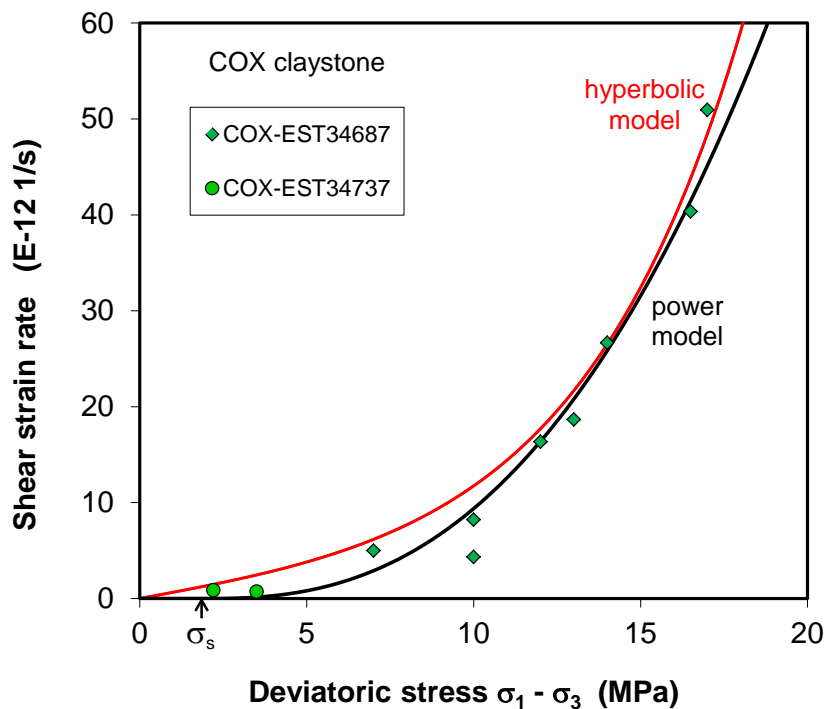
Fig. 5.28   Creep models for the stationary creep of the COX claystones

5.3.3   Simulations of short- and long-term deformation

The short- and long-term deformation behaviour of the COX claystone are simulated by HM coupling calculations using the visco-elastoplastic model for the mechanical behaviour and the relevant hydraulic laws for the response of pore pressure. The mechanical parameters are partly determined above based on the test data and partly through back calculations, depending on individual samples because of the different properties. However, the same hydraulic parameters are adopted for all the samples and given in Table 5.13.

Table 5.13 Key hydraulic parameters obtained for modelling the COX claystone

Permeability-porosity relation	$k = k_o \cdot \dfrac{\phi^3}{(1-\phi)^2} \cdot \dfrac{(1-\phi_0)^2}{\phi_0^3}$; $\phi_o = 0.17$, $k_o = 1\cdot10^{-20}$ m^2
Relative permeability	$k_{rl} = A \cdot S_l^\lambda$; $k_{rg} = 1 - k_{rl}$; $A = 1$, $\lambda = 5$
Water retention curve	$S_l = \left[1 + (s/P_o)^{\frac{1}{1-\beta}}\right]^{-\beta}$; $P_o = 20$ MPa, $\beta = 0.35$

5.3.3.1 Short-term deformation

A series of triaxial compression tests presented in /ZHA 13a/ are simulated by solving the balance equations of solid (Eq. 5.2), water mass (Eq. 5.3) and stress equilibrium (Eq. 5.5). The initial properties of the samples are characterized by a porosity of 17 %, water content of 6.5 % and saturation degree of 90 %. The corresponding suction is determined to s_o = 10 MPa. The cylindrical samples of 70 mm diameter and 140 mm length were loaded at an axial strain rate of 10^{-6} s^{-1} under different lateral stresses of 0 to 12 MPa to the peak stress and beyond that to the residual strength. The drained conditions are applied by keeping atmospheric pressure at both end faces, $P_l = P_g = 0.1$ MPa. The circumference surface is isolated against fluid, $Q_l = 0$. The cylindrical samples are represented by a 3D cubic body (Fig. 5.29).
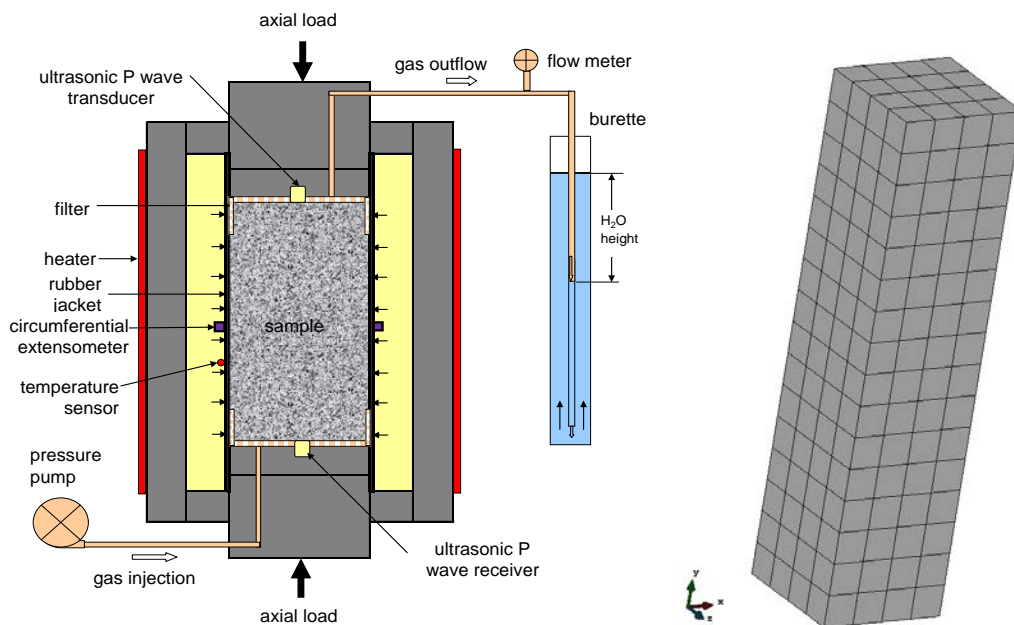

Fig. 5.29 3D model geometry for modelling the triaxial tests

In the calculations, the Biot effective stress concept is applied: $p^b = p^t - Bp^l$, where p^t is the total mean stress, p^l is the porewater pressure and p^b is the effective stress. The mechanical parameters used are summarized in Table 5.14.

Table 5.14   Mechanical parameters adopted for modelling the short-term deformation behaviour of the COX claystone

Biot stress parameter	$p^b = p - Bp^l$: $B = 0.6$
Elastic modulus (Eq. 5.34)	$E = 6.3$ GPa, $\nu = 0.2$, $K_s = 1E7$ MPa
Yield parameters (Eq. 5.36/37)	$c = 6$ MPa, $\varphi = 26°$, $\varpi = 0.1$, $\theta = 25°$
Hardening-softening parameters (Table 5.11)	$\beta^{ini} = \varphi_{ini} / \varphi_{peak} = 0.42$, $\alpha_{hard} = 0.0035$ $\beta^{res} = \varphi_{ires} / \varphi_{peak} = 0.8$, $\alpha_{soft} = 0.07$ $\xi_1 = 0.001\sigma_3 + 0.001$, $\xi_2 = 0.001\sigma_3 + 0.002$ $\xi_3 = 0.001\sigma_3 + 0.012$
Creep parameters (Eq. 5.40)	$\sigma_s = 2$ MPa, $\varepsilon_{eq}^{vp} = 0$, $\gamma = 4.5 \cdot 10^{-9}$ d^{-1}, $n = 2.5$, $m = 530$

Modelling results are illustrated in Fig. 5.30 together with the test data. It is obvious that the elastoplastic response with hardening and softening effects can be reasonably represented by the model. The model shows the volumetric compression until the peak stress and then the following dilatancy progressing during the softening phase. There are some quantitative discrepancies between the calculated and measured volumetric strains. It is also to be pointed out that the equivalent plastic strain parameters ξ_1, ξ_2, ξ_3 are not constant but vary with the confining stress σ_3. This is due to the increased ductility of the claystone at high confining stresses. In the calculations, the plastic strain parameters are preliminarily assumed to be linearly related with the confining stress as shown in Fig. 5.31 and Table 5.14. Obviously, this assumption provides the sound modelling results. These equations shall be implemented in the code.
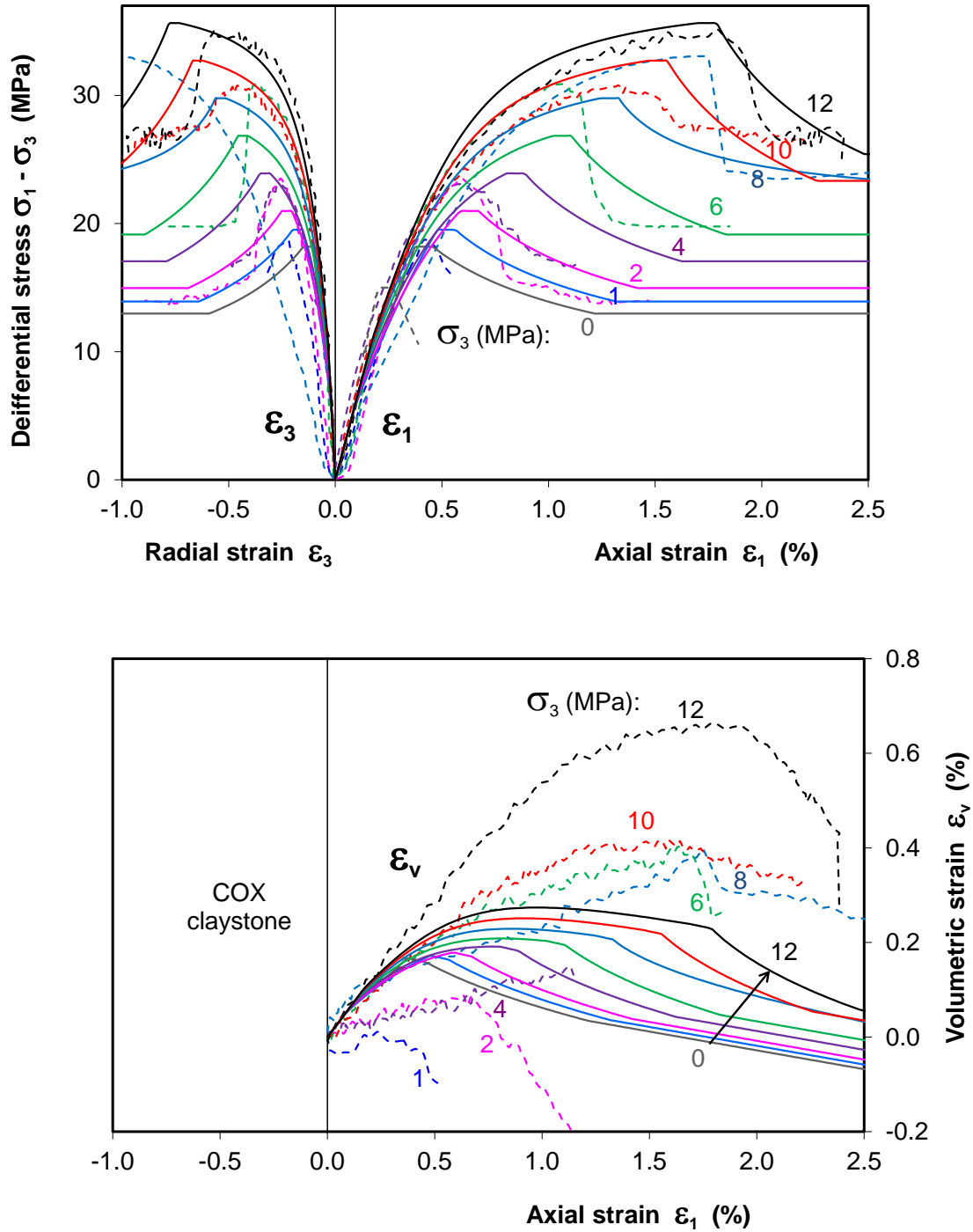
Fig. 5.30 Modelling results of the short-term deformation behaviour of the COX clay-
stone during triaxial loading
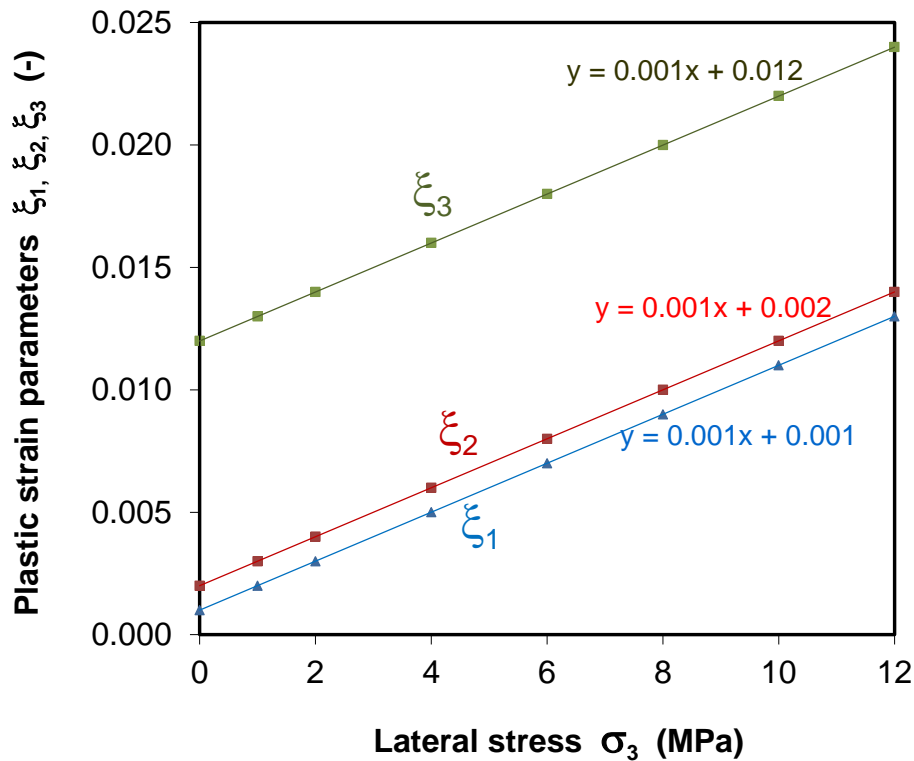
Fig. 5.31   Plastic strain parameters as function of the minor confining stress

5.3.3.2   Long-term deformation

The long-term deformation behavior of the claystone was investigated in triaxial creep tests. One of them was performed on a COX sample EST34678 with a porosity of 15 % and water saturation degree of 97 %. The corresponding suction is determined to $s_o = 5$ MPa. The cylindrical sample of 100 mm diameter and 190 mm length is represented by a 3D cubic body (Fig. 5.29). The drained conditions are applied by keeping atmospheric pressure at both end faces, $P_l = P_g = 0.1$ MPa. The circumference surface is isolated against fluid, $Q_l = 0$. The creep test was performed in three phases under different triaxial loads.

Fig. 5.32a shows the evolution of applied stresses. During the first phase at axial stress $\sigma_1 = 15$ MPa, the lateral stress σ_3 was stepwise reduced down to 5, 3, 2, 1 and 0.5 MPa. In the second phase, the lateral stress of 0.5 MPa maintained and the axial stress was increased up to 17, 17.5 and 18.5. The third phase was carried out by increasing the lateral stress up to 1, 2 and 3 MPa under constant $\sigma_1 = 18.5$ MPa. The test is simulated by solving the balance equations of solid (Eq. 5.2), water mass (Eq.

5.3) and stress equilibrium (Eq. 5.5). The parameter values used in the modelling of the short-term deformation above (Table 5.14) are adopted for modelling the long-term deformation. Moreover, sensibility of some parameters is examined in the simulation of the creep test, such as the Young's modulus E and plastic strain parameters ξ_1, ξ_2, ξ_3. All the parameters are listed in Table 5.15.

Table 5.15   Mechanical parameters for modelling the short-term deformation behaviour of the COX claystone

Biot stress parameter	$p^b = p - Bp^l$: $B = 0.6$
Creep parameters	$\sigma_s = 2.0$ MPa, $\varepsilon_{eq}^{vp} = 0$, $\gamma = 4.5 \cdot 10^{-9}\,\mathrm{d}^{-1}$, $n = 2.5$, $m = 530$
Elastic parameters	$\nu = 0.25$, $K_s = 1\mathrm{E}7$ MPa
Hardening-softening parameters	$\beta^{ini} = \varphi_{ini} / \varphi_{peak} = 0.42$, $\alpha_{hard} = 0.0035$ $\beta^{res} = \varphi_{ires} / \varphi_{peak} = 0.8$, $\alpha_{soft} = 0.07$
Model	Varying parameters
A	$E = 6.3\ GPa$, $\xi_1 = 0.0015$, $\xi_2 = 0.003$, $\xi_3 = 0.012$
B	$E = 8.8\ GPa$, $\xi_1 = 0.003$, $\xi_2 = 0.004$, $\xi_3 = 0.014$
C	$E = 88\ GPa$, $\xi_1 = 0.0015$, $\xi_2 = 0.003$, $\xi_3 = 0.012$

Fig. 5.32b compares the calculated strains with the measured data. Model A uses the same parameters as in the simulation of the short-term tests, resulting in relatively large deformation. Model B takes relatively large E–value of 8.8 GPa and plastic strains, providing slightly larger strains for the first and second phases compared to that of Model A. Taking a very large E–value of 88 GPa and smaller plastic strain parameters, Model C produces the strain curves more close to the measured ones. This indicates the extremely high stiffness of this sample. For the most samples, the parameters of Model B seem to be more adequate.

The calculated creep strains for each step are almost in steady state because the applied very large m–value of 530 limits the strain hardening effect. The slope of the creep curve or creep rate is more comparable with the last part of each creep step. However, the creep rates during the third phase under increased lateral stresses are overestimated by the models. The dependency of the creep on the loading path has to be examined further.
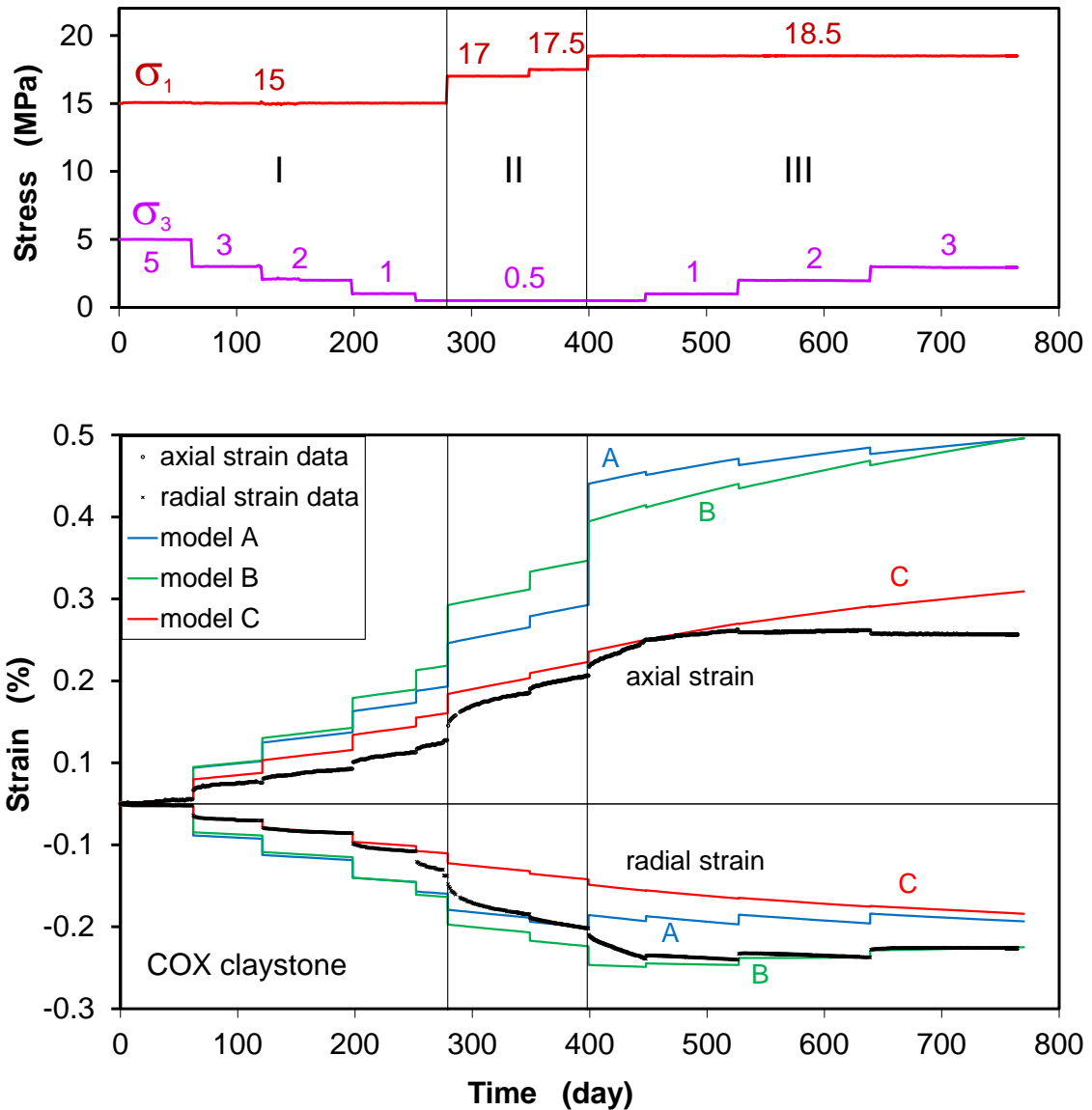
Fig. 5.32   Modelling results of the long-term deformation behaviour observed during a triaxial creep test on COX claystone

Another triaxial creep test performed on the COX claystone under very low deviatoric stresses is also simulated. Fig. 5.33 shows the modelling results in comparison with the measured data. For fitting the data, the creep parameters are newly determined: $\sigma_s = 1.0$ MPa, $\gamma = 2.0 \cdot 10^{-7}$ d^{-1}, $n = 2.5$, $m = 530$. The other parameters used are: $E = 3.2$ GPa, $\nu = 0.25$, $\xi_1 = 0.003$, $\xi_2 = 0.004$, $\xi_3 = 0.012$. The model curves are close to the measured ones. But the short transient creep stage cannot be well matched by the model. This is however not significant for prediction of the long-term deformation of the clay rock during the repository post-closure phase over hundreds of thousands of years.
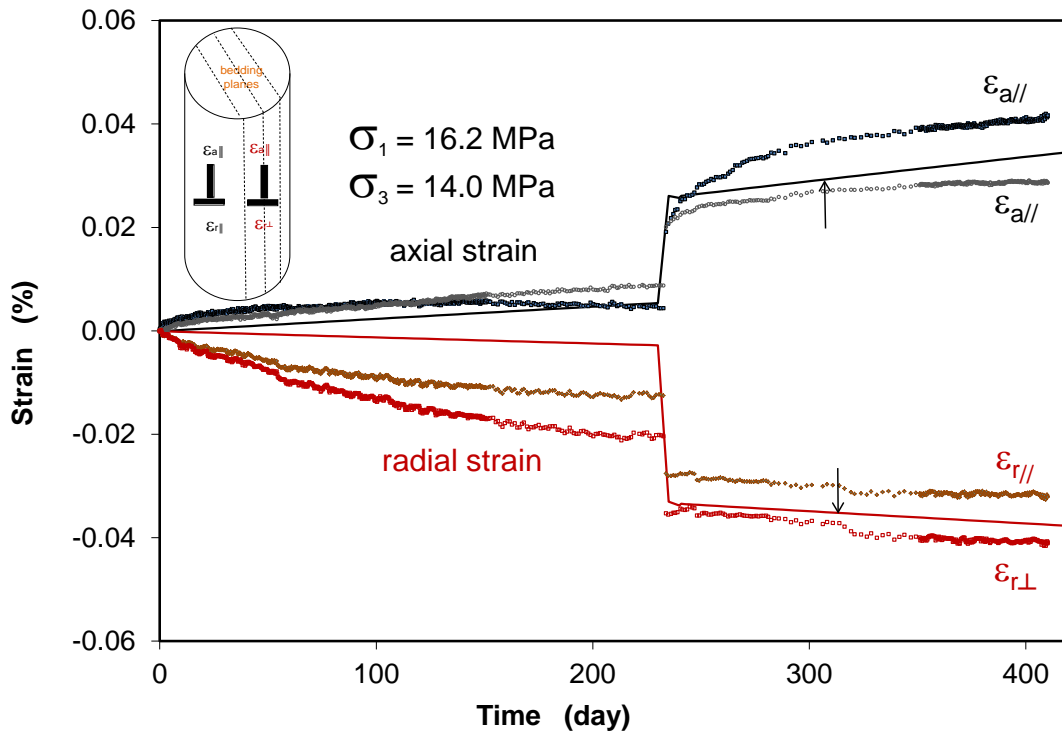

Fig. 5.33   Modelling results of the long-term deformation behaviour of the COX clay-stone under low deviatoric stresses

6 Summary and conclusions

Within the DOPAS project, the sealing behaviour of damaged claystone was studied with artificially-cracked samples under repository-relevant conditions, including damage-induced permeability changes, permeability reduction due to fracture closure, and gas migration in resealed claystone. As an alternative to bentonite-based seal materials, excavated claystone mixed with bentonite was investigated along with pure bentonite and a bentonite-sand mixture. Under identical laboratory conditions, the three materials were comprehensively characterized in terms of key sealing properties such as compacted density, water uptake and retention, swelling capacity, water permeability, and gas migration. Based on the experimental results, the existing constitutive models for the description of the hydro-mechanical behaviour of claystone as well as of sealing materials were verified and improved. New formulations for some constitutive equations were found and used for the simulation of the hydro-mechanical behaviour observed in the experiments. The following important conclusions can be drawn from the investigations.

6.1 Sealing behaviour of fractured claystone

The Callovo-Oxfordian (COX) and Opalinus (OPA) claystones were taken for the sealing experiments. These claystones have relatively high portion of clay minerals amounting to 40 % in COX and 65 % in OPA.

Fracturing-induced permeability

High deviatoric stresses generate microcracks, which propagate and coalesce forming a network when the peak failure stress is reached. The development of the cracks results in a spontaneous increase of the permeability by up to several orders of magnitude. The increased permeability does not change much during the post-failure phase.

Fracture closure and permeability variation

The fractures in damaged claystone tend to close up when the normal confining stress is increased. This results in a decrease of permeability, depending on the fracture properties such as size, geometry, roughness and connectivity and the applied load. The permeability reduction is related to the fracture closure by a cubic law.

Water conductivity

As water enters and flows through fractures, the clay matrix can take up the water and expand into the interstices. Consequently, the hydraulic conductivity decreases dramatically. This decrease can amount to several orders of magnitude down to very low levels of 10^{-19} to 10^{-21} m^2 even at low confining stresses of 2-4 MPa. This process is completed within relatively short periods of times, i.e. months to years, compared with the long post-closure phase of tens of thousands of years. Moreover, the sealing of the fractures is not significantly affected by the thermal loading in the testing range between 20 °C and 90 °C. The very low water permeabilities after resealing of the fractures are in the same order as that of the intact claystones, indicating that the fractures in the claystones can be completely resealed under the repository conditions.

Gas migration

In a partially saturated claystone, the fractures in the EDZ act as preferential pathways for gas. However, after full water saturation, gas entry and subsequent penetration into the resealed fractures requires a certain gas pressure to overcome the capillary thresholds. The gas entry/breakthrough pressure is controlled by the degree of fracture sealing which is in turn depending on the confining stress. It was observed that the gas breakthrough pressures in the water-saturated and highly-resealed claystones are still lower than the confining stresses. It implies that the EDZ, even when highly resealed, will still have the capacity for gas migration at moderate pressures without fracturing the host rock.

Generally speaking, the high sealing capacities of the studied COX and OPA claystones hinder water transport and thus radionuclides migration through the EDZ, but allow gas flow at moderate pressures without fracturing the host rock. These significant advantages guarantee the long-term sealing functions of the plug/seal systems and hence the long-term safety of the repositories in the clay formations.

6.2   Properties of clay-based sealing materials

As an alternative to bentonite-based materials, excavated claystone mixed with bentonite was investigated for sealing of boreholes, drifts and shafts in repositories in clay formations. The crushed COX claystone taken from the MHM-URL was prepared to

contain only grains of diametres below 5 mm and 10 mm, respectively, and mixed with the expansive bentonite MX80 (d < 2 mm) with ratios of 80/20 and 60/40. For the purpose of comparison, the pure bentonite and a bentonite-sand mixture with a ratio of 70/30 were also tested. These materials were characterized with respect to the key sealing properties such as compacted density, water uptake and retention, swelling capacity, water conductivity, and gas migration. A comparison between the different mixtures yields the following conclusions.

- *Compacted density*: Under the same load of 30 MPa, a higher dry density of 1.9 g/cm^3 was achieved for the claystone-bentonite mixture with the ratios of 80/20 and 60/40, compared with that of 1.8 g/cm^3 for the bentonite-sand mixture (70/30) and 1.56 g/cm^3 for the pure bentonite.
- *Water retention*: All the mixtures have significant water uptake and retention capacities, depending on bentonite content and confinement. In vapour and free swelling conditions, the maximum amount of water uptake is reached at 45-48 % for the bentonite, at 32 % for the bentonite-sand mixture, and at 28-20 % for the claystone-bentonite mixture (60/40; 80/20).
- Water saturation duration: The claystone-bentonite mixture exhibits a faster saturation than the bentonite-sand mixture and the pure bentonite. The rate of water uptake increases with decreasing bentonite content and density.
- *Swelling capacity*: All the compacted mixtures have certain swelling capacities, which increase with bentonite content and dry density. The maximum swelling pressures achieved after water saturation are: 7.5 MPa for the bentonite; 6.0 MPa for the bentonite-sand mixture, 3.5 MPa and 2.5 MPa for the claystone-bentonite mixture with ratios of 60/40 and 80/20, respectively.
- *Water conductivity*: All the compacted mixtures show very low water permeabilities of 10^{-19} to 10^{-20} m^2 which is close to that of the intact clay rocks.
- *Gas migration*: Gas breakthrough pressures observed on the claystone-bentonite mixture are below the confining stresses or swelling pressures, while the compacted bentonite and bentonite-sand mixture remain to be gas tight at pressures close to the confining stresses.

Similar results were obtained from the borehole sealing tests with claystone-bentonite (60/40) and bentonite-sand (70/30) blocks. Here, the blocks were assembled in steel cylinders with bentonite powder filling the gaps between blocks and borehole wall. It was found that: (a) the measured water permeabilities are very low at 1·10^{-19} m^2 for the clay-

stone-bentonite seal and $1 \cdot 10^{-20}$ for the bentonite-sand seal respectively, which are nearly the same as those measured on the individual compacted blocks; (b) the swelling pressures after water saturation are equal to 2 MPa for both the seals, being somewhat lower than those of the compacted blocks due to the low density of the bentonite powder filled in the gaps.

Table 6.1   Key properties of the compacted mixtures and assembled seals

Compacted mixtures	Claystone-bentonite (80/20)	Claystone-bentonite (60/40)	Bentonite-sand (70/30)	Bentonite (MX80)
Dry density (g/cm^3)	1,90	1,90	1,80	1,56
Water permeability (m^2)	$1 \cdot 10^{-19}$	$6 \cdot 10^{-20}$	$2 \cdot 10^{-20}$	$5 \cdot 10^{-21}$
Swelling pressure (MPa)	2.5	3.5	6.0	7.5
Gas breakthrough pressure (MPa)	1.2	2.5	6.0	≥7.5
Assembled seals	**Claystone-bentonite (60/40)**		**Bentonite-sand (70/30)**	
Dry density (g/cm^3)	1,88		1,80	
Water permeability (m^2)	$1 \cdot 10^{-19}$		$1 \cdot 10^{-20}$	
Swelling pressure (MPa)	2.0		2.0	
Gas breakthrough pressure (MPa)	to be determined		to be determined	

The important parameters are summarized in Table 6.1 for the compacted mixtures and the assembled seals. It can be concluded that

- the water permeabilities of the studied sealing materials are very low, close to that of the intact clay rocks, and thus suitable for drift seals (in the French concept, for instance, a permeability lower than 10^{-18} m² is demanded /AND 15/);
- the swelling pressures of the sealing materials after water saturation are sufficiently high to enhance the sealing process of the EDZ;
- the claystone-bentonite mixture can be compacted to higher densities compared to the pure bentonite and bentonite-sand mixture;
- the compacted claystone-bentonite seal allows gas migration at moderate pressures, guaranteeing the integrity of the natural and engineered barrier system; and
- in contrast to the claystone-bentonite seal, the compacted bentonite and bentonite-sand mixtures are gas tight even at pressures up to the confining stress, so that the high gas pressures might generate fractures in the surrounding host rock.

6.3 Modelling

In order to enhance the predictive capability of numerical models for the long-term performance of the sealing systems in a repository, the existing constitutive models describing the hydro-mechanical behaviour of the sealing materials and clay host rock were verified and improved. New constitutive equations were formulated and the related parameters fitted to the laboratory observations. Based on the experimental results, the key parameters were determined for each sealing material and for the claystone. They were applied for numerical simulations of various laboratory experiments using the THM code CODE-BRIGHT.

Modelling of the performance of sealing materials

First of all, adequate hydro-mechanical material models were established for the studied sealing materials, i.e. the compacted bentonite, bentonite-sand and claystone-bentonite mixtures. Model parameters were determined from the test data, including the porosity, permeability, water retention curve, the nonlinear elastic modulus, and others. Based on these parameters, the development of water saturation and swelling pressure in the seal materials was calculated. The modelling provides a satisfactory agreement with the measured data. However, some uncertainty in the models and the parameters remains and has to be minimized through further investigations.

Development of new models for clay rock

The constitutive models implemented in CODE-BRIGHT for claystone were enhanced by the development of some new constitutive relations for the long-term deformation, permeability variations with damage and reconsolidation, water conductivity and gas migration in fractured and resealed claystone.

Mitchell's creep equation was modified to a hyperbolic sine equation (Eq. 5.42) for the stationary shear creep of the water-saturated clay rock. The temperature effect on the creep is taken into account by the Arrhenius law. The creep parameters were established from the long-term triaxial creep experiments on the COX claystone.

Based on the measurements of gas permeability during mechanical loading, a percolation permeability model (Eq. 5.30) was formulated. It describes the dependency of the permeability on loading before and after peak failure as well as during recompaction.

137

The permeability is related to the minor confining stress and volumetric strain. Model parameters for the COX claystone were derived.

Because of the significant swelling effects, the water permeability of the fractured claystone is several orders of magnitude lower than the gas permeability. Based on the measurements of water permeability of the fractured claystone, a relationship was established for the water permeability to effective confining stress (Eq. 5.31).

For modelling of gas migration in water-saturated and resealed claystone, empirical models were formulated for the gas breakthrough pressure as a function of the water permeability and the minor confining stress (Eq. 5.31). Other relations concern the gas permeability as a function of gas pressure (Eq. 5.32) or the effective confining stress (Eq. 5.33).

It is intended to implement these new models in CODE-BRIGHT in the framework of another GRS programme. Currently, the code developers at UPC have established a new visco-elastoplastic model for claystone (Eqs. 5.34-5.41). This model has been used for the simulation of the short-term and long-term deformation experiments on the COX claystone and was validated by comparison with the data. However, the constitutive models still need to be improved for more adequate description of the hydro-mechanical behaviour of clay rock, particularly with regards to the long-term sealing process and gas migration in the EDZ.

Acknowledgements

References

/ÅKE 10/   Åkesson, M., Kristensson, O., Börgensson, L., Dueck, A. (2010): THM modelling of buffer, backfill and other system components – Critical processes and scenarios. SKB Technical Report TR-10-11, March 2010.

/ÅKE 13/   Åkesson, M. and Andersson, L. (2013): BRIE Water-uptake test Clay Technology AB, Lund, Sweden, April / September 2013.

/AND 05/   ANDRA DOSSIER (2005): Synthesis – Evaluation of the feasibility of a geological repository in an argillaceous formation.

/AND 15/   ANDRA (2015): Status of the Cigéo Project in France - French Industrial Geological Disposal Project, in the Proceedings of the LUCOEX Conference and Workshop, June 2-4, 2015, Oskarshamn, Sweden.

/ARM 14/   Armand, G., Leveau, F., Nussbaum, C., de La Vaissiere, R., Noiret, A., Jaeggi, D., Landrein, P., Righini, C. (2014): Geometry and Properties of the Excavation-Induced Fractures at the Meuse/Haute-Marne URL Drifts, Roch Mech Rock Eng (2014) 47, 21-41.

/BGR 07/   Hoth, P., Wirth, H., Reinhold, K., Bräuer, V., Krull, P., Feldrappe, H. (2007): Untersuchung und Bewertung von Tongesteinsformationen, Bundesanstalt für Geowissenschaften und Rohstoffe, Berlin/Hannover, April 2007.

/BIR 13/   Birgersson, M., Karnland O. (2013): Gas intrusion in bentonite – Results of small scale experiments, FORGE International Symposium and Workshop on Gas Generation and Migration, February 5-7, 2013, Luxembourg.

/BLU 07/   Blümling, P., Bernier, F., Lebon, P., Martin, C.D. (2007): The excavation damaged zone in clay formations: time-dependent behaviour and influence on performance assessment, Physics and Chemistry of the Earth, 32, 588-599.

/BOC 10/ Bock, H., Dehandschutter, B., Martin, C.D., Mazurek, M., Haller, A.D., Skoczylas, F., Davy, C. (2010): Self-Sealing of Fractures in Argillaceous Formations in the Context of Geological Disposal of Radioactive Waste – Review and Synthesis. Clay Club Report, OECD, NEA No. 6184.

/BOS 04/ Bossart, P., Trick, T., Meier, P.M., Mayor, J.C. (2004): Structural and hydrogeological characterisation of the excavation-disturbed zone in the Opalinus Clay (Mont Terri Project. Switzerland), Applied Clay Science 26, 429-448.

/DEL 13/ de La Vaissiere, R. and Talandier J. (2013): Gas Injection Test in the Meuse/Haute Marne Underground Research Laboratory, FORGE International Symposium and Workshop on Gas Generation and Migration, February 5-7, 2013, Luxembourg.

/DEL 15/ de La Vaissiere, R., Conil, N; Leveau, F., Armand, G. (2015): Large-Scale Sealing Experiment in the Meuse/Haute Marne Underground Research Laboratory, The 6th International Clay conference – Clays in Natural & Engineered Barriers for Radioactive Waste Confinement, March 23-26, 2015, Brussels.

/FOI 15/ Foin, R., Bosgiraud, J.-M., Armand, G., Noiret, A. (2015): Technical feasibility of the Cigéo Project seals, in the Proceedings of the LUCOEX Conference and Workshop, June 2-4, 2015, Oskarshamn, Sweden.

/FRE 93/ Fredlund, D.G., Rahardjo, H. (1993): Soil Mechanics for Unsaturated Soils. John Wiley & Sons, INC.

/GEN 98/ Gens, A., Garcia-Molina, A.J., Olivella, S., Alonso, E.E., Huertas, F. (1998): Analysis of a Full Scale in-situ Test Simulating Repository Conditions. Int. J. Numer. Anal. Meth. Geomech., 22, 515-548, 1998.

/GEN 06/ Gens, A. A., Olivella, S.: Coupled Thermo-Hydro-Mechanical Analysis of Engineered Barriers for High-Level Radioactive Waste, in Chinese Journal of Rock Mechanics and Engineering, 2006, 25(4), 670 -680.

/HAN 13/ Hansen, J., Holt, E., Palmu, M. (2013): DOPAS: 'Full-scale in situ Demonstration of Tunnel Plugs and shaft Seal in Clay, Crystalline and Salt Repository Host-Rock Formations', EURADWASTE'13 – 8th EC Conference on the Management of Radioactive Waste Community Policy and Research on Disposal, 14-17 October 2013, Vilnius, Lithuania.

/HAN 14/ Hansen, J. (2014): A general overview of DOPAS project and first year achievements for full-scale demonstration of plugs and seals, PEBS International Conference on the Performance of Engineered Barriers, February 6-7, 2014, Hannover.

/HER 15/ Herold, P., Gruner, M., Jobmann, M., Kudla, W. (2015): Konzeptentwicklung für Schachtverschlüsse im Ton- und Salzgestein, Technischer Bericht (Entwurf), DBE TECHNOLOGY GmbH, TU Bergakademie Freiberg (in German).

/JOB 15a/ Jobmann, M., Meleshyn, A., Maßmann, J. & Polster, M. (2015): Quantifizierung von Kriterien für Integritätsnachweise, Technischer Bericht (Entwurf), BGR, GRS, DBE TECHNOLOGY GmbH, Ber. Nr.: TEC-08-2013-AP, Peine (in German).

/JOB 15b/ Jobmann, M. & Lommerzheim, A. (2015): Endlagerkonzept sowie Verfüll- und Verschlusskonzept für das Endlagerstandortmodell SÜD, Technischer Bericht (Entwurf), DBE TECHNOLOGY GmbH, Peine (in German).

/KAR 08/ Karnland, O., Nilsson, U., Weber, H., Wersin, P. (2008): Sealing ability of Wyoming bentonite pellets foreseen as buffer material – Laboratory tests, Physics and Chemistry of the Earth 33, 472-475

/KOH 15/ Köhler, S., Fries, T., Müller, H.R., Gaus, I. (2015): Swiss Backfilling Concept – Requirements and Aproaches for Optimization of the Bentonite Barrier around SF/HLW Disposal Canisters, The 6th International Clay conference – Clays in Natural & Engineered Barriers for Radioactive Waste Confinement, March 23-26, 2015, Brussels.

/KRÖ 04/ Kröhn, K.-P. (2004): Modelling the re-saturation of bentonite in final repositories in crystalline rock, final report, GRS – 199.

/LOM 15/ Lommerzheim, A. & Jobmann, M. (2015): Endlagerkonzept sowie Verfüll- und Verschlusskonzept für das Endlagerstandortmodell NORD, Technischer Bericht (Entwurf), DBE TECHNOLOGY GmbH, Peine (in German).

/MIT 76/ Mitchell, J.K. (1976): Fundamentals of Soil Behavior. University of California, Berkeley, USA

/MUL 15/ Müller, H.R., Vogt, T., Garritte B., Köhler, S., Sakaki, T., Weber, H., Vietor, T. (2015): The Full-Scale Emplacement Experiment – Implementation of a Multiple Heater Experiment at the Mont Terri URL, The 6th International Clay conference – Clays in Natural & Engineered Barriers for Radioactive Waste Confinement, March 23-26, 2015, Brussels.

/NAG 02/ NAGRA (2002): Project Opalinus Clay, Models, Codes and Data for Safety Assessment – Demonstration of disposal feasibility for spent fuel, vitrified high-level waste and long-lived intermediate-level waste

/NIA 97/ Niandou, H., Shao, J.F., Henry, J.P., Fourmaintraux, D. (1997): Laboratory Investigation of the Mechanical Behaviour of Tournemire Shale, Int. J. Rock Mech. Min. Sci. Vol 34, No. 1, pp. 3-16

/MIT 92/ Mitchell, J.K. (1992): Characteristics and Mechanisms of Clay Creep and Creep Rupture, in "Clay-water interface and its rheological implications, Clay Mineral society", Vol.4, 212-244.

/OEC 04/ OECD (2004): Safety of Disposal of Spent Fuel, HLW and Long-lived ILW in Switzerland – An international peer review of the post-closure radiological safety assessment for disposal in the Opalinus Clay of the Zürcher Weinland. NEA No. 5568.

/OLI 94/   Olivella, S.; Carrera, J.; Gens, A.; Alonso, E.E. (1994): Nonisothermal Multiphase Flow of Brine and Gas Through Saline Media. Transport in Porous Media, 15, 271-293 (1994).

/POP 07/   Popp, T. and Salzer, K. 2007: Anisotropy of seismic and mechanical properties of Opalinus clay during triaxial deformation in a multi-anvil apparatus, Physics and Chemistry of the Earth, 32, 879-888.

/RUI 15/   Ruiz, D.F., Vaunat, J., Gens, A., Manica, M., Pasteau, A. (2015): Insights into the response of a gallery sealing over the entire life of a deep repository, The 6th International Clay Conference – Clays in Natural & Engineered Barriers for Radioactive Waste Confinement, March 23-26, 2015, Brussels.

/RUT 83/   Rutter, E.H. (1983): Pressure solution in nature, theory and experiment, Journal of Geological Society. London, Vol. 140, pp. 725-740.

/SHA 15/   Shaw, R.P. (editor): Gas Generation and Migration in Deep Geological Radioactive Waste Repositories, Special Publication 415 of the Geological Society of London, 2015.

/UPC 15/   UPC (2015): User's Guide of CODE-BRIGHT - A 3-D Program for Thermo-Hydro-Mechanical Analysis in Geological Media, Department of Geotechnical Engineering and Geosciences of Technical University of Catalonia (UPC), Barcelona, Spain.

/VAN 80/   Van Genuchten, M.T. (1980): A Closed-Form Equation for predicting the hydraulic Conductivity of Unsaturated Soils. -Soil Sci. Soc. Am. J., 44:892-898

/VAU 03/   Vaunat, J., Alonso, E.E., Gens, A. (2003): constitutive model of short and long term behaviour of the Meuse/Haute-Marne argillite. Deliverable 2&3 of the EC project MODEX-REP, FIKW-CT2000-00029.

/VIG 11/ Viggiani, G., Bésuelle, P, Desrues, J. (2011): X-ray Micro Tomography as a Tool for Studying Localized Damage / Deformation in Clay Rock, NEA CLAY CLUB Workshop Proceedings – Clay characterisation from nanoscopic to microscopic resolution, Karlsruhe, Germany, September 2011.

/VOL 96/ Volckaert,G.; Bernier,F.; Alonso,E.; Gens,A.; Samper,J.; Villar,M.; Martin-Martin,P.L.; Cuevas,J.; Campos,R.; Thomas,H.; Imbert,C.; Zingarelli,V. (1996): Thermo-hydraulic-mechanical and geochemical behaviour of the clay barrier in radioactive waste repositories (model development and validation), Final report, EUR 16744 EN.

/WHI 14/ White, M., Doudou, S., Neall, F. (2014): DOPAS-Deliverable D2.1: Design Bases and Criteria.

/ZHA 08a/ Zhang, C.L., Rothfuchs, T., Dittrich, J., Müller, J. (2008): Investigations on self-sealing of indurated clay – part of the EC NFPRO project, Bericht GRS-230, Gesellschaft für Anlagen- und Reaktorsicherheit (GRS) mbH, Braunschweig.

/ZHA 08b/ Zhang, C.L., Rothfuchs, T. (2008): Damage and sealing of clay rocks detected by measurements of gas permeability, Physics and Chemistry of the Earth, Vol. 33, 363-373

/ZHA 09/ Zhang C.L. (2009): Self-sealing of Fractures in Argillites under Repository conditions, The international conference and workshop in the framework of the EC TIMODAZ and THERESA projects, Sept. 2009, Luxembourg

/ZHA 10a/ Zhang, C.L., Czaikowski, O., Rothfuchs, T. (2010): Thermo-Hydro-Mechanical Behaviour of the Callovo-Oxfordian Clay Rock – Final report of the BURE-HAUPT/EC-TIMODAZ project, Bericht GRS-266, Gesellschaft für Anlagen- und Reaktorsicherheit (GRS) mbH, Braunschweig.

/ZHA 10b/ Zhang, C. L, Wieczorek, K., Xie, M. L. (2010): Swelling experiments on mudstones, Journal of Rock Mechanics & Geotechnical Engineering, 2(1) 41-47

/ZHA 11/   Zhang C.L. (2011): Experimental Evidence for Self-sealing of Fractures in Claystone, Physics and Chemistry of the Earth, Vol. 36: 1972-1980.

/ZHA 13a/   Zhang, C.-L., O. Czaikowski, T. Rothfuchs, K. Wieczorek (2013): Thermo-Hydro-Mechanical Processes in the Nearfield around a HLW Repository in Argillaceous Formations - Volume I: Laboratory investigations, May 2007 to May 2013, Bericht GRS-312, Gesellschaft für Anlagen- und Reaktorsicherheit (GRS) mbH, Braunschweig.

/ZHA 13b/   Zhang C.L. (2013): Sealing of Fractures in Claystone, Journal of Rock Mechanics and Geotechnical Engineering 5, 214-220.

/ZHA 14a/   Zhang C.L. (2014): Status report for the EC DOPAS project Deliverable (D5.5): Characterization and modelling of clay rock and claystone-based seal material, Bericht GRS-A-3761, Gesellschaft für Anlagen- und Reaktorsicherheit (GRS) mbH, Braunschweig.

/ZHA 14c/   Zhang, C.L. (2014): Characterization of Excavated Claystone and Claystone-Bentonite Mixtures as Backfill/Seal Material, Geological Scociety Special Publication 400 – Clays in Natural and Engineered Barriers for Radioactive Waste Confinement (edited by Norris et al.), The Geological Society of London, 2014, 323-337.

/ZHA 14d/   Zhang, C.L. (2014): Investigations of Excavated Claystone as Backfill/Seal Material, PEBS International Conference on the Performance of Engineered Barriers, February 6-7, 2014, Hannover.

/ZHA 15a/   Zhang, C.L. (2015): Deformation of Clay Rock under THM Conditions, Geomechanics and Tunnelling 8 (2015), No. 5, 426-435.

/ZHA 15b/   Zhang, C.L. (2015): The Stress-Strain-Permeability Behaviour of Clay Rock during Damage and Recompaction, Journal of Rock Mechanics and Geotechnical Engineering (2015), http://dx.doi.org/10.1016/j.jrmge.2015.10.001 .

/ZHA 15c/ Zhang, C.L., Armand, G., Conil, N. (2015): Investigation on the Anisotropic Mechanical Beahviour of the Callovo-Oxfordian Clay Rock, Final Report of the ANDRA/GRS Experimental Programme, Bericht GRS-360, Gesellschaft für Anlagen- und Reaktorsicherheit (GRS) mbH, Braunschweig.